City Research Online

City St George's, University of London

Permanent repository link: https://openaccess.city.ac.uk/id/eprint/24723/

City Research Online: http://openaccess.city.ac.uk/   publications@citystgeorges.ac.uk

Cavitation and the Application of Methods for Erosion Prediction in High Pressure Fuel Injection Systems

Maxwell J. Brunhart

Thesis submitted for the fulfilment of the requirements for:

Degree of Doctor of Philosophy

School of Mathematics, Computer Science & Engineering

Department of Aeronautical and Mechanical Engineering

City, University of London

London, UK

2020

I, Maxwell Brunhart, confirm that the work presented in this thesis is my own. Where information has been derived from other sources, I confirm that this has been indicated in the thesis.

Maxwell Brunhart

London, 2020

Table of Contents

List of Figures

List of Tables

Acknowledgments

I would like to start off by thanking my industrial supervisor, Dr. Celia Soteriou, for her continued support throughout these past years. Completing this work would not have been possible without her vision, experience and knowledge. Secondly, I would like to thank my academic supervisors, Prof. Manolis Gavaises. And Dr. Phoevos Koukouvinis for their expert advice.

I would also like to thank my colleagues at City - University of London, Delphi Technologies and in the CaFE project (Cavitating Flows, surface Erosion damage and material loss, MSCA-ITN-2014-ETN). We have all shared in the triumphs and struggles during our work and it has been a pleasure to work with all of them.

I am grateful to my parents for their endless support and encouragement, to my partner for her patience and understanding, and to a lesser extent, to my brothers who thought I only went traveling for conferences these past few years.

Maxwell J. Brunhart

May 2020

Abstract

Cavitation, the appearance of vapour in a homogeneous liquid through pressure changes, is common in many fields like naval, automotive and aviation, and often leads to problems such as reduced efficiency, noise and erosion. Consequently, there has been extensive research dedicated to understanding and controlling the effects of cavitation, through experiments and CFD simulations.

There is currently no reliable model to predict cavitation erosion. Moreover, simply having cavitation collapse near a solid wall will not always result in erosion. To explore cavitation characteristics and cavitation erosion three different components have been investigated with Computational Fluid Dynamics (CFD) simulations, results of which are presented here. The components investigated included an axisymmetric converging-diverging Venturi nozzle, a thin liquid filled gap between a Shoe and Guide assembly in a high-pressure fuel injection pump, and a control orifice in a prototype diesel injector.

Cavitating flow dynamics are investigated in a Venturi nozzle. Computational Fluid Dynamics (CFD) results are compared with those from previous experiments. Analyses performed on the quantitative results from both data sets reveal a coherent trend and show that the simulations and experiments agree well. The CFD results have confirmed the interpretation of the high-speed images of the Venturi flow, which indicated there are two vapor shedding mechanisms that exist under different running conditions: re-entrant jet and condensation shock. Moreover, they provide further detail of the flow mechanisms that cannot be extracted from the experiments. For the first time on this cavitating Venturi nozzle flow, the re-entrant jet shedding mechanism is reliably achieved in CFD simulations. The condensation shock shedding mechanism is also confirmed, and details of the process are presented. These CFD results compare well with the experimental shadowgraphs, space-time plots and time-averaged reconstructed computed tomography (CT) slices of vapor fraction.

For the Shoe and Guide component, real industrial examples were used to evaluate the viability of several cavitation erosion risk indicators (ERIs). Industry standard endurance tests resulted in non-critical cavitation erosion of a shoe and shoe-guide assembly in a high-pressure fuel pump. A design modification was made which eliminated the erosion. For the current work, transient CFD simulations of the two designs were run. The distribution and intensity of the resulting ERIs were evaluated against photographic evidence of erosion taken after endurance testing. Details of the component dynamics and the resulting cavitation formation and collapse are presented, along with an analysis of the ERIs for their potential usefulness. Of the 10 ERIs studied, two were found to be particularly good indicators, one of which is newly derived for this research.

Lastly, for the Control Orifice, an early prototype design resulted in cavitation erosion after endurance testing. A design modification eliminated the erosion and subsequent prototypes were free from damage. CFD results for the two designs using different simulation methods are discussed, along with the effects of different rates of evaporating and condensing mass transfer. Findings on the successful ERIs from comparing the eroding with the non-eroding design are presented. The two successful ERIs from the Shoe and Guide component work were also successful for the Control Orifice which emphasises the robustness of these ERIs. It is now anticipated that using these ERIs to guide product design and development will save considerable time and cost.

Present Contributions

- **For the first time, erosion risk indicators (ERIs) have been established by testing them against two component types, which have significantly different flow conditions, as well as benchmarking results on similar designs that do not experience cavitation erosion** – ERIs were studied on two component types, each of which had significantly different geometry, flow conditions and cavitation characteristics that lead to erosion. Furthermore, each component type had two design levels examined, an original eroding design and a modified non-eroding design. This allowed the ERIs to be benchmarked against a control case, which is unique in this type of work and, in many cases, provided the deciding factor on the ERIs usefulness. With this, 10 potential ERIs were tested on one component type, and later an additional 9 on a second component type. Of the 10 ERIs tested on both component types, two were found to identify erosion even given the different flow characteristics and modelling criteria.

- **Novel ERIs proposed and tested** – Of the 19 potential ERIs tested, many are novel to this research. Of the two ERIs which were successful on both component types, one has never been seen before in the literature. An additional three ERIs found to be useful that were only tested on the Control Orifice component have also not been seen before in the literature.

- **Component types uncommon in published literature** – The two component types are real-world designs related directly to industry prototypes, as opposed to experimental test pieces. This contrasts with most published research, which uses simplified designs. Eroding conditions of an expanding, liquid filled gap are found in components like gear pumps, bearings and cylinder liners, but the application of ERIs to these cases has not been seen in the literature. Concerning the Control Orifice, which can be found in almost every injector and pump, there are relatively few publications, especially when considering eroding conditions.

- **Frequency rather than maxima of ERIs may be a useful indicator** - A successful ERI is typically one that had high values on the eroding design in the region of erosion, as seen on hardware, and low values on the non-eroding design. However, the Control Orifice results indicate that the number of times an ERI quickly goes above a certain threshold value may also be significant in indicating erosion. This was clearly demonstrated as the two Control Orifice designs had similar peak values of pressure and *Dp/Dt* (among others), but the original design, which suffered from erosion, experienced over 10 times more impulses.

- **Vapour shedding mechanisms analysed in depth which led to the simulation of a shedding mechanism not reliably achieved in previous research for this geometry** – Two different shedding mechanisms were simulated on a Venturi nozzle. The condensation shock shedding

mechanism was simulated and compared better to experimental data than seen in previous studies. The re-entrant jet shedding mechanism was also recreated, which has not been reliably achieved before with this component. These simulations were achieved by performing a more thorough analysis to understand the whole data set first. In addition, the work clarifies the shedding mechanisms for internal three-dimensional geometries of circular cross-section, instead of simplified, often two-dimensional geometries, such as the frequently used wedge.

Nomenclature

Symbols

A	Area (m^2)
B	Bulk modulus (Pa)
C	Isentropic constant
c	Speed of sound (m/s)
D	Characteristic length (m)
F	Empirical constant (m^{-1})
f	Frequency (Hz)
L_s	spatial limiter
$\dot{m}$	Mass flow rate (kg/s)
P_a	Acoustic power (W)
P_p	Potential power (W)
p	Pressure (static pressure) (bar)
p_d	Dynamic pressure (bar)
$\mathfrak{R}$	Bubble radius (m)
R	Rate of mass transfer (kg/m^3/s)
S	Surface tension (N/m)
S_{ij}	strain rate tensor
s	Wave speed (m/s)
t	Time (s)
u	Axial velocity component (m/s)
$\bar{u}$	Average velocity (m/s)
$\boldsymbol{U}$	Velocity vector field (m/s)
Y+	Dimensionless wall distance
V_{cell}	Volume of cell (m^3)
α	Volume fraction
γ	Heat capacity ratio
$\Delta p = p_{in} - p_{out}$	Pressure drop (Pa)
$\varepsilon \sim U^3/D$	Turbulent dissipation (m^2/s^3)
$\lambda = \sqrt{10} Re^{-1/2} D$	Taylor length scale (m)
μ	Dynamic viscosity (Pa·s)
μ_t	Turbulent viscosity (kg/m/s)
ρ	Density (kg/m^3)
$\tau = \sqrt{\upsilon/\varepsilon}$	Kolmogorov time scale (s)
$\bar{\bar{\boldsymbol{\tau}}}$	Stress tensor (Pa)
υ	Kinematic viscosity (m^2/s)

Subscripts

c	Condensation
e	Evaporation
u	Inlet (upstream)
d	Outlet (downstream)
$post$	Post-shock

pre	Pre-shock
l	Liquid
v	Vapour
ref	Reference
sat	Saturation

Abbreviations

CT	Computed tomography
DES	Detached Eddy Simulation
ERI	Erosion Risk Indicator
EoS	Equation of State
LES	Large Eddy Simulation
LSM	Large Scale Model
PPD1	1st definition of Potential Power Density (W/m^3)
PPD2	2nd definition of Potential Power Density (W/m^3)
RP	Rayleigh-Plesset
SAS	Scale Adapted Simulation
UDF	User Defined Function
(U)RANS	(Unsteady) Reynolds-Averaged Navier-Stokes
ZGB	Zwart-Gerber-Belamri

Non-dimensional numbers

$Cd = \dot{m}/(A\sqrt{2\rho\Delta p})$	Coefficient of discharge
$CN = \Delta p/(p_{out} - p_v)$	(Bergwerk) Cavitation number
$K = 2\Delta p/\rho U^2$	Loss factor
$Re = UD/\upsilon$	Reynolds number
$St = fD/U$	Strouhal number
$\sigma = 2(p_{out} - p_v)/\rho U^2$	(Thoma) Cavitation number

1 - Introduction

1.1 - Motivation

Cavitation, described as the phase change of liquids into vapour due to a drop in the local static pressure, is common in many fields like naval, automotive, aviation and even medical. However, while cavitation is prevalent, it often results in reduced efficiency, noise and can even lead to erosion damage when the vapour violently collapses. Consequently, there has been extensive research dedicated to understanding and predicting the effects of cavitation with experimental and numerical simulation techniques. Nevertheless, erosion caused by cavitation is still an ongoing field of research due to the complexity of the physics in the micro and macro scales of cavitation collapse and due to the interaction with the boundary material. Moreover, simply having cavitation collapse near a solid wall will not always result in erosion. These challenges are some of the reasons why there is no consistently accurate model to predict cavitation erosion.

The importance of cavitation research is immediately apparent when considering the transportation sector. According to ExxonMobil [1], diesel is expected to remain the backbone of the commercial transportation sector up to 2040 (Fig. 1.1). While there is movement toward electrification, there is still a large demand for diesel engines. Thus, there is still ongoing research to improve diesel engines and reduce emissions. Work by Keeler et al [2] demonstrated that lower emissions could be achieved by increasing the injection pressure (see also the IPPAD project). However, this can lead to an increase in cavitation erosion as it is closely linked to flow velocity [3]. Challenges such as these highlight the need for more accurate and reliable erosion risk indicators
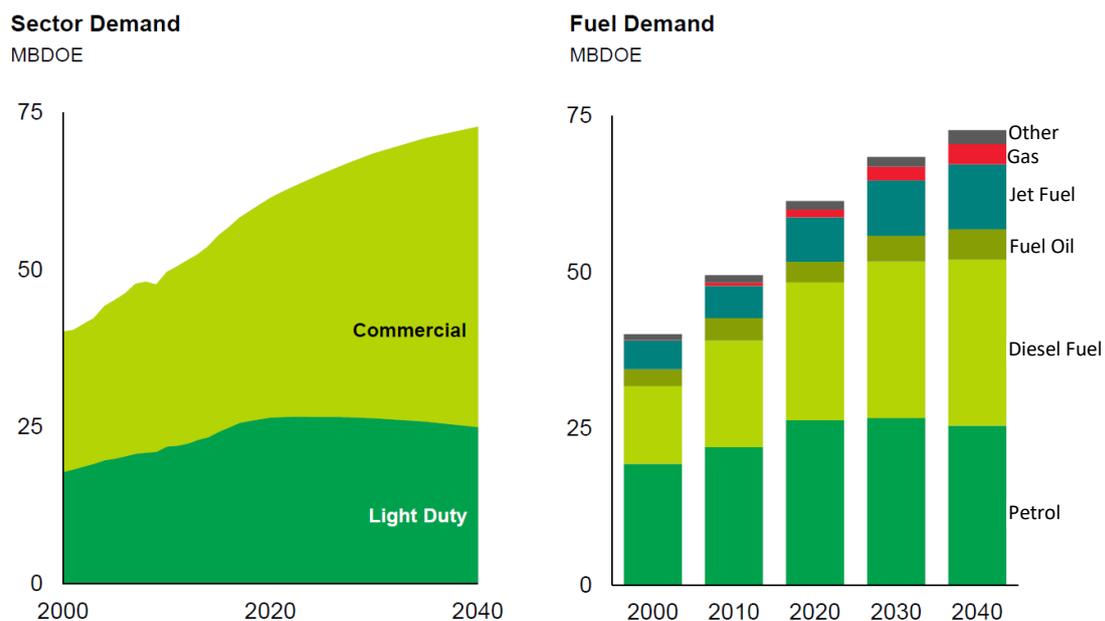
Fig. 1.1 – Projected energy consumption by energy source for the world's transportation sector given in million barrels per day of oil equivalent (MBDOE) [1].

(ERIs) to be developed. By developing these ERIs there would also be a shift in resolving challenges related to cavitation in the early prototype phase with simulations rather than later in the design process on hardware.

1.2 - Literature Review

The phenomenon of cavitation has been known for centuries with much time and effort being devoted to its research. One of the first mentions of cavitation was by Euler [4] in a paper presented in 1754 about how cavitation influenced a type of water wheel. The actual term "cavitation" was first proposed be R.E. Froude, but first cited in 1895 for research on the poor performance of a ship propeller on the H.M.S. Daring [5]. It was discovered that the propellers were generating an unexpectedly low amount of thrust, which was later attributed to large vapour voids that formed around the propellers. As technologies have developed and put higher stresses of working fluids, the chances of cavitation, and subsequently cavitation erosion, have increased. The following sections cover important aspects of cavitation related to this work. For further reading of cavitation and cavitating flows, please refer to Franc et al [6] and Brennen [7].

1.2.1 - Cavitation Process

Cavitation is caused by the reduction in the local pressure in a liquid, past the saturation pressure, resulting in a phase change to vapour. Examining the phase diagram (Fig. 1.2) one can see that the vapour phase can be reached by either a reduction in pressure (cavitation) or by an increase in temperature (boiling). While the process of increasing the temperature or reducing the pressure do not occur independently, the respective changes are assumed to be negligible in the ensuing discussion.

When the pressure drops below a certain level within a liquid it is said to be in a state of tension. Once the tension is high enough the molecular forces binding the liquid together are overcome and a phase change occurs. The pressure at which this phase change occurs is termed the vapour pressure.

1.2.2 - Single Bubble Dynamics

The pioneering work of Lord Rayleigh [8] set the foundation of cavitation research. He derived equations for the rate of a spherical bubble to collapse and its characteristic collapse time. This was done by comparing the kinetic energy to the work needed to produce a spherical cavity. While Lord Rayleigh considered the bubble to be empty and the liquid incompressible, the equations are still widely used today. Commonly, newly developed cavitation models are initially validated by simulating a single bubble collapse (see [9], [10] and [11] as examples).
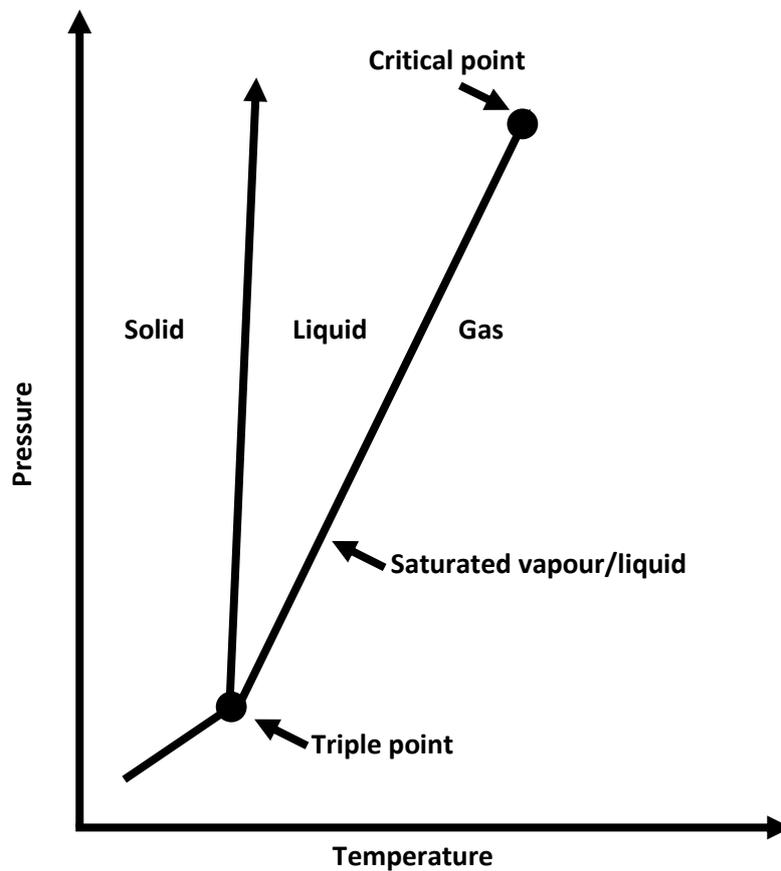
Fig. 1.2 - Phase diagram of a nondescript material

Following Lord Rayleigh's early work, Plesset [12] formulated the classic Rayleigh-Plesset (RP) equation (see Eq. 21 in chapter 2.4). Plesset considered pure vapour inside the bubble and added terms to account for the surface tension and viscosity. Plesset went on to compare simulated bubble growth and collapse to experimental data and found relatively good agreement. He mentioned some uncertainties which had not been fully explored then. He commented on the symmetry of the flow field and how thermal effects likely play an important role at the final stages of collapse. Moreover, he highlighted the importance of compressibility and the variability that could be caused by contaminant gas inside the bubble.

The assumption of compressibility was further theoretically studied by Moss [13] who modified the RP equation. With the modification they were able to improve agreement between simulated and experimental bubble motion, specifically during the final collapse. While the compressibility, along with thermal, viscous, surface tension and contaminated gas, are important during the final stages of bubble collapse, they are not typically simulated, as the final stage of collapse occurs within the sub-grid scale. As such, the relation of them to cavitation erosion may be linked, however they are computationally intensive or currently plainly unfeasible to simulate. This is especially true for industry work that requires a quick turnaround time.

For flows near walls, the spherical collapse assumption becomes unrealistic. Blake et al [14] studies such cases utilizing the boundary integral method, which could recreate a jet entering the bubble that had been seen in previous experiments. It was noted the asymmetrical collapse of these bubbles was due to asymmetric flow fields caused by a boundary or other bubbles. Their simulation results compared well to experimental data for a single bubble collapsing near a wall. They also showed some interesting results with similar asymmetric phenomena in cloud cavitation.

1.2.3 - Cavitation models

One of the early numerical cavitation models was presented by Kubota et al [15] in 1992. The authors used the RP equation to calculate the expansion and collapse of vapour. They neglected surface tension and viscosity and considered the liquid and the vapour as an incompressible mixture. The authors also considered sub-grid scale bubble interaction. They simulated flow around a cavitating hydrofoil at various angles of attack and compared their CFD results to experimental data. They were able to show that vortex generation and transport were greatly influenced by baroclinic torque generated cavitation. It should be noted though that the authors did report numerical errors in some cases.

Another early model was presented by Chen and Heister [16] in 1995. The authors used a model like Kubota et al [15], with a mixture model and sub-grid scale consideration of the bubbles. However, they considered the bubbles nuclei per unit mass to be constant. This meant that once a bubble would expand, the number of nuclei diminished, and vice versa. Another improvement was the treatment of the pressure field surrounding a bubble. The RP equation assumes a far-field pressure, which is not valid when multiple bubbles are expanding in the same region. To compensate for this, Chen and Heister used the average pressure in the sub-cell and solved a finite domain form of the RP equation. The simulations by Chen and Heister showed good agreement with initial 2D studies and on a 2D single holed injector-like orifice. However, there were some doubts about stability and CPU cost.

An early development in modelling cavitation was the introduction of a barotropic model by Delannoy and Kueny [17]. They used an inviscid single-fluid Euler model solved with the finite volume method. The local value of the vapour fraction was determined by the quantity of liquid and vapour, thus resulting in a mixture. As the model was inviscid, turbulence was not considered. In a 1D Venturi nozzle the results were inaccurate. However, a 2D simulation of a Venturi nozzle gave qualitative results that compared well to experimental data. While the vapour cavity did detach and collapse downstream in both the simulations and experiments, the frequency of detachment was significantly lower in the CFD. This also meant that the cavity length was typically larger. Even so, they were able to decipher an important aspect of cavity detachment, that is, the re-entrant jet was likely an inviscid phenomenon.

Schmidt et al [18], [19] went on to develop a model further relating the pressure with density and the speed of sound of a liquid-vapour mixture. The calculations utilized the speed of sound equations developed by Wallis [20]. The authors presented the idea that compressibility is desirable for numerical stability with cavitating flows. This would also allow simulations to predict effects of kinetic energy from violent vapour collapses. However, the authors admit that barotropic based models may have issues with large-scale low speed cavitation due to the gradual density change and pressure gradients. As such, Schmidt et al worked with simple 2D nozzles with high speed flows. They included an artificial viscosity but did not take turbulence into account. The predicted discharge compared well with experimental values from literature at various cavitation numbers. However, the oscillation or shedding behaviour was not captured in the simulations. They were able to show some cyclical behaviour once they switched to a simplified valve covering orifice nozzle, although the boundary conditions were questionable with part of the entrance assumed to be a wall. It is noted here that turbulence is a critical component of flows within injectors, particularly so in terms of how turbulence affects cavitation and is discussed in an upcoming section.

It is clear from the previously mentioned early studies the effects of turbulence were frequently neglected. There have been some studies that attempt to include it and correct any issues pertinent to cavitating flows. A later cavitation model, based a barotropic equation, was presented by Reboud et al [21] with later improvements by Coutier-Delgosha [22]. The liquid and vapour were both considered compressible through their equation of state (EoS). Simulations were solved with the pressure-based method and the simple solver. The 2D models were tested on Venturi like nozzles with unsteady Reynolds-averaged Navies-Stokes (URANS) model. They were able to show differences between a standard and modified RNG k-ε turbulence models. The simulations with the modified RNG k-ε turbulence model were much more capable of resolving the transient nature of the flow and showed good agreement to experimental data. The modification to the turbulence model essentially reduced the viscosity in the mixture which allowed for a re-entrant jet to easily develop. This is in line with Delannoy and Kueny [17] who argued a re-entrant jet was likely an inviscid phenomenon. While perhaps not entirely inviscid, at least according to [21] and [22], the development of a re-entrant jet does appear to depend on the level of viscosity. This is not considering the mainstream flow where viscosity has an obvious effect and is linked to The Reynolds number (Re).

1.2.3.1 - Fluent cavitation models

The models discussed above are some of the pioneering works for cavitation models. There have been several other models developed and improvements made over the years. Some of the more commonly used models (and that are a part of ANSYS Fluent) will be discussed thusly. These are the Sauer and Schnerr [23], Singhal et

al [24], and Zwart et al [25] (termed ZGB). These three models account for the vapour production with a source term originally based on the RP equation, and are so called bubble-based cavitation models.

Sauer and Schnerr [23] utilized a modified form of the classic volume of fluid interface capturing method as a mixture equation. The cavitation model is similar to the model of Chen and Heister [16], in that the number of nuclei are dependent on the bubble sizes, or rather the vapour fraction. With this, Sauer and Schnerr were able to simulate a 2D NACA 0015 aerofoil, neglecting turbulence and viscosity, to study the cavitation dynamics. They were able to show that their cavitation model could resolve unsteady cyclical behaviour of cavitation shedding along with re-entrant jets dynamics. Later publications [26] included improvements and the use of a k-ω turbulence model in a single hole injector-like nozzle with sharp edges. They showed that, with adjustments to the cavitation model parameters, the cavitation structures qualitatively agreed well with experimental observation.

Singhal et al [24] proposed another bubble-based cavitation model which assumed a constant bubble density. The mixture model is again utilized, but solves for the vapour mass fraction, instead of the volume fraction. Like other bubble-based models, it also uses the RP equation to account for bubble growth and collapse. Interestingly though, the cavitation model also accounts for non-condensable gas. The researcher used the cavitation model, coupled with a k-ε turbulence model, to compare CFD results against different experimental geometries. The model performed well in terms of pressure distribution. For example, when compared to experimental data for a sharp-edged orifice, the Cd values were in good agreement.

Finally, the ZGB cavitation model [25] is discussed, which is the model used for the Control Orifice and Shoe & Guide work. It is again based on a simplified RP equation, with surface tension, viscosity, and second order terms assumed negligible. It is an Eulerian model, which is essentially simplified to a single homogeneous mixture of liquid and vapour. Like the Sauer and Schnerr model, it solves for the volume fraction, rather than the mass fraction, like the Singhal model. In [25], the authors coupled it with a modified k-ε turbulence model and simulated a cavitating flow with a hydrofoil, inducer, and Venturi nozzle. Importantly, the modified k-ε turbulence model allowed for shedding, following the arguments of Rebound et al [21].

Of the three geometries originally investigated, the hydrofoil at one-degree angle of attack is considered first. The ZBG cavitation model produced low amounts of vapour and the CFD results agreed very well with the experimental data. However, once the angle of attack was increased to four degrees, with more vapour being produced, the cavitation region was under predicted when compared to experimental data.

Secondly, three different flowrates for the inducer were tested with the ZGB cavitation model. Visually, the simulated cavitation was quite reasonable. The head drop-off curves for all three conditions were also in close

agreement to the experimental results. However, some inconsistency in the timing of the head drop was present.

The final geometry the ZGB cavitation model was originally tested on was a Venturi nozzle. While they were able to closely match the Strouhal number (St), they had to calibrate some of the constants in the cavitation and turbulence equations for a better qualitative comparison. Although tuning was needed, it was still encouraging that the shedding behaviour could be modelled.

1.2.3.2 – ZGB cavitation model coefficients

Concerning the tuning of the cavitation model, the ZGB model has four coefficients that can enable the tuning of the evaporation and condensation rates. Work by Lui et al [27] investigated the importance of tuning these coefficients. They simulated a centrifugal pump while varying one coefficient. The simulations were done with RNG k-ε to resolve the turbulence and the ZGB cavitation model. They were able to find close agreement to experimental data if the condensation coefficient was lowered by two orders of magnitude. This is likely because RANS models tend to over predict pressure recovery. As such, a certain amount of tuning can be beneficial, though this can be a long process and the same coefficients will not work for every simulation.

1.2.4 – Turbulence models and cavitation

RANS and URNAS simulations have been popular within industry due to time constraints and computational power needed to run them. LES, DES and WMLES, among other models, have improved and gained more feasibility to run in a timely manner, but these turbulence models still have a high computational demand. However, advanced CFD models resolve transient large scale turbulent structures and show much more detail in the flow, as compared to RANS or URANS [28] [29] [30] [31]. LES modelling techniques have been specifically shown to be superior to RANS and URANS in capturing vortex structures in cavitating flows in high-pressure fuel systems (for example Bush et al [32], Gavaises et al [33], and Koukouvinis et al [34]). However, this does not indicate that RANS and URANS simulations are unhelpful or that RANS and URANS will not be utilized in the years to come. In fact, there has been a significant amount of work into combining RANS and LES turbulence models, (see selectively [35], [36], [37] and [38]). By creating a hybrid model and reducing the computational need of pure LES simulations there is a greater likelihood of these hybrid models being used within industry.

Koukouvinis et al [39] tested different turbulence models with different cavitation models at several pressure drops and compared those results to experimental data. They found that RANS produced less accurate results at low pressure drops. They also confirmed that SST turbulence model offered the best compromise between

k-ε and k-ω. Obviously though the most accurate results were with LES turbulence models. Concerning cavitation models, they found that using the default values for ZGB and Sauer and Schnerr cavitation models tended to give unrealistically steady vapour structures. If the mass transfer rates were increased, they began to behave more like a barotropic model and display more realistic broken-up vapour structures. This has also been shown to reduce unrealistic negative pressure predicted [40].

Gavaises et al [41] studied flow on a common test geometry. They compared URANS and LES simulations to experimental data, focusing on the distribution of vapour. They found that URANS was unable to accurately predict the shedding. As such, URANS may not be appropriate to predict cavitation erosion as smaller scale eddies would need to be resolved. However, a recent modification to the URANS equations, as proposed by Reboud et al [21], has been shown to enhance cavity shedding. Edelbauer et al [42] was able to show situational applicability with RANS and URANS models with high pressure flows in microchannels using this Reboud correction.

Certain consideration should be given to laminar flows that cavitate. Soteriou et al [43] [44] demonstrated that a laminar approach to an orifice can still cavitate and will have a significant effect on the form of the cavitation where the vapour pocket is intact and less like a cloud of small bubbles. After the collapse of cavitation, the flow will inherently have unsteadiness and turbulence.

1.2.5 – Interaction of fluid property and cavitation

The fluid properties can have a significant effect on cavitation and cavitation erosion. The need for representative EoS at high pressures has increased as injection pressures are now reaching 3000 bar [45] [46] and simulations working on pressures upwards of 4500 bar [see IPPAD project]. However, current data for diesel or ISO4113 (calibration fluid used in the automotive industry) only go up to 2000 bar [47]. This issue is made worse still when considering cavitation collapse pressures, which have been recorded up to 10,000 bar in both experiments [48] and in simulations [10].

1.2.5.1 - Viscosity

The importance of viscosity can easily be demonstrated if the Re is considered with the characteristic length, which is the bubble diameter, approaches zero. This would indicate a heavily viscous-dominated flow and would likely slow the collapse. This is consistent with Nour et al [49] who examined viscosity and showed that lower viscosity relates to higher mass loss during cavitation erosion. The team showed that water is a good erosive fluid and theorized it was due to its small molecular size, heavy molecular weight, high vapour pressure, low viscosity and air solubility. These factors, along with a fast rate of phase change, lead to high

vapour implosion velocities. The authors proposed that complex molecules and non-homogeneous liquids typically have a lower density and less defined phase change behaviour. This would decrease their ability to cause cavitation erosion.

Work recently published in a PhD thesis by Naseri [50] has shown that cavitation is closely linked to viscosity. The author investigated viscoelastic effects on cavitation on a step nozzle and injection nozzle. They found that the addition of a viscoelastic additive helped to suppress cavitation while increasing the flow rate when compared to a Newtonian fluid.

1.2.5.2 - Molecular adhesion

On the importance of surface tension, Lord Rayleigh [8] indicated that it was likely unimportant and so neglected it. Indeed, Franc & Michel [6] demonstrated that it is only important during the final stages of collapse for some scenarios. However, Iwai & Li [51] showed that increasing the surface tension led to an increase in the cavitation damage. They did this by adding a wetting agent to water to reduce the surface tension while maintaining the density and viscosity. However, they did not indicate the effects of vapour pressure from this. They deduced that the increased surface tension led to more symmetrical and larger bubbles, which could have more power during collapse. This was later studied numerically as idealized cases by Zhang & Zhang [52] and further experimentally by Liu et al [53]. These researchers found that erosion rises sharply by increasing the surface tension.

Concerning just cavitation and not erosion, work by Theodorakakos et al [54] showed that just small changes in fuel properties could have significant changes in vapour production. The researchers compared experimentally a heavy fuel to a light fuel, each cavitating at different pressures, and then examined the cavitation with a fuel mixture. After adding just 1% of the light fuel to the heavy fuel, the mixture cavitated in a remarkably similar way as the pure light fuel.

Indeed, while the physical interface of the liquid and vapour may seem like a perfect surface, it is in fact a transitional region. Temperley and Trevena [55] describe this area to be around 3 Å thick for water. However, during cavitation this region will grow which further complicates the implementation of surface tension in simulations. Complex fluids, like diesel and ISO4113, will also likely have a thicker transition region.

1.2.5.3 - Temperature

The issue of temperature is lastly discussed in this section. In many simulations the fluid properties are solely dependent on pressure and considered isothermal. While this assumption may be valid for many simulations,

significant temperature rises can be generated during cavitation collapse. McNamara III et al [56] confirmed temperatures close to 5000K by examining the light given off during bubble collapse, termed sonoluminescence. However, these temperature spikes are only located in small specific regions and are only present for short times. Indeed, work comparing adiabatic and barotropic simulation give near identical overall results (See [57] and work from the CaFE project). While the temperature may have a global impact on fluid properties, in terms of erosion it is likely negligible for most current cases.

Temperature changes may become more important in future work, specifically concerning higher injection pressures. While temperature changes due to cavitation appear to be negligible, temperature effects from viscous heating can be important, specifically in narrow channels. Strotos et al [58] studied the temperature effects inside an injector and found a significant increase in temperature due to viscous shear over the whole injection period when comparing an injection of 2000 bar to 3000 bar.

1.2.6 - Cavitation Erosion

The actual processes that lead to erosion in a cavitating flow are complex, but there are two generally agreed upon mechanisms. They are the micro jet, caused by eccentric bubble collapse (Fig. 1.3), and radiated acoustic pressure, generated by a shock wave after bubble collapse. However, no matter the dominating process, it can be agreed that erosion is caused by the release of energy from the vapour bubble collapsing near a surface. If enough energy is released, then the surface will experience a localized area of plastic deformation or induced fatigue. The accumulation of stress within the surface eventually leads to localized failure of the material, leading to the material being eroded away [59].

Attempting to predict the removal of material from the solid boundaries of real components is a significantly greater challenge still. Recent numerical research on potential material damage focusses on the collapse of a single bubble on a simple flat surface [60] [61]. These works calculate either the plastic strain or the plastic deformation and do not extend into material removal. Predicting the removal of material from actual components, particularly those of hardened steel, will heavily depend on manufacturing processes, geometry and assembly of the component, the effects of which are not currently accounted for in published research.
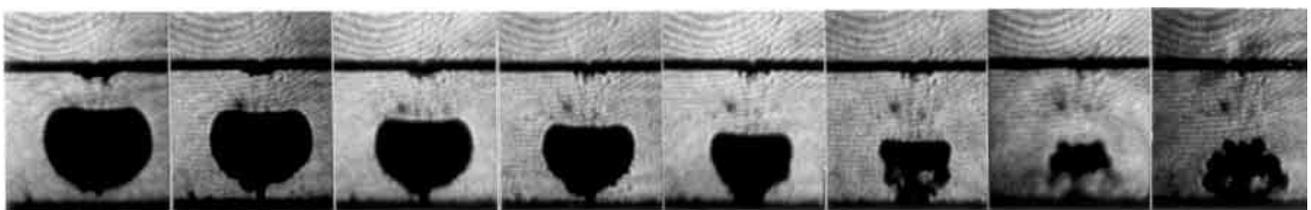
Fig. 1.3 – Progressive collapse of an eccentric bubble near a wall. Image from Shima et al [130]

1.2.6.1 - Stages of cavitation erosion

Nour et al [49] described three main stages to cavitation erosion. The authors proposed that the stages are incubation, acceleration and maximum rate. During the incubation stage the hardware surface experiences impact loads resulting in cracks developing and surface deformities. This stage has little mass loss. During the acceleration phase, the mass loss increases with further crack development and further cyclical loading on the hardware wall. Finally, during the maximum rate stage, the mass loss is at a terminal value with larger particles being removed. The erosion process is not only affected by the material hardness, but also grain size, shape and roughness [3] [49]. It should be noted though that for many real-world components (like those in the fuel injection industry), the rate of mass loss is not of interest since any erosion means component failure due to breakage or not performing to desired specifications.

There are several ways to quantify the cavitation collapse intensity. Some researchers have used pressure sensors to measure the energy released [48] [62], while others measured the surface topography before and after a set amount of time in cavitating flow [3]. Franc et al [3] categorized the cavitation aggressiveness by load, as well as indentation diameter, with before and after topography measurements. This provided a useful means to categorize levels of cavitation, but only when little cavitation damage was present. From this they were able to determine that the number and size of indentations were heavily linked to flow velocity.

1.2.6.2 - Material properties

It is generally agreed that the harder the material is, the less susceptible it is to erosion. However, it is not that simple. Franc et al [3] attempted to relate the pitting rate to the materials elastic limit, but no solution was found. The authors showed that a simple micro indentation test would not provide an accurate representation of a material toughness when subjected to high strain rates. It is likely due to the lack of data regarding material properties under the necessary time scale and strain rates. They concluded that there are great changes in yield stress when under high strain rates. However, this is likely more important for steel rather than aluminium.

In more recent work, Cadoni and Forni [63] tested three different steels with 4 different strain rates ranging from almost zero to 1000 s^{-1}. They showed that an increased strain rate resulted in an increased stress and ultimate tensile strength. The authors only experimented in tension though, while cavitation erosion would mainly result in compressive forces.

Variations in surface properties are also important. Vinogradova et al [64] experimented with laser induced cavitation in a narrow gap bounded by two plate. One test was with hydrophobic plates and then another with hydrophilic plates. The data showed that the hydrophobic surfaces tended to enhance the cavitation initiation

threshold. The reason for cavitation to occur more readily was determined to be gas-filled submicrocavitaties. This further highlights the complexities with the fluid structure interactions.

1.2.6.3 - Erosion risk indicators (ERIs)

Lord Rayleigh [8] indicated that large pressure values occur during vapour collapse. Indeed, researchers have shown that the pressure can exceed 10,000 bar [48] [65]. Many researchers have analysed CFD results and calculated parameters to correlate with the erosion. As detailed below, some of those studies focussed on direct forces, like peak pressure attained during vapor collapse, whilst others investigated indirect indicators, like the rate of change of pressure or potential power. Although some success has been shown, at this time there is no overall reliable ERI.

Gavaises et al [33] conducted one of the first cavitation erosion studies in fuel injection components and used a bespoke Eulerian-Lagrangian CFD model. They tested two different injector designs that experienced severe erosion in different locations. They were able to show some correlation with the acoustic pressure and liquid volume fraction.

In early experiments by Soda & Tanaka [66], the rate of pressure change appeared to be a likely deterministic factor for cavitation erosion. This idea was investigated numerically by Koukouvinis et al [67] [68]. The researchers considered the material derivative of pressure and of liquid volume fraction to investigate erosion in diesel injectors using a commercial Eulerian code. They were able to show some success in predicting regions at risk of cavitation erosion. Nevertheless, there were some discrepancies with the experimental data which they attributed to the cavitation model. Furthermore, there were no non-eroding designs to compare with to confirm the results.

In other works, Koukouvinis et al [69] used two ERIs applied to two different nozzles with different sac sizes. Both designs experienced erosion, but in different locations. One design experienced erosion around the needle in the sac region while the other design had erosion in the nozzle orifices. Two ERIs were applied to these designs. One was termed the cavitation aggressiveness index, based on the rate of change of vapour fraction and of pressure. The other ERI was related to the radiated acoustic pressure proposed by Wang and Brennen [70]. The researchers were able to correlate some regions more likely to experience cavitation erosion with both ERIs when compare to images of erosion from hardware. However, not all the regions predicted by the ERIs compared well to the experimental images.

Finally, to improve the cavitation model and limit the negative pressure predicted in the CFD, Koukouvinis et al [34] [40] increased the mass transfer rate (R) by increasing the constants in the ZGB cavitation model. This was run in conjunction with a liquid compressible LES hybrid model during the opening phase in an injector.

With this change to the cavitation model, they were able to show that the maximum values of static pressure correlated well with regions of erosion from experimental tests. However, relying on absolute values of peak static pressure could lack robustness with the current state of CFD development. Furthermore, there were again no designs without erosion to provide a benchmark case in this investigation.

Other methods attempting to predict risk of erosion utilize the energy of the vapour collapse. Franc and Michel [6] and Fortes-Patellar et al [71] [72] each considered different energy aspects of bubble collapse and how energy is imparted to a nearby solid surface. The ERIs proposed by these researchers have shown promise. However, these methods appear only to have been applied to a limited degree to industrial designs. They are also lacking non-eroding design to benchmark and confirm their results.

Considering the definitions of some ERIs, it may be expected that there will be some dependence on the resolution of the numerical grid used in the CFD simulations. Indeed, Mihatsch et al [73] explored the effects of mesh refinement on a possible ERI related to maximum pressure. They ran a parametric study with simulations of three different mesh refinements on a well-studied test geometry. The researchers showed that continued mesh refinement resulted in resolving smaller scale vapour structures, though this did not have a major impact on their ERI results. While agreement with experiments was achieved, the CFD results were calibrated using a scaling factor. Furthermore, there was once again no non-eroding design to compare and confirm their results to.

1.2.7 - Vapour shedding

In general, experiments have shown that there are two mechanisms that lead to bulk vapor shedding and occur under different flow conditions. One is termed re-entrant jet and typically occurs when the attached or partial cavity is relatively short. A re-entrant flow from the cavity closure region extends to the cavity start and causes the vapor to be pinched off and shed. This has been well documented by Knapp [74] and Furness & Hutton [75] in earlier years, and more recently by Foeth et al [76]. Further experimental studies have been conducted on the re-entrant jet velocity by Pham et al [77] and Stanley et al [78] and on the effects of obstructing the jet by Kawanami et al [79].

The other shedding mechanism is termed condensation or bubbly shock and typically occurs when the running conditions have enabled the attached vapor region to extend further downstream. The phenomenon was first suggested by Jakobsen [80], and can be triggered when a pressure wave, produced downstream from the collapse of previously shed vapor, propagates upstream. This produces a condensation front which travels up the attached vapor region, causing the vapor progressively to detach and partially collapse as it transitions to a shed vapor cloud. This mechanism has been well studied on wedges and other pseudo two-dimensional

geometries by Campbell & Pitcher [81], Riesman et al [82], Laberteaux & Ceccio [83] and more recently by Wang et al [84] and numerically by Budich et al [57].

The two shedding mechanisms are well documented on hydrofoils. Arabnejad et al [85] investigated the re-entrant jet shedding mechanism on a NACA 0009 hydrofoil, both by experimental means and by simulations. They were able to demonstrate good agreement between the CFD and the experimental data in terms of shedding frequency, cavity length and overall vapor structure. The transition between the different shedding mechanisms was shown well by Arndt et al [86] who studied flow over a NACA 0015 hydrofoil, also by experimental and numerical means. The researchers were able to demonstrate a sharp change in the shedding mechanism by changing either the cavitation number or angle of attack, which altered the amount of vapor produced.

Both shedding mechanisms have also been documented on a wedge, for example by Ganesh et al [87]. These researchers used time-averaged X-ray densitometry to illustrate both the re-entrant jet and condensation shock shedding mechanism. For the latter mechanism, they showed the shock front moving through the attached vapor region. Once the condensation front reached the wedge apex, the remaining vapor was shed downstream, and the process repeated.

The wedge used by Ganesh et al [87] was investigated with CFD by Budich et al [57]. Their investigation focused on the condensation shock regime, and they achieved good correlation in terms of shedding frequency and cavitation distribution with the experimental data. However, their results showed a significantly higher pressure drop than in the experiments. They attributed this in part to the two-phase model chosen which inhibited pressure recovery.

Tummler et al [88], following work by Sou et al [89], and Bicer and Sou [90], studied the two shedding mechanisms in an asymmetric rectangular cross-section orifice. While not investigating the shedding frequencies, the authors were able to model the two shedding mechanisms using Large-Eddy Simulations (LES).

The shedding mechanisms were also investigated in an axisymmetric converging diverging Venturi nozzle. Hogendoorn [91] and Jahangir et al [92] used high-speed imaging at different flow conditions and characterized a re-entrant jet shedding regime, a condensation shock shedding regime and a transition zone between them. When there was a small amount of vapor present near the orifice throat, they identified the shedding mechanism as re-entrant jet. As the running conditions were changed to produce more vapor, they reported that the shedding mechanism transitioned to condensation shock. They found that the re-entrant jet shedding mechanism had a much higher shedding frequency than the condensation shock mechanism. Jahangir et al [93] went on to collect time-averaged X-ray computed tomography (CT) data of the Venturi at

two running conditions which were expected to produce the two shedding mechanisms. With this, the authors explored the averaged internal cavitation structures and the vapor distribution.

The Venturi nozzle used in Jahangir et al [92] was investigated with CFD in a Master Thesis by Cointe [94]. This work showed some vapor contours that appeared to distinguish the different shedding mechanisms but did not demonstrate the relatively high shedding frequencies for the re-entrant jet mechanism. Moreover, as in the work of Budich et al [57], the Cointe was also unable to produce the pressure drops that were seen in experiments.

1.2.8 - Cavitation within thin fluid filled gaps

There are numerous articles on the dynamics of a solitary bubble close to a single wall (see selectively [10], [14] and [95] among many others). However, the dynamics are significantly different when cavitation is considered in a narrow, liquid filled gap between two walls, which exist for example, in bearings [96], engine cylinders [97] and biological joints [98]. Erosion caused by such cavitation has been observed on the boundaries of such gaps, in hardware like gear pumps [99], bearings [100] and engine cylinder liners [101]. However, there is an absence of literature applying cavitation ERIs to these cases.

An early work by Parkins & Stanley [102] studied cavitation in an oil film between two oscillating surfaces. They found a characteristic "fern" pattern of vapour was produced. This pattern was also shown by Dellis & Arcoumanis [97], in the early stages of cavitation development in the lubrication film between a piston ring and cylinder liner. They went on to show that at higher engine speeds the film thickness would vary, and so different patterns would be formed.

Gonzalez-Avila et al [103] studied cavitation in a thin gap without considering potential erosion. They looked at bubble dynamics between two close parallel surfaces by experimental means. The study used laser induced cavitation and examined the dynamics when a bubble was in contact with one or both walls. They observed that bubbles contacting both walls adopted a cylindrical shape during collapse. These bubbles were produced in a gap of about 50µm. The authors also showed that the bubbles contacting both sides collapsed more slowly than bubbles that were only in contact with one side. Moreover, they point out the importance of viscosity in sandwiched bubbles, which is likely to play an important role in collapse time, and thus the energy of collapse.

The effects of viscosity during cavitation collapse within a thin gap were also studied by Quinto-Su et al [104]. They similarly studied laser-induced bubbles in thin gaps experimentally. The authors' work was concerned with biological uses and so used gap widths of 15 to 400µm. They found that for bubbles created with the same amount of energy, a smaller gap width resulted in an increase in the lifetime of the bubble.

A similar case was investigated numerically by Hsiao et al [105] who simulated the collapse of a bubble in contact with two parallel plates. This enabled their 25µm gap to be more thoroughly visualized than in experimental studies. Their simulations showed that the centre region of the bubble collapses faster than the regions near the walls. This results in an hourglass shape near the end of the bubble collapse. Eventually, the vapour region splits into two hemispherical shaped bubbles, one on each wall. This would indicate that cavitation induced erosion is possible on both walls. Moreover, while it is generally accepted that in the case of a spherical bubble collapsing the surface tension is insignificant [6], Hsiao et al concluded that the effects of surface tension are even less in the bounded bubble.

1.2.9 - Cavitation in control orifices

An injector, and particularly the fuel injection process, is not a straightforward task to model. However, the injector is a key factor in emissions. Mitroglou et al [106] and Winterbourn et al [107] both examined transparent real-size nozzles experimentally. They were able to show that vapour bubbles fill the sac volume caused by the closing of the needle at the end of injection. This was further complicated by air entering the sac at the end of injection. These factors will affect the cycle-to-cycle reproducibility and emissions.

A method used to recreate the cavitation structures in small orifices is to use large scale models (LSMs). It has been shown that scale models of orifice flow within the high-pressure fuel system can act reasonably independent of scale. This is assuming pressure and CN are also scaled accordingly (see selectively [44] and [108]), although it is know that Re will not scale in the same manner.

Bush et al [32] scaled a hydraulic orifice to 40 times from real-size with CFD results showing similar flow structures between the CFD real-size model, CFD LSM and experimental LSM. While the LSM URANS simulation did not show the correct shedding, more advanced DES models did show the shedding. They were able to correlate the simulation to the experimental LSM data. From there they were able to simulate the real-size orifice and determine the shedding frequency.

The orifice and entry shape greatly affect the flow and injector spray shape. Soteriou et al [109], [110] examined nozzle hole shape extensively. The researchers demonstrated the effects on cavitation that tapering and entry rounding of the nozzle holes had, with higher rounding and higher converging taper reducing the amount of cavitation.

The needle movement is a factor that should also be considered. The transient nature of the injection cycle have been shown well by Orley et al [111], who utilized an immersed boundary method on a three-phase, 9-hole diesel injector, and by Payri et al [112], who demonstrated possible effects of cavitation on the mass flow

rate, among many other works. This sudden closing of the needle can cause cavitation and can lead to erosion of the needle seat.

As injectors and the fuel line are made of metal, traditional methods of visualization, like x-ray and CT scans, are not suitable. New methods are being introduced though, and some new techniques show promise. Neutron imaging can image through a metal injector, but still needs further development to achieve high enough imaging speed rather than averaged images [113]. Neutron imaging may even have applications in imaging chalking and deposition within an injector, but this is beyond the scope of this work.

1.2.10 - Gaps in the literature

While there are some numerical models that include fluid-structure interaction (see selectively [60], [61] and [114]) there is currently no reliable way to directly simulate cavitation erosion. This is in part due to complications and unknowns of how the surface materials respond to cavitation collapse. The materials microstructure, grain size, modes of plastic deformation, etc. all play a large role. There is also the question of a reliable fatigue model. Furthermore, due to the rate and scale at which micro-jets and shockwaves transpire, a strain-rate needs to be inferred as there is currently little data, if any, available. However, what is needed first is a reliable model that can determine the location and severity of erosion. Therefore, cavitation risk assessment, in the form of ERIs, are investigated in this thesis. Moreover, understanding the characteristics of cavitation itself are studied.

Previously published ERIs have been studied but remain unreliable. All the published material shows reasonable correlation between eroded hardware and CFD results. However, there are no papers exploring the ERIs on similar non-eroding components or under non-eroding running conditions. This step is essential in determining how reliable prospective ERIs are.

1.3 - Objective

In the proceeding chapters, cavitating flows in three different components have been simulated. The components were a Venturi nozzle, a thin gap within a high-pressure fuel pump (Shoe and Guide), and a Control Orifice within a diesel injector (SPO). From this, different characteristics of cavitation have been thoroughly examined and the CFD results compared to experimental data. The overall aim of this work is to further the understanding of cavitation and to develop more reliable and accurate methods to predict regions at risk of cavitation erosion. The separate objectives are summarised as:

• Investigate characteristics of cavitation with state-of-the-art methods.

- Further the understanding of cavitation shedding characteristics.

- Propose potential cavitation erosion risk indicators (ERIs) and implement them in CFD simulations.

- Validate the potential ERIs against actual hardware results for eroding and non-eroding designs.

- Determine which potential ERIs can reliably predict regions at risk of cavitation damage.

- Assess the transferability of the ERIs with different flow conditions and simulation methods.

- Simulate cases of industrial interest which have a direct real-world impact.

1.4 - Outline

The main body of this thesis is divided into the following sections. In chapter 2, the methodology is given for the proceeding chapters, with a focus on cavitation and the ERIs tested. An overview of the three components tested and their respective results, (the Venturi nozzle, the Shoe and Guide and the Control Orifice) are presented chapters 3, 4 and 5. In chapter 6, the conclusions are summarised and future work proposed.

2 - Simulation background and methodology

The governing equations and numerical methods used in the simulations are described in this chapter. The simulations solved for conservation of mass and momentum, along with turbulence, fluid properties and phase change. The equations are typically considered as a parabolic and hyperbolic mix. For the Venturi nozzle component, a barotropic single-fluid model for water and water-vapour (section 2.3.1) was used. For the thin gap in the Shoe and Guide assembly and the Control Orifice, fluid properties of ISO4113 (Normafluid) were simulated and are discussed in section 2.3.2. The EoS for Normafluid was implemented as a mixture model and was coupled with the ZGB cavitation model, which allowed for adjustments to the mass transfer rate (R). The potential for cavitation damage was explored with various erosion risk indicators (ERIs), described in section 2.6. The simulations were all performed in ANSYS Fluent, V17 using a pressure-based finite volume solver. User defined functions were implemented where there was not a suitable built-in model available and are noted in the appropriate sections. See Appendix A for the specific procedure followed for each component simulated.

2.1- Governing equations

The CFD simulations solved the standard equations for mass (Eq. 1) and momentum (Eq. 2) conservation:

$$\frac{\partial \rho}{\partial t} + \boldsymbol{\nabla} \cdot (\rho \, \boldsymbol{U}) = 0 \qquad \text{Eq. 1}$$

$$\frac{\partial (\rho \boldsymbol{U})}{\partial t} + \boldsymbol{\nabla} \cdot (\rho \boldsymbol{U} \boldsymbol{U}) = -\boldsymbol{\nabla} p + \boldsymbol{\nabla} \cdot (\bar{\bar{\boldsymbol{\tau}}}) \qquad \text{Eq. 2}$$

where $\boldsymbol{U}$ is the velocity vector field, t is time, p is pressure, ρ is the density and $\bar{\bar{\boldsymbol{\tau}}}$ is the stress tensor. Gravity is neglected in this work as it is deemed negligible when compared to the flow velocity and characteristic lengths. The stress tensor, which includes viscous stress and stress due to dilation of the fluid, is given as:

$$\bar{\bar{\boldsymbol{\tau}}} = \mu \left[\left(\boldsymbol{\nabla} \boldsymbol{U} + (\boldsymbol{\nabla} \boldsymbol{U})^T \right) - \frac{2}{3} (\boldsymbol{\nabla} \cdot \boldsymbol{U}) \boldsymbol{I} \right] \qquad \text{Eq. 3}$$

where μ is the fluid viscosity and $\boldsymbol{I}$ is the unit tensor.

RANS models apply an ensemble averaging to the governing equations to solve for the mean velocity ($\overline{U}$) using a Farve-averaging (density weighted technique). Utilizing an index notation ($\boldsymbol{U} = (U_i) = (u, v, w)$) and $U_i = \overline{U}_i + U_i'$ for the mean and fluctuating components, the governing equation can now be written as:

$$\frac{\partial \rho}{\partial t} + \frac{\partial (\rho U_i)}{\partial x_i} = 0 \qquad \text{Eq. 4}$$

$$\frac{\partial (\rho U_i)}{\partial t} + \frac{\partial (\rho U_i U_j)}{\partial x_j} = -\frac{\partial \rho}{\partial x_i} + \frac{\partial}{\partial x_j}\left[\mu\left(\frac{\partial U_i}{\partial x_j} + \frac{\partial U_j}{\partial x_i} - \frac{2}{3}\delta_{ij}\frac{\partial U_l}{\partial x_l}\right)\right] + \frac{\partial \left(\rho \overline{U_i' U_j'}\right)}{\partial x_j} \qquad \text{Eq. 5}$$

where U indicates the mass-averaged velocity and δ_{ij} is the Kronecker delta. Averaging the governing equations in this manner introduces terms known as the Reynolds stresses, which are solved using different turbulence models.

The LES models do not average the variables, but instead filters them, which results in a similar set of equations.

$$\frac{\partial \rho}{\partial t} + \frac{\partial (\rho \widehat{U}_\iota)}{\partial x_i} = 0 \qquad \text{Eq. 6}$$

$$\frac{\partial (\rho \widehat{U}_\iota)}{\partial t} + \frac{\partial (\rho \widehat{U}_\iota \widehat{U}_J)}{\partial x_j} = -\frac{\partial \hat{p}}{\partial x_i} + \frac{\partial}{\partial x_j}\left[\mu\left(\frac{\partial \widehat{U}_\iota}{\partial x_j} + \frac{\partial \widehat{U}_J}{\partial x_i} - \frac{2}{3}\delta_{ij}\frac{\partial \widehat{U}_l}{\partial x_l}\right)\right] + \frac{\partial \tau_{ij}}{\partial x_j} \qquad \text{Eq. 7}$$

where $\widehat{U}$ indicates the filtered velocity. From here, turbulence models are again applied. These will be discussed briefly for completeness in the following subsections. However, further information can be found in [115].

2.2- Turbulence modelling

Turbulence is characterized by chaotic changes in pressure and flow velocity resulting from the kinetic energy overcoming the dampening effects of viscosity. The energy is dissipated in eddies, which vary in size, with the larger ones carrying more energy. The energy is transferred from the larger eddies down to the smaller ones through an energy dissipative process known as "energy cascade" by a means of vortex stretching. The energy is finally dissipated as heat. [116]

There are several models that attempt to emulate the effects of turbulence. The more simplified models are based in RANS and only capture the more energy dominant eddies. Other more advanced turbulence models attempt to resolve smaller scale eddies but require significantly more computational resources. Background information is provided below for the turbulence models used for the different components with further details in relevant chapters.

2.2.1 – Realizable k-ε turbulence model

The realizable k-ε turbulence model was used primarily for the RANS/URANS simulations and for any initialization in this work. RANS turbulence models solve for the Reynolds stresses $(-\rho\overline{U_i'U_j'})$ assuming isotropic turbulence and employ the Boussinesq eddy viscosity hypothesis [117], which assumes the Reynolds stresses are proportional to the mean strain rate [115]. The Reynolds stress is defined as:

$$-\rho\overline{U_i'U_j'} = \mu_t\left(\frac{\partial U_i}{\partial \mathrm{x}_j} + \frac{\partial U_j}{\partial x_i}\right) - \frac{2}{3}\left(\rho k + \mu_t\frac{\partial U_k}{\partial \mathrm{x}_k}\right)\delta_{ij} \qquad \text{Eq. 8}$$

where k is the turbulent kinetic energy and μ_t is the turbulent viscosity. The turbulent viscosity is solved as

$$\mu_t = C_\mu\rho\frac{k^2}{\varepsilon} \qquad \text{Eq. 9}$$

where C_μ is a model variable (rather than a constant, as in other k-ε models). The realizable k-ε model has an improved formulation of the turbulent viscosity and transportation equation for ε [115].

The realizable transport equations were derived from vorticity fluctuations by Shih et al [118], defined as:

$$\frac{\partial(\rho k)}{\partial\mathrm{t}} + \frac{\partial(\rho kU_j)}{\partial x_j} = \frac{\partial}{\partial x_j}\left(\left(\mu + \frac{\mu_t}{\sigma_k}\right)\frac{\partial k}{\partial x_j}\right) + G_k + G_b - Y_M - \rho\varepsilon + S_k \qquad \text{Eq. 10}$$

$$\frac{\partial(\rho\varepsilon)}{\partial\mathrm{t}} + \frac{\partial(\rho\varepsilon U_j)}{\partial x_j} = \frac{\partial}{\partial x_j}\left(\left(\mu + \frac{\mu_t}{\sigma_\varepsilon}\right)\frac{\partial\varepsilon}{\partial x_j}\right) + \rho C_1 S_\varepsilon - \frac{\rho C_2\varepsilon^2}{k + \sqrt{\nu\varepsilon}} + C_{1\varepsilon}\frac{\varepsilon}{k}C_{3\varepsilon}G_b + S_\varepsilon \qquad \text{Eq. 11}$$

For a full definition of all the variables see [115]. These reformulations from the standard k-ε model removes weaknesses in cases with flow separation and stagnation. The realizable k-ε model has been proven to overcome these issues and has been validated for a wide range of flows [119].

2.2.2 - SAS turbulence models

For more detailed simulations, smaller eddies must be resolved during the flow, as opposed to averaging them out. The turbulence model used in the Venturi nozzle work to further resolve eddies was the Scale-Adaptive Simulation (SAS), as first proposed by Mentor and Egorov [120]. This model is based on Unsteady Reynolds Averaged Navier-Stokes (URANS) but employs the von Karman length-scale (Eq. 12) and resolves smaller scale eddies than traditional URANS:

$$L_{vK} = \kappa\left|\frac{U'}{U''}\right| \qquad \text{Eq. 12}$$

For a detailed definition see [115]. The transportation equations are given as:

$$\frac{\partial(\rho k)}{\partial t} + \frac{\partial(\rho k U_i)}{\partial x_i} = \frac{\partial}{\partial x_j}\left(\left(\mu + \frac{\mu_t}{\sigma_k}\right)\frac{\partial k}{\partial x_j}\right) + G_k - \rho k \omega c_\mu \qquad \text{Eq. 13}$$

$$\frac{\partial(\rho\omega)}{\partial t} + \frac{\partial(\rho\omega U_i)}{\partial x_i} = \frac{\partial}{\partial x_i}\left(\left(\mu + \frac{\mu_t}{\sigma_\omega}\right)\frac{\partial \omega}{\partial x_j}\right) + \frac{\alpha G_k \omega}{k} - \rho\beta\omega^2 + (1 - F_1)\frac{2\rho}{\sigma_{\omega,2}\omega}\frac{\partial k}{\partial x_j}\frac{\partial \omega}{\partial x_j} + Q_{SAS} \quad \text{Eq. 14}$$

The SAS turbulence model is classified as a scale resolving simulation (SRS) and so does not average the variables, but instead filters them. However, the filtering is not wholly based on the computational grid. In resolving more turbulent eddies, SAS provides a more detailed flow structure without necessarily requiring a greatly refined mesh and the large computational cost as compared to LES. This was extremely important for the Venturi nozzle as the simulation needed close to 10^6 time-steps, so the computational cost needed to be low to run the simulations in a reasonable amount of time. This was done with a coarser mesh than would be required by an LES turbulence model.

2.2.3- Advanced turbulence models

A detached eddy simulation (DES) turbulence model was used for the Control Orifice work. DES is a hybrid model, which institutes a URANS model near the wall for the boundary layer where it is unlikely that large eddies play a dominant role. In the core flow region, an LES model is utilized to further resolve the eddies in the transient flow [37]. As such, DES is less computationally expensive than a pure LES approach, while still providing highly detailed results, like a full LES model, in important regions. This was important for the Control Orifice work, as a high level of detail was needed in the orifice. Moreover, DES is more comparable to previous research of ERIs.

LES resolves large scale eddies and models the smaller eddies through sub-grid scale modelling. The eddy viscosity is applied to the sub-grid scale equation using the Smagorinsky model [121] [115]:

$$\tau_{ij} - \frac{\tau_{kk}\delta_{ij}}{3} = -2\mu_t\left(S_{ij} - \frac{S_{kk}\delta_{ij}}{3}\right) \qquad \text{Eq. 15}$$

where

$$\mu_t = \rho L_s^2 \sqrt{2\widehat{S_{ij}}\widehat{S_{ij}}} \qquad \text{Eq. 16}$$

and

$$\widehat{S_{ij}} = \frac{1}{2}\left(\frac{\partial \widehat{U_i}}{\partial x_j} + \frac{\partial \widehat{U_j}}{\partial x_i}\right) \qquad \text{Eq. 17}$$

Where L_s is the spatial limiter and is based on the distance from the wall and S_{ij} is the strain rate tensor. The eddy viscosity goes to zero at the wall. The full set of equations for LES are extensive and can be found in [115].

2.3 - Fluid properties

The fluid properties, or equations of state (EoS), were modelled with two in-house compressible models. The EoS used with the Venturi nozzle case was a barotropic single-fluid model representative of water and water vapour, where cavitation is only dependent on pressure. The EoS for the Control Orifice and thin gap in the Shoe and Guide assembly were representative of Normafluid and used the mixture model where cavitation occurs by employing a mass transfer rate. The two EoS were implemented with a user defined function (UDF).

2.3.1 - Water and water-vapour

The working fluid was modelled as water, water vapour and the mixture of the two. The EoS for each phase are implemented together as a barotropic single-fluid model. The three phases are compressible, which enables pressure wave propagation. These EoS have been used by previous researchers [11] [39] and shown to be robust. A Tait EoS was used in the liquid phase (Eq. 18), an isentropic EoS for the vapour phase (Eq. 20), and an EoS based on Wallis speed of sound [20] when both the liquid and vapour were present (Eq. 19). The complete set of equations is given as:

$$p(\rho) = B\left[\left(\frac{\rho}{\rho_l}\right)^{7.15} - 1\right] + p_{sat,l} \qquad if \quad \rho \geq \rho_l \qquad \text{Eq. 18}$$

$$p(\rho) = \frac{c_v^2 c_l^2 \rho_l \rho_v(\rho_v - \rho_l)}{c_v^2 \rho_v^2 - c_l^2 \rho_l^2}\ln\left(\frac{\rho}{c_l^2\rho_l(\rho_l - \rho) + c_v^2\rho_v(\rho - \rho_v)}\right) + p_{ref} \quad if \quad \rho_l > \rho \geq \rho_v \qquad \text{Eq. 19}$$

$$p(\rho) = C\rho^\gamma \qquad if \quad \rho_v > \rho \qquad \text{Eq. 20}$$

where B is a factor that relates to the bulk modulus (actual bulk modulus is $7.15B$), C is a constant, γ is the heat capacity ratio, and v and l indicate vapour and liquid, respectively. Reference values p_{sat} and p_{ref} are used to ensure the equations are continuous. In Table 2.1, values of the EoS variables are provided for 16.5°C, the average running temperature of the experiments. As a reference, the density and speed of sound are plotted against pressure (Fig. 2.1).

Table 2.1 – Reference properties used for the EoS

Liquid properties	Values	Units	Vapour properties	Values	Units
B	307.3×10^6	Pa	γ	1.33	-
ρ_l	998.8	kg/m^3	C	27715	N/A
c_l	1472	m/s	ρ_v	1.41×10^{-2}	kg/m^3
μ_l	1.1×10^{-3}	Pa·s	c_v	95.4	m/s
$p_{sat,l}$	3659	Pa	μ_v	9.94×10^{-6}	Pa·s
p_{ref}	4280	Pa	$p_{sat,v}$	96.5	Pa
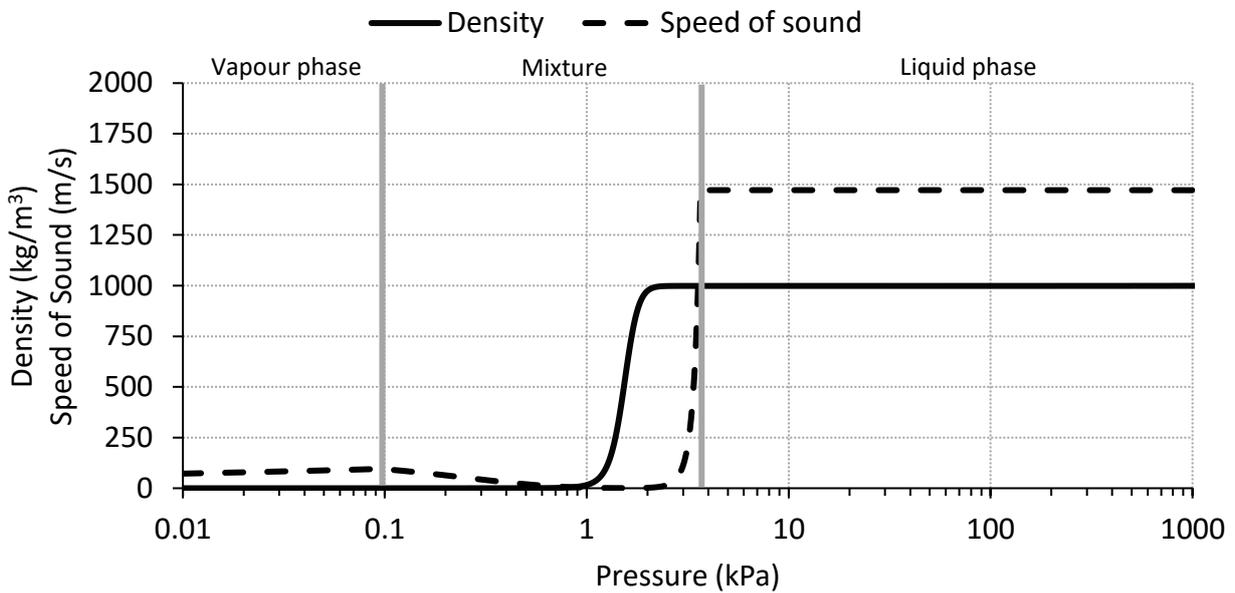
Fig. 2.1 - The density and speed of sound characteristics of the EoS plotted against pressure.

2.3.2 - ISO4113 (Normafluid) EoS

For the thin gap in the Shoe and Guide assembly and Control Orifice cases, an EoS representing liquid and vapor Normafluid were implemented alongside the ZGB cavitation model. Fig. 2.2 shows plots of Normafluid density, isentropic bulk modulus, speed of sound, and dynamic viscosity. The Normafluid EoS are given in [47] and [122] and have an average deviation less than 1% when compared to experimental data, which was measured up to 2000 bar. Data to compare the EoS at higher pressures was unavailable. However, the EoS is expected to be accurate up to 3000 bar. Moreover, the density appears reasonable at pressure up to 10,000 bar. It should be noted though that in the simulations, that pressures above 4000 bar were only reached a few times and so is not considered imperative. The vapour was considered as incompressible as any sizeable pressure change occurs while the fluid was in a liquid phase. However, this does limit examining the speed of

sound where vapour is present. The transition from liquid to vapour was done through the ZGB cavitation model.
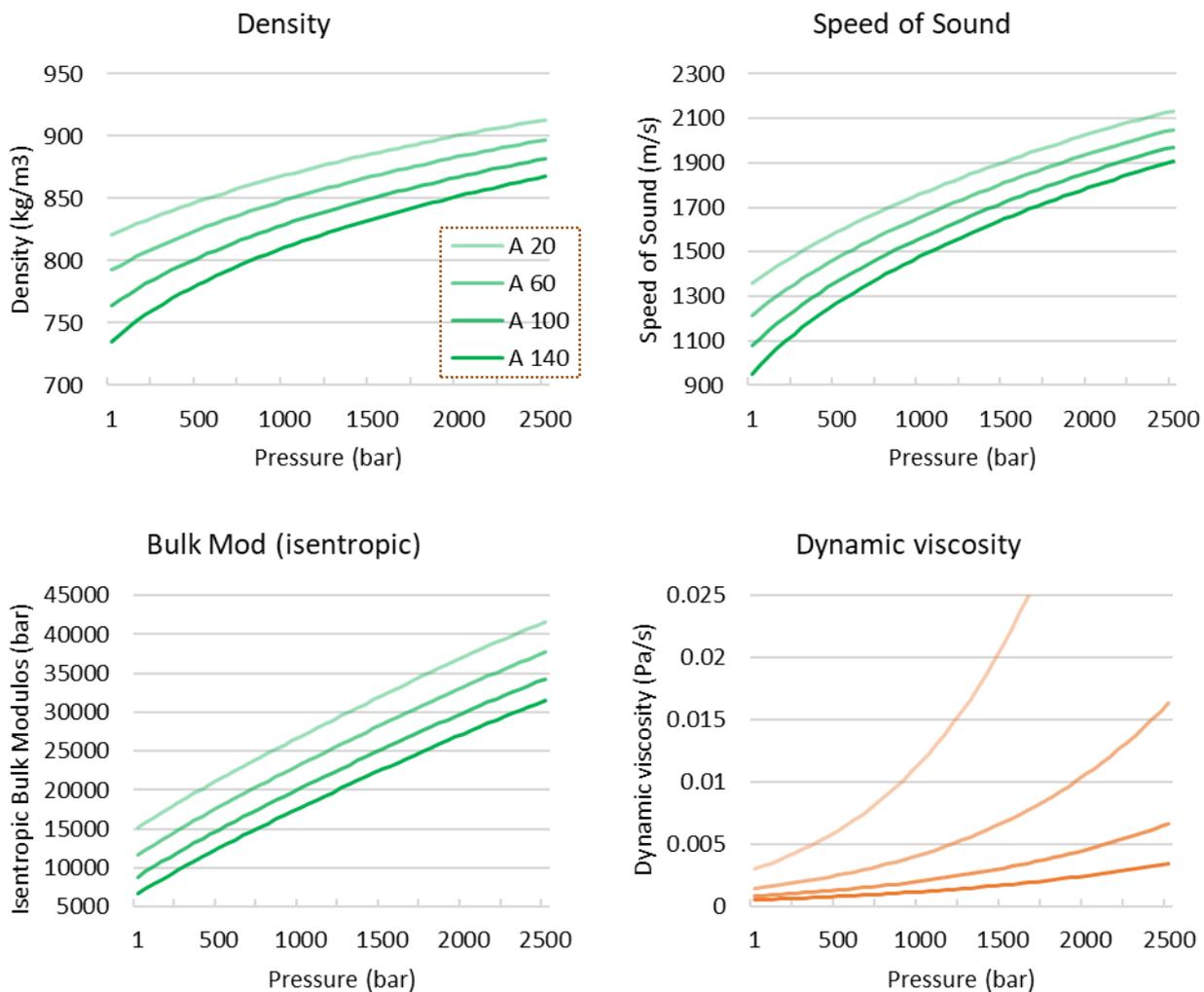
Fig. 2.2 – Fluid properties of Normafluid (A) at 4 different temperatures (20, 60, 100, and 140 °C)

2.4- Cavitation Model

The simulations using Normafluid (i.e. the Shoe and Guide assembly and Control Orifice components) used a homogeneous mixture model, as opposed to a single fluid model or an interface tracking model. The mixture model was deemed more appropriate as the cavitation was expected to be more of a cloud, or mixture, rather than discreet pockets of vapour.

The cavitation model used was based on the RP single bubble equation, given as:

$$\rho\left[\mathfrak{R}\ddot{\mathfrak{R}} + \frac{3}{2}\dot{\mathfrak{R}}^2\right] = p_v - p_\infty(t) + p_{g0}\left(\frac{\mathfrak{R}_0}{\mathfrak{R}}\right)^{3\gamma} - \frac{2S}{\mathfrak{R}} - 4\mu\frac{\dot{\mathfrak{R}}}{\mathfrak{R}} \qquad \text{Eq. 21}$$

where $\mathfrak{R}$ is the bubble radius, $\dot{\mathfrak{R}}$ its velocity, $\ddot{\mathfrak{R}}$ its acceleration and $\mathfrak{R}_0$ is the original bubble radius. The last two terms on the righthand side, representing surface tension and viscosity, are typically assumed negligible, along with the second order term. See section 1.2.2 for more information about the development of the RP equation.

Cavitation models within Fluent are implemented through the vapour transport equation, defined as:

$$\frac{\partial(\alpha_v\rho_v)}{\partial t} + \nabla \cdot (\alpha_v\rho_v\boldsymbol{U}_v) = R_e - R_c \qquad \text{Eq. 22}$$

where ρ is density, α_v is vapour volume fraction, $\boldsymbol{U}$ is velocity field, v denotes vapour and R_e and R_c are the rates of evaporating and condensing mass transfer, respectively. Coupled with this are the mass and momentum conservation equations (Eq. 1 and Eq. 2), which are solved using the mixture density:

$$\rho = \alpha_v\rho_v + \alpha_l\rho_l \qquad \text{Eq. 23}$$

For the ZGB cavitation model, R is related to the bubble number density (n) and the rate of change, which is assumed to be the same for all the bubbles.

$$R = n(\rho_v 4\pi\mathfrak{R}^2)\frac{D\mathfrak{R}}{Dt} \qquad \text{Eq. 24}$$

where:

$$\frac{D\mathfrak{R}}{Dt} = \sqrt{\frac{2(p_v - p)}{3\rho_l}} \qquad \text{Eq. 25}$$

and:

$$\alpha_v = n\left(\frac{4}{3}\pi\mathfrak{R}^3\right) \qquad \text{Eq. 26}$$

R takes the following form depending on condensing (R_c) or evaporating (R_e), as described by Zwart et al [25]:

$$R_e = F_e\frac{3a_{nuc}\alpha_l\rho_v}{\mathfrak{R}}\sqrt{\frac{2(p_v - p)}{3\rho_l}} \qquad \text{Eq. 27}$$

$$R_c = F_c\frac{3a_v\rho_v}{\mathfrak{R}}\sqrt{\frac{2(p - p_v)}{3\rho_l}} \qquad \text{Eq. 28}$$

where α_{nuc} is nucleation site volume faction, p is pressure, and F_e and F_c are constants. Note that the $\alpha_{nuc}\alpha_l$ accounts for the reduction of nucleation site density within the liquid as more vapour is produced. In Fluent, the default values for the ZGB model constants are 1e-6 m for $\mathfrak{R}$, 5e-4 for α_{nuc}, 0.01 for F_c, and 50 for F_e (as suggested in [25]). These values were used for the thin gap case, but for the Control Orifice the mass transfer rate was increased as the simulations produced unrealistic negative pressure (tension in the liquid).

2.5 - Increased mass transfer rate (*R*)

The constants in the ZGB equations greatly affect the rate of mass transfer. The constants can be grouped as:

$$F_{evap} = F_e \frac{3\alpha_{nuc}}{\mathfrak{R}}$$
<div align="right">Eq. 29</div>

$$F_{cond} = F_c \frac{3}{\mathfrak{R}}$$
<div align="right">Eq. 30</div>

resulting in F_{evap} equalling 75,000 m^{-1} and F_{cond} equalling 30,000 m^{-1} with the default values.

The ZGB cavitation model approaches a barotropic model asymptotically as the mass transfer rates tend toward infinity. Koukouvinis et al [40] demonstrated improved results for eliminating unrealistic negative pressure by using this increased *R*. They also demonstrated good results for their ERIs. As such, a modified ZGB cavitation method was implemented for the Control Orifice case. A large but practical value of 10^8 for both F_{evap} and F_{cond} was used.

2.6 - Erosion Risk Indicators (ERIs)

ERIs were applied to the thin gap (Shoe and Guide) and Control Orifice cases. Many factors have been suggested as ERIs in the literature. Some relate to the energy or power produced by a violently collapsing vapour region, while others relate to physical forces exerted. The published ERIs reviewed and tested in the current work are from Franc & Michel [6], Fortes-Patellar et al [71], Koukouvinis et al [34] [123]. These ERIs, along with several novel ERIs, were explored.

An energy approach was considered by Franc & Michel [6]. Their equation quantifies the acoustic power (P_a), defined as:

$$P_a = \frac{\rho_l V_{cell}^2}{4\pi c_l}\left(\frac{\partial^2 \alpha_v}{\partial t^2}\right)^2$$
<div align="right">Eq. 31</div>

when expressed in terms of cell volume and vapour volume fraction. Here, c_l is the speed of sound in the liquid.

An alternate energy approach, first postulated by Hammitt [124] and expanded on by Fortes-Patellar et al [71] [72]. The latter work presented a means of measuring cavitation aggressiveness by considering the potential power density (P_{p1}/V_{cell} or *PPD1*), defined as:

$$\frac{P_{p1}}{V_{cell}} = (p_v - p)\frac{D\alpha_v}{Dt} + \alpha_v \frac{Dp}{Dt}$$

Eq. 32

where V_{cell} is the cell volume. This comes from the derivative of potential energy of a collapsing bubble. The authors went on to assume the $\alpha_v Dp/Dt$ term was negligible. Using a different form of Eq. 1, i.e. the local mass equation ($D\rho/Dt + \rho \boldsymbol{\nabla} \cdot (\boldsymbol{U})$), Eq. 32 can then be rearranged to get a second form of potential power density (*PPD2*), defined as:

$$\frac{P_{p2}}{V_{cell}} = (p_v - p)\frac{\rho}{\rho_l - \rho_v}\boldsymbol{\nabla} \cdot (\boldsymbol{U})$$

Eq. 33

Pressure (i.e. static pressure taken at the cell centre) and its material derivative have been explored by Koukouvinis et al [40] [123]. This was also included in this study, along with several other variables and various derivatives. The material derivative is given as:

$$\frac{D\varphi}{Dt} = \frac{\partial \varphi}{\partial t} + \boldsymbol{U} \cdot \boldsymbol{\nabla}\varphi$$

Eq. 34

where φ is the variable of choice. Clearly, the material derivative includes terms related to time and the fluid motion. However, while the spacial term ($\boldsymbol{U} \cdot \boldsymbol{\nabla}\varphi$) is present, it is expected to be minimal near the wall due to the no-slip condition. This is explored by examining the different components of the material derivative.

Finally, an easily obtainable and simple ERI sometimes considered is R_c (Eq. 28) and has a strong influence on the derivatives of density and vapour fraction.

A list of ERIs tested on which components are given in the respective chapters. The thin gap data was collected earlier and so fewer ERIs had been proposed by then. However, as a reference, Table 2.2 is provided which lists all of the various ERIs and why they were examined. Some of the variables tested appear in other equations, but the main goal was simply to explore the importance of certain physics. All the variables are related to each other in some way, but it is expected some would be more numerically stable and sensitive as ERIs than others. Reasons for these differences may include the model type (pressure or density based), cavitation model (single fluid or mixture) or turbulence model.

Table 2.2 – Complete list of ERIs examined and why they were selected

Variable	Variable name	Reason for testing
p	Pressure (static pressure)	Previously tested
Dp/Dt	Material derivative of pressure	Previously tested
D^2p/Dt^2	Second material derivative of pressure	Further explore the importance of pressure
dp/dt	Partial derivative of pressure	Previously tested
$-Dp/Dt$	Negative values of the total derivative of pressure	Further explore the importance of pressure
$(Dp/Dt)/V_{cell}$	Material derivative of pressure divided by the cell volume	Test the importance of cell size
$(Dp/Dt)^2$	Material derivative of pressure, squared	Further explore the importance of pressure
$D\rho/Dt$	Material derivative of density	Explore the importance of density
$d\rho/dt$	Partial derivative of density	Explore the importance of density
R_c	Condensing R	Previously tested
$D\alpha_l/Dt$	Material derivative of liquid volume fraction	Previously tested
$d\alpha_l/dt$	Partial derivative of liquid volume fraction	Previously tested
$d^2\alpha_l/dt^2$	Second partial derivative of liquid volume fraction	Further explore the importance of vapour fraction
p_d	Dynamic pressure	Further explore the importance of pressure
Dp_d/Dt	Material derivative of dynamic pressure	Further explore the importance of pressure
$\nabla \cdot (\boldsymbol{U})$	Divergence of velocity	Explore the importance of velocity
$D\boldsymbol{U}/Dt$	Acceleration	Explore the importance of velocity
$PPD2$	Second derivation of potential power density	Previously tested
P_a	Acoustic pressure	Previously tested

3 - Vapour shedding characteristics in a Venturi nozzle

3.1 – Introduction

Hydrodynamic cavitation develops in regions of flow fields subjected to pressures lower than the working fluid vapor pressure. It can occur in a wide range of systems, such as those involving hydrofoils, in turbo machinery, as well as in orifices present in rocket and automotive fuel injectors [7]. The cavities may exist as large voids or as clouds of bubbles and can be attached to a wall or travel in the mainstream flow [43]. Attached cavities can exhibit an unsteady trailing edge that oscillates or sheds vapor, which is carried downstream in the flow. These vapor formations and oscillations can result in negative effects on the system, like vibration, noise, loss of lift and power, and erosion [6]. When designing new systems, potential cavitation shedding must be understood so the system can be designed to cope with or avoid instabilities, and so function as needed. This is especially true for systems where cavitation is unavoidable, such as in high pressure fuel injectors [125] or ships propellers [126].

There are two general mechanisms that lead to vapour shedding and occur under different flow conditions. They are the re-entrant jet and condensation shock (see section 1.2.7 for descriptions and an in-depth literature review concerning the mechanisms). In this chapter, the two shedding mechanisms are investigated on a Venturi nozzle that was investigated experimentally by Hogendoorn [91] and Jahangir et al [92]. These researchers were able to characterize, using high-speed video at different flow conditions, a re-entrant jet shedding regime, a bubbly shock shedding regime and a transition zone between them. They found that the re-entrant jet shedding mechanism had a much higher shedding frequency than the bubbly shock shedding mechanism. Jahangir et al [93] went on to collect averaged X-ray CT data of the Venturi nozzle at two running conditions corresponding to the two shedding mechanisms. With this, the authors explored the internal cavitation structures and the average vapour distribution. Currently, there is no CFD work that demonstrates the correct re-entrant jet shedding mechanism seen in the experiments and only limited results of the bubbly shock shedding mechanism.

The novelty in the work presented here exists firstly in the analysis revealing a more coherent trend in the quantitative results for the experiments over a wide range of running conditions. The quantitative CFD results match this trend. Facilitated by the in-depth analysis of the quantitative results, the CFD simulations achieve both the re-entrant jet and the condensation shock vapor shedding mechanisms, as seen in the experiments. Previous CFD investigations have had difficulty realizing the re-entrant jet case on this geometry [94] [127]. In

addition, the current work clarifies the shedding mechanisms for internal three-dimensional geometries of circular cross-section, instead of simplified, often two-dimensional geometries, such as the frequently used wedge [57] [87] [128] [129] [130]. Further to that and for the first time on this geometry, average vapor fraction slices of the CFD are compared with those from the experimental computed tomography (CT) and show good agreement overall. Finally, details have been exposed which cannot be extracted from the experiments and provide additional insight into the shedding mechanisms.

For the preceding work, results are presented of the CFD investigation that was carried out on a Venturi nozzle, which has been studied experimentally. The simulation methodology is presented in section 3.2, while section 3.3 analyses the CFD results and discusses how they compared to the experimental data. Finally, the summary and conclusion are given in section 3.4.

3.2 - Brief overview of the simulation model and methodology

The fluid properties were modelled with an in-house compressible model. The EoS used were a barotropic single-fluid model representative of water and water vapour, implemented with a UDF. The different phases are compressible which enables pressure wave propagation. This is important as a potential vapour shedding mechanism is caused by pressure waves. See section 2.3.1 for further details of the EoS.

Throughout the different flow conditions and across the different diameters, the Re ranged from 7×10^4 to 2.5×10^5, which indicates that the flow is inertia dominated overall, rather than viscous dominated. As such, Cointe [94] used an inviscid model to simulate the Venturi nozzle flow, as did Budich et al [57] for simulations of flow over a wedge. Nevertheless, flow separation and low velocities are present in the diverging section of the nozzle. So, as the viscosity could affect the shedding behaviour, the Scale-Adaptive Simulation (SAS) turbulence model was selected for the current work, as described in [115] and [120]. This model is based on Unsteady Reynolds Averaged Navier-Stokes (URANS) but employs the von Karman length-scale and resolves smaller scale eddies than traditional URANS. The SAS turbulence model is classified as a scale resolving simulation (SRS) and so does not average the variables, but instead filters them. However, the filtering is not wholly based on the computational grid. In resolving more turbulent eddies, SAS provides a more detailed flow structure without necessarily requiring a greatly refined mesh and the large computational cost as compared to LES. See section 2.2.2 for further details of the turbulence model.

The Venturi (Fig. 3.1, left) is 17cm in length with a throat diameter of 1.66cm. The upstream and downstream pipes have a diameter of 5cm. The mesh (Fig. 3.1, right) consisted of 8.2×10^5 cells with a cell axial length of 0.8mm near the Venturi throat. Coupled with a timestep of 1μs, the Courant–Friedrichs–Lewy condition (CFL) is less than 0.02 when considering the flow velocity at the throat. As pressure waves are a central feature of
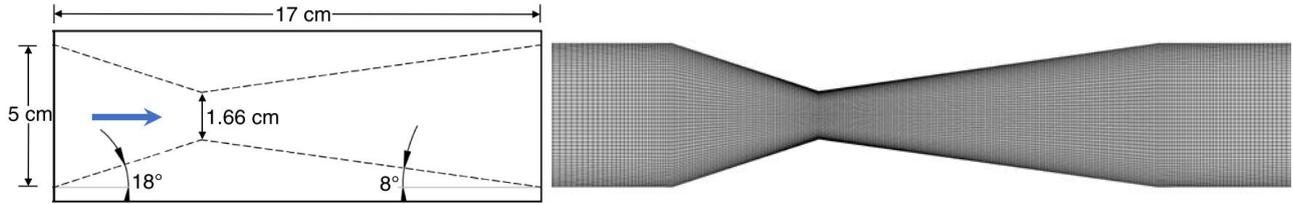
Fig. 3.1 – Left: Schematic of the Venturi geometry. Jahangir et al [92], Right: Mid-plane view of the mesh at the Venturi.

shedding, the acoustic CFL was also considered and equates to 1.75 in pure water. However, in mixture regions the speed of sound drops greatly [6] [20] and so the acoustic CFL in these regions is well below unity, in which case any pressure waves would be captured.

As a reference, the Taylor length scale is estimated to be 100µm and the Kolmogorov time scale is about 2µs. Hence the mesh could be further refined, but a well-structured tetrahedral mesh would need almost 20 million cells to achieve that level of refinement. In order to avoid the heavy computational cost associated with this, the SAS model was allowed to revert back to URANS in the boundary layer. As such, the Y+ in the Venturi nozzle was usually below 30. However, the mesh is considerably finer than that implemented in other studies of this geometry [94] [127]. Coarser meshes were tested and resulted in similar flow characteristics and shedding, but worse Y+, so the finest mesh was used. Mesh suitability was confirmed when checks showed the simulated pressure drop vs flow rate matched the experiments (section 3.3.1).

The domain included an inlet volume followed by a porous medium boundary at the start of the inlet pipe (as suggested in [131] [132]). The values used for the porous medium boundary were 10^{10}m^2 for the permeability, 23m^{-1} for the pressure-lump coefficient and 1m for the thickness. The porous medium boundary works in a similar way to snubber valves, used in high pressure fuel lines to reduce potentially harmful pressure reflections. The dimensions for the porous medium were selected from experience with snubber valves [133]. The upstream pressure was recorded downstream of the inlet volume, so that any pressure drop created by the porous medium did not impact the pressure readings. The simulations used a velocity boundary condition at the inlet and a fixed pressure at the outlet.

3.2.1 - Analysis of data

To compare the experimental and CFD results, the following nondimensional numbers were used. Relating to the shedding frequency, the Strouhal number (St_d) is defined as:

$$St_d = \frac{fD}{\bar{u}}$$

Eq. 35

where f is the shedding frequency, D is the characteristic length taken as the throat diameter and $\bar{u}$ is the average velocity at the throat.

Cavitation numbers of different definitions have long been used to indicate the level of vapor present in the flow. Jahangir et al [92] considered St_d with respect to a cavitation number (σ), given as:

$$\sigma = \frac{p_d - p_v}{\frac{1}{2}\rho\bar{u}^2}$$

Eq. 36

where p_d is the downstream pressure, p_v is the vapor pressure and ρ is the reference liquid density. The downstream pressure was measured at 400mm from the throat in the CFD and 730mm in the experiments, a difference not considered significant as both locations are sufficiently far downstream and viscous losses were low, in the region of 0.2% of the overall pressure drop.

The loss factor (K) was also considered with respect to the cavitation number:

$$K = \frac{\Delta p}{\frac{1}{2}\rho\bar{u}^2}$$

Eq. 37

where Δp is the difference between the upstream and downstream pressures. The upstream pressure was measured at 200mm from the throat in the CFD and 310mm in the experiments. Again, a difference not considered significant. Normally K is considered for minor losses and is calculated with the average downstream velocity [134] [135], but here the average throat velocity was used to maintain consistency with relevant previous papers [92] [93].

An alternative cavitation number, from the work of Bergwerk [136], was introduced to the analysis for the current work:

$$CN = \frac{\Delta p}{p_d - p_v}$$

Eq. 38

This cavitation number is more consistently used for internal flows within industry (see for example [33] [109] [134] [137]) and takes into account the pressure drop caused by the feature of interest, which is not considered in σ. Moreover, the usual definition of σ [7] states that the velocity and pressure are taken at U_∞ and p_∞, respectively, which correspond to locations unaffected by the feature of interest, as is appropriate for external flows.

3.3 - Results and discussion

3.3.1 - Quantitative results

The base experimental information comes from Hogendoorn [91] and Jahangir et al [92], who collected data for many running conditions for this Venturi nozzle. The quantitative experimental results were originally examined with respect to the cavitation number σ [92]. For the current work those results, along with the new CFD results, were also considered with respect to the cavitation number CN.

Fig. 3.2 shows the distribution of St_d with respect to both cavitation numbers. The regions of the two different shedding regimes, as determined by the experimental and CFD images (see sections 3.3.2 and 3.3.3), are indicated. As previously mentioned, cavitation numbers are used to indicate the level of vapour present in the flow: vapour levels increase as σ decreases or as CN increases. Hence, when there is less vapour, as indicated in Fig. 3.2 by higher values of σ or lower values of CN, the shedding mechanism is predominantly re-entrant jet and sheds at a higher frequency. When there is more vapour (indicated by lower σ values or higher CN values), the dominant shedding mechanism is condensation shock and is characterized by a lower shedding frequency. When St_d is plotted against CN (right plot in Fig. 3.2) the experimental results are much more cohesive and the same is true for the CFD results. Moreover, the two sets of results show good agreement with each other. This clearer result is consistent with CN being the cavitation number more appropriate for the internal, three-dimensional geometry tested in this work as it accounts for the pressure drop across the region of interest. It is also apparent from Fig. 3.2 that the re-entrant jet shedding mechanism is only possible over a very narrow range of running conditions. This indicates why it has been difficult in past studies [94] [127] to simulate the re-entrant jet shedding mechanism.

In Fig. 3.3, the loss factor (K) is plotted against σ and CN. Again, both the experimental and the CFD results are more cohesive when analysed with respect to CN. It also shows that there is slightly more pressure loss in the CFD simulations. This is in line with other studies (see [57] [94] [127]), Fig. 3.3 also shows that for this set of
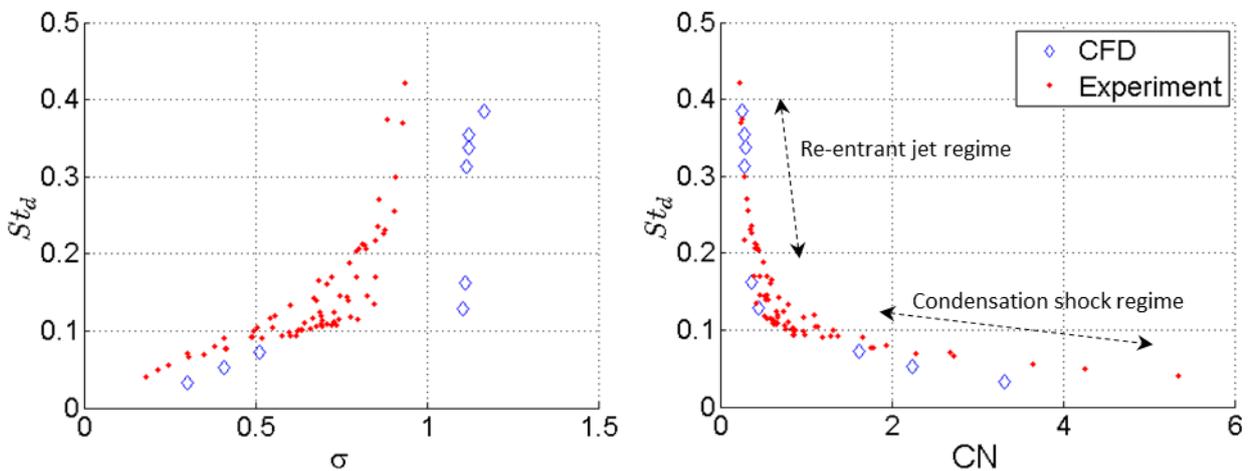
Fig. 3.2 – Strouhal number (St_d) versus different cavitation numbers. Left: σ. Right: CN.
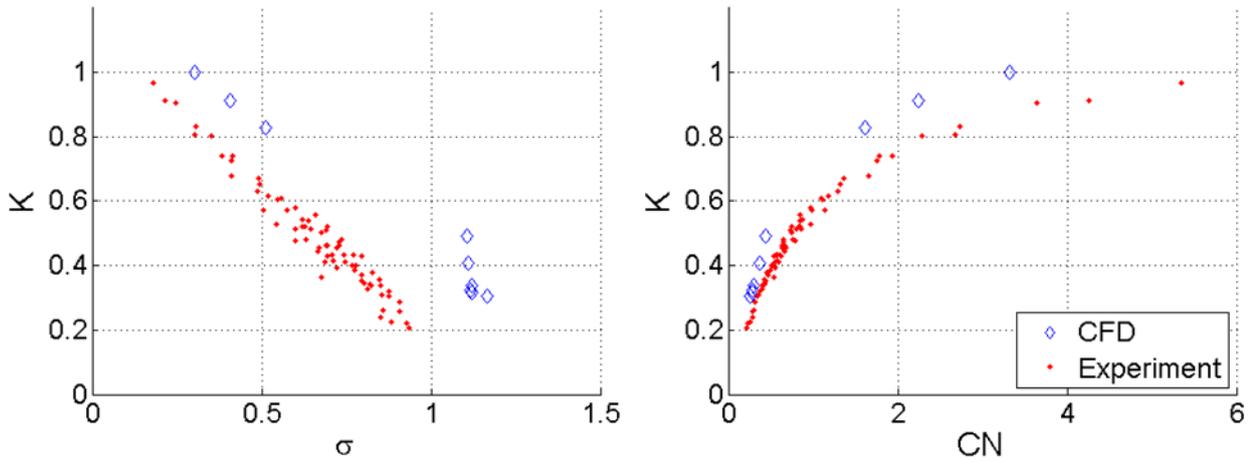
Fig. 3.3 – Loss factor (*K*) versus different cavitation numbers. Left: *σ*, Right: *CN*.

running conditions the magnitude of *K* is mainly influenced by the quantity of vapour, as indicated by the cavitation numbers, and not by the shedding mechanism.

Simulation results at two running conditions (Table 3.1) were used to make detailed comparisons with the corresponding experimental results. The CFD results in the following section show that both the re-entrant jet and condensation shock shedding mechanisms were achieved. Moreover, they were achieved with pressure drops that matched the experiments for the flow rates used. This is considered the important factor, even though a higher downstream pressure was used in the CFD to guide the amount of cavitation produced. Regarding the shedding frequency, that of the condensation shock shedding mechanism agreed well with the experiments. The frequency of the re-entrant jet shedding mechanism showed some discrepancy. This is strongly linked to the trend shown in Fig. 3.2: the St_d increases by 100% for a 0.2 change in *CN,* or 0.1 change in *σ,* indicating an extreme sensitivity of the shedding frequency to the level of cavitation. Hence, the discrepancy in the re-entrant jet shedding frequency is likely explained by this sensitivity, along with cycle to cycle variations and the uncertainties in both the experimental and CFD results.

Table 3.1 - Running conditions and results for the shedding mechanism investigation.

		Flow rate (l/s)	Δp (kPa)	p_{out} (kPa)	f (Hz)	St_d	K	CN	σ
Re-entrant jet	Experiment	2.95	28	80	192	0.24	0.31	0.36	0.86
	CFD	2.94	28	101	250	0.31	0.32	0.29	1.1
Condensation shock	Experiment	2.99	85	26	46	0.056	0.90	3.6	0.25
	CFD	2.99	86	40	43	0.053	0.91	2.2	0.41

3.3.2 - Re-entrant jet vapour shedding mechanism

In Fig. 3.4, frames of high-speed videos from experiments by Hogendoorn [91] and Jahangir et al [92] are compared with analogous CFD results for re-entrant jet shedding. The first two columns show that vapor structures simulated closely match those of the experiment. The third column shows the axial velocity on the mid-plane, which further illustrates the detail of the vapor shedding and confirms that the re-entrant jet shedding mechanism is well captured by the CFD results.

At the start of each cycle, the vapor forms as a toroid at the wall of the Venturi, immediately downstream of the throat (t_0 + 2ms). With time, this cavitating annular region extends downstream, and a re-entrant jet forms
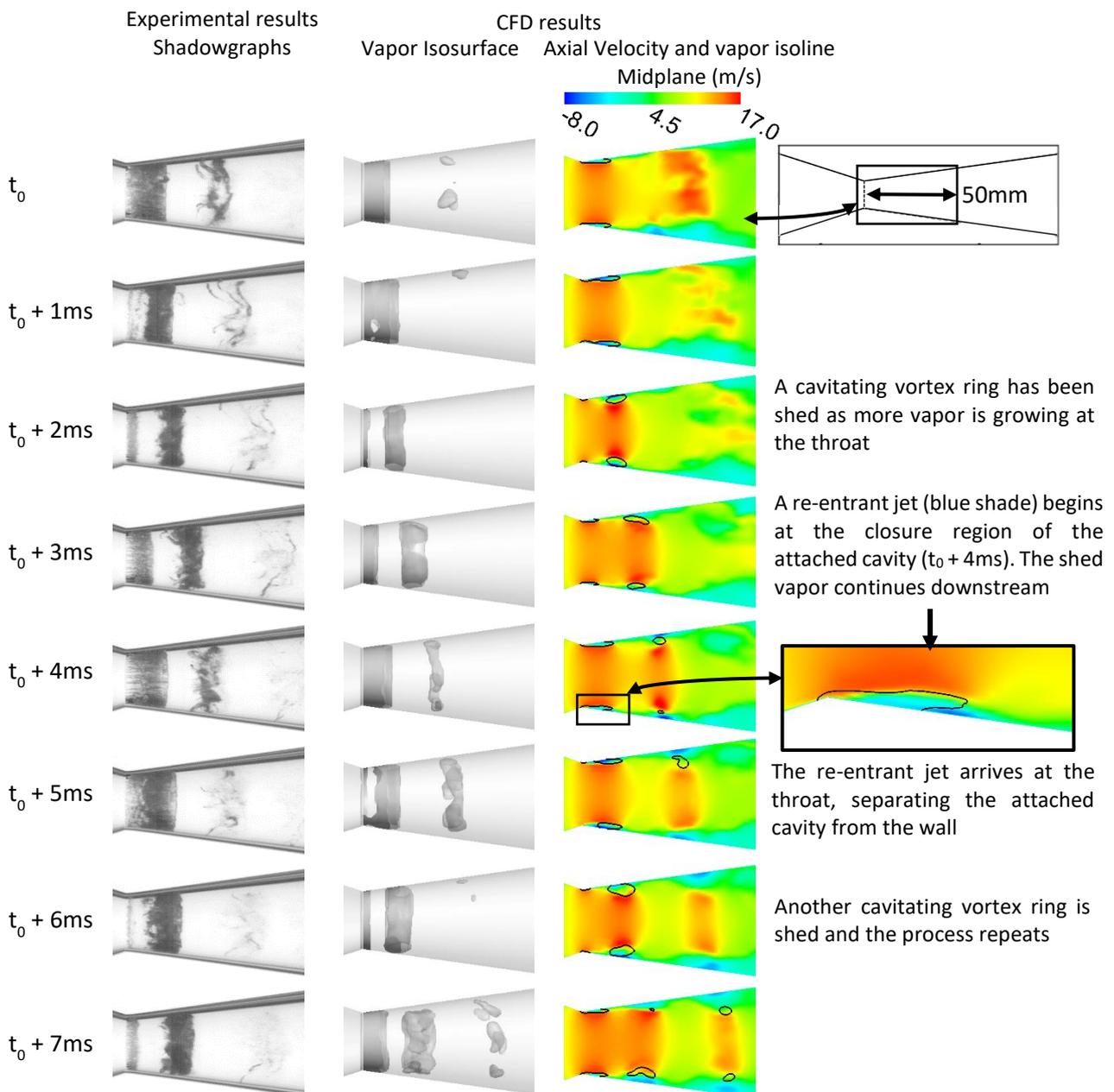
Fig. 3.4 – Re-entrant jet vapor shedding cycle. Left: experimental high-speed shadowgraphy. Center: CFD Isosurface vapor volume fraction at 10%. Right: color - axial velocity; black isoline - vapor volume fraction at 10% on the mid-plane. (See Table 3.1 for running conditions)

at the closure region (t$_0$ + 4ms, blue shade in column 3) detaching the cavitation at the wall. Separation in the boundary layer and the attendant re-entrant flow are caused by the local adverse pressure gradient stemming from the cavitating region, and the expanding geometry downstream of the Venturi throat. As this re-entrant jet reaches the throat, the vapor detaches completely and is shed downstream as a cavitating vortex ring (t$_0$ + 6ms) and the process repeats. Some cycle to cycle variation can be seen in Fig. 3.4 of both the experimental and simulation results. This instability is likely connected with the sensitivity to the running conditions.

3.3.3 - Condensation shock vapour shedding mechanism

The first and second columns in Fig. 3.5 compare frames of a high-speed video from experiments by Hogendoorn [91] and Jahangir et al [92] with analogous CFD images for condensation shock shedding. They demonstrate good agreement in timing and in the distribution of the vapor between the experimental and CFD results. The third column in Fig. 3.5 shows the axial velocity on the mid-plane, which highlights the back flow that develops during the shedding process. The images show that the cavitation grows from the throat (t$_0$ + 2ms to t$_0$ + 10ms) and extends considerably further than in the re-entrant jet case.

By frame t$_0$ + 12ms, the downstream cloud of previously shed vapor has collapsed. This creates a pressure wave that propagates upstream, back to the trailing edge of the attached vapor and triggers the condensation front, which coincides with the appearance of a backflow along the wall (column 3, Fig. 3.5). The condensation front progressively detaches the vapor at the wall until it reaches the throat, when the whole vapor structure is shed and convected downstream as a cloud.

A close study of the experimental and CFD vapor images reveals that there is a small difference in the cavitation structure close to the throat: in the experiment, the cavitation initiates as streaks [7]. This streak cavitation (Fig. 3.6) only occurs over a very short distance and is associated with imperfections in the surface finish of the component [7] [138]. The geometry in the CFD is perfectly smooth and does not produce this streak cavitation structure.

The shedding process is further illustrated in Fig. 3.7, which shows the liquid volume fraction, condensing $d\rho/dt$ and evaporating $d\rho/dt$. As noted in Fig. 3.5, the first column confirms that the vapor forms in a toroid just downstream from the throat, but later extends across the entire diameter. Moreover, the progress of the condensation front as it travels back towards the throat is revealed by the high values of condensing $d\rho/dt$ (second column) at the trailing edge of the attached cavity (highlighted at t$_0$ + 15ms). As expected, this tracks the negative velocity in the recirculating flow at the walls, as shown in Fig. 3.5. Some further condensation and evaporation can be seen within the main body of cavitation. Although higher values of $d\rho/dt$ can be

Experimental results
Shadowgraphs

CFD results
Vapor Isosurface Axial Velocity and vapor isoline
Midplane (m/s)

-8.0   4.5   17.0

t_0 — Vapor from the previous cycle has been shed

$t_0 + 2ms$ — A new vapor toroid begins to grow from the throat

$t_0 + 4ms$

$t_0 + 6ms$

$t_0 + 8ms$

$t_0 + 10ms$

$t_0 + 12ms$ — Vapor extends over the entire cross-section

$t_0 + 14ms$ — The condensation wave and negative axial velocity initiate the vapor detaching at the wall

$t_0 + 16ms$

$t_0 + 18ms$ — Collapse of vapor and negative axial velocity progress back towards the throat

$t_0 + 20ms$

$t_0 + 22ms$ — Once more, the vapor is shed as a cloud and the cycle repeats itself

Fig. 3.5 – Condensation shock vapor shedding cycle. Left: experimental high-speed shadowgraphy, dark grey indicating vapor. Center: CFD Isosurface vapor volume fraction at 10%. Right: color - axial velocity on the mid-plane; black isoline - vapor volume fraction at 10%. (See Table 3.1 for running conditions) Note that in the experiment there is a slightly distorted view in the section after the Venturi. This is due to the exterior shape in the downstream section and not a step in the internal geometry.

caused by vapor rapidly traveling across cells rather than collapsing or expanding, this is not the case here. Fig. 3.5 shows there are only low velocities in regions of high $d\rho/dt$.

The vapor images indicate that the vapor grows from the throat in an annular

Streak cavitation
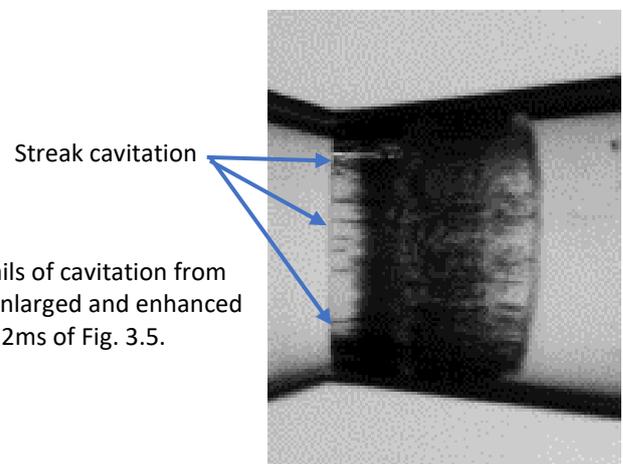
Fig. 3.6 – Details of cavitation from experiment: enlarged and enhanced section at $t_0 + 2ms$ of Fig. 3.5.
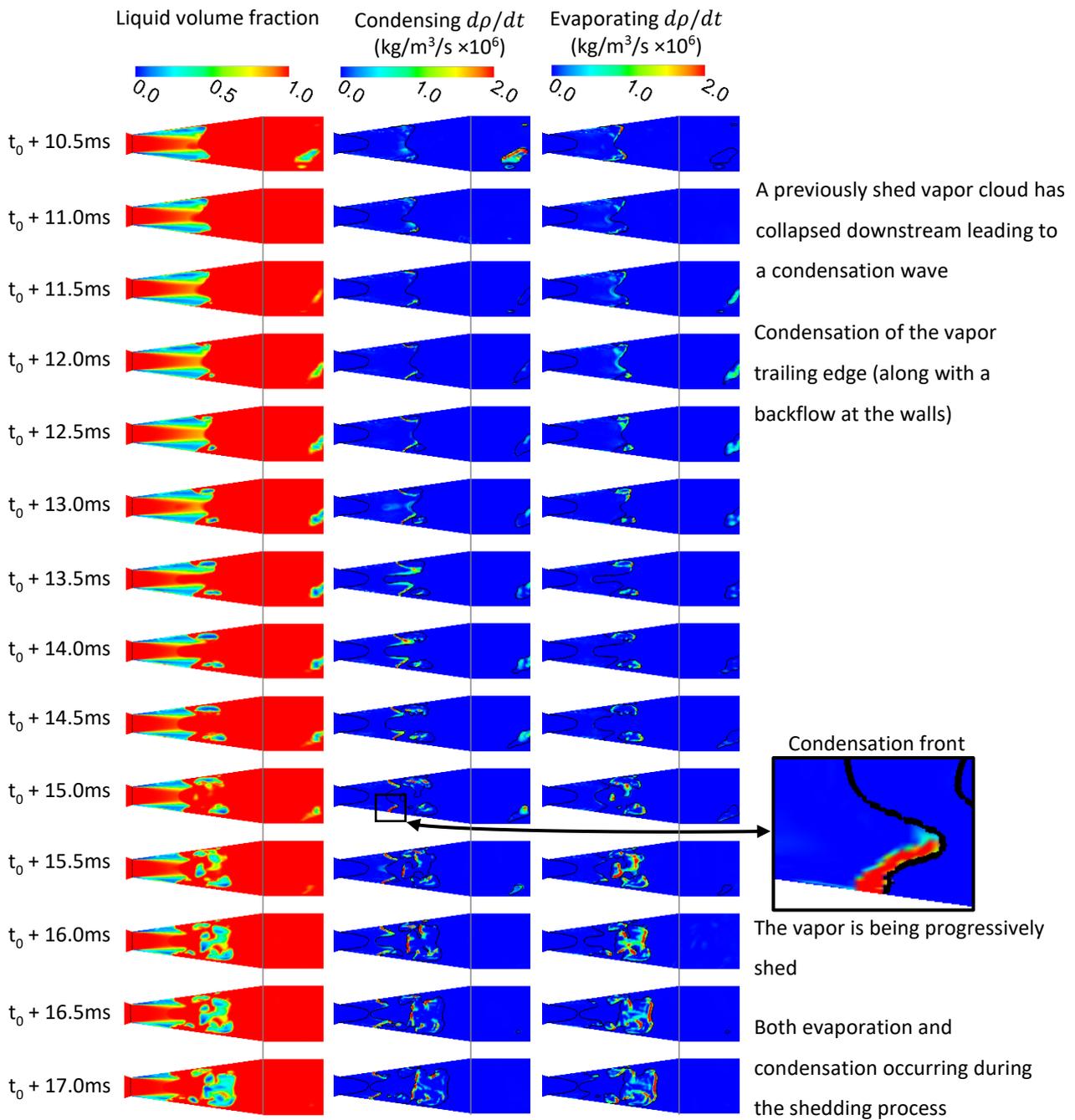
Fig. 3.7 – Part cycle of condensation shock vapor shedding as the condensation wave travels up the attached cavity. CFD mid-plane values. Left: vapor volume fraction. Middle: condensing $d\rho/dt$. Right: evaporating $d\rho/dt$. Isoline - vapor volume fraction at 1%. (See Table 3.1 for running conditions)

region close to the walls, but later extends over the entire cross section of the Venturi. It is well known that cavitation in the flow can create the condition in which the acoustic speed in the two-phase mixture falls well below that for each of the single phases [20], enabling supersonic flow. The Rankine-Hugoniot jump condition, originally derived for one-dimensional flow, can be used to identify if the condensation wave does indeed represent a shock front and also computes its velocity [57] [139] [140]. The Rankine-Hugoniot condition is given as:

$$\begin{bmatrix} \rho u \\ \rho u^2 + p \end{bmatrix}_{pre,post} = s \cdot \begin{bmatrix} \rho \\ \rho u \end{bmatrix}_{pre,post} \qquad \text{Eq. 39}$$

where s is the wave propagation velocity and u is the axial velocity component. The subscripts pre and post denote pre- and post-shock and $[\cdot]_{pre,post} = (\cdot)_{pre} - (\cdot)_{post}$. The density, axial velocity and pressure values in Table 3.2 are taken at pre- and post-shock locations at $t_0 + 13.5ms$ (Fig. 3.8). The values do indeed satisfy the Rankine-Hugoniot jump condition with a shock propagation speed of 4.2m/s, which agrees with the rate of 4.25m/s calculated from the frames in Fig. 3.9.

Table 3.2 – Pre- and post-shock conditions for the Rankine-Hugoniot analysis.

	Density (kg/m³)	Velocity (m/s)	Pressure (Pa)
Pre-shock	158.5	3.84	1,311
Post-shock	998.8	-2.91	10,070
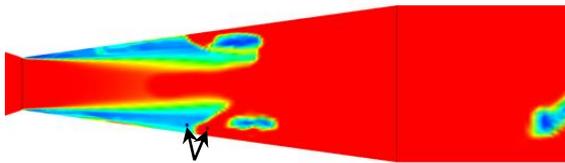
Points where values were taken

Fig. 3.8 – Above: Locations where values were taken to test the Rankine-Hugoniot jump condition at $t_0 + 13.5ms$.

Fig. 3.9 – Right: Details from Fig. 3.6 of cavitation from CFD results used to calculate the average shock propagation speed for this time range.
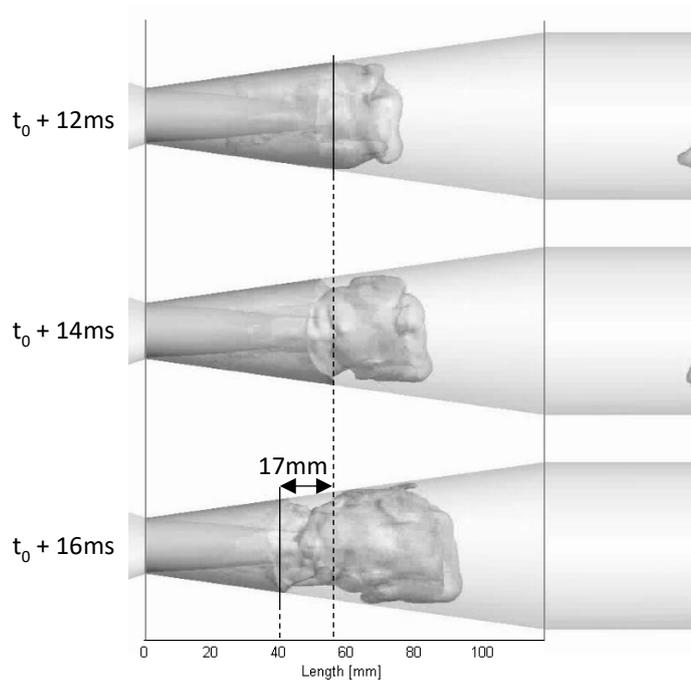
Jahangir et al [92] produced a space-time (x-t) plot from the experimental data. A similar process was repeated with corresponding CFD data using total vapor fraction. Fig. 3.10 shows the x-t plots constructed from the experimental and CFD results. The cavity lengths (red arrows) agree well, and the condensation and shedding processes occur in a similar manner. Both x-t plots show that shed vapor collapses downstream (green lines). This triggers the condensation wave (yellow curved lines) that travels up the attached vapor to begin a new shedding process.
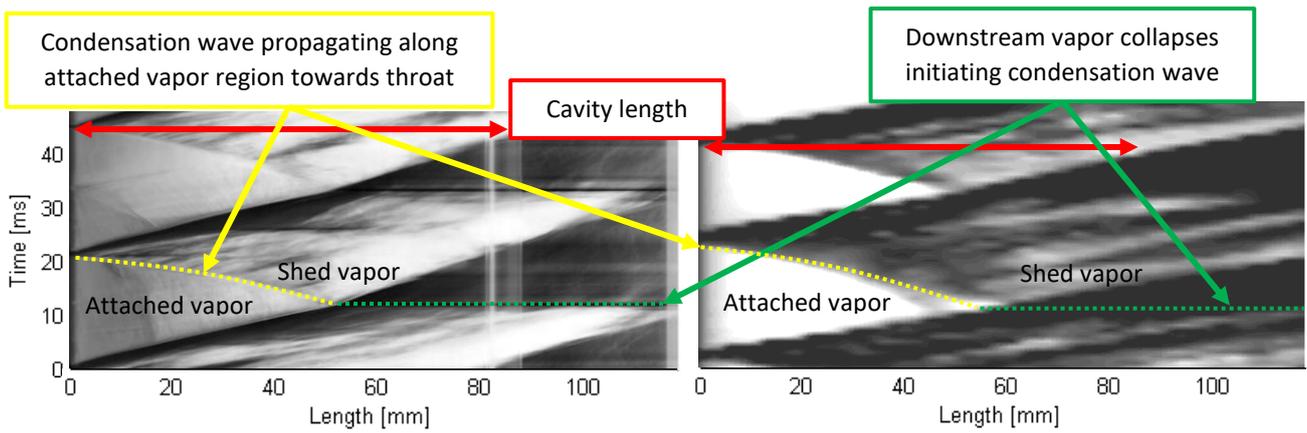
Fig. 3.10 – Condensation shock vapor shedding: x-t plot of experimental results (left) and CFD results (right). Colors are inverted from previous figures (light gray indicates vapor). Grayscale levels are approximate and do not indicate precise level of vapor. (See Table 3.1 for running conditions) Experimental image reprinted from [92] with permission from Elsevier
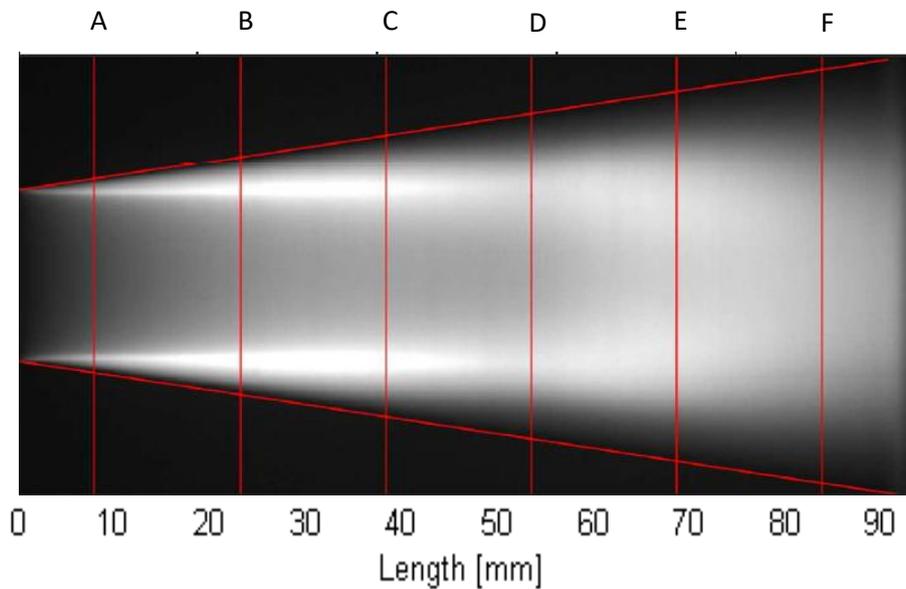
Fig. 3.11 – Experimental time-averaged X-ray results in the condensation shock regime. Letters indicate where the CT slices were taken. The length covers 93mm. Experimental image reprinted from [93] with permission from Elsevier.

Finally, 2D experimental time-averaged X-ray images of the cavitating Venturi nozzle were reconstructed using CT to produce a pseudo 3D numerical representation of the averaged vapor content [93]. The X-ray images were taken over 60 seconds (2700 shedding cycles) and captured the projected average of cavitation in the Venturi nozzle (Fig. 3.11), with the light grey representing vapor. This X-ray data was then reconstructed using CT to show the average vapor distribution at different planes (further examples of CT reconstruction can be found in [141] [142]).

41
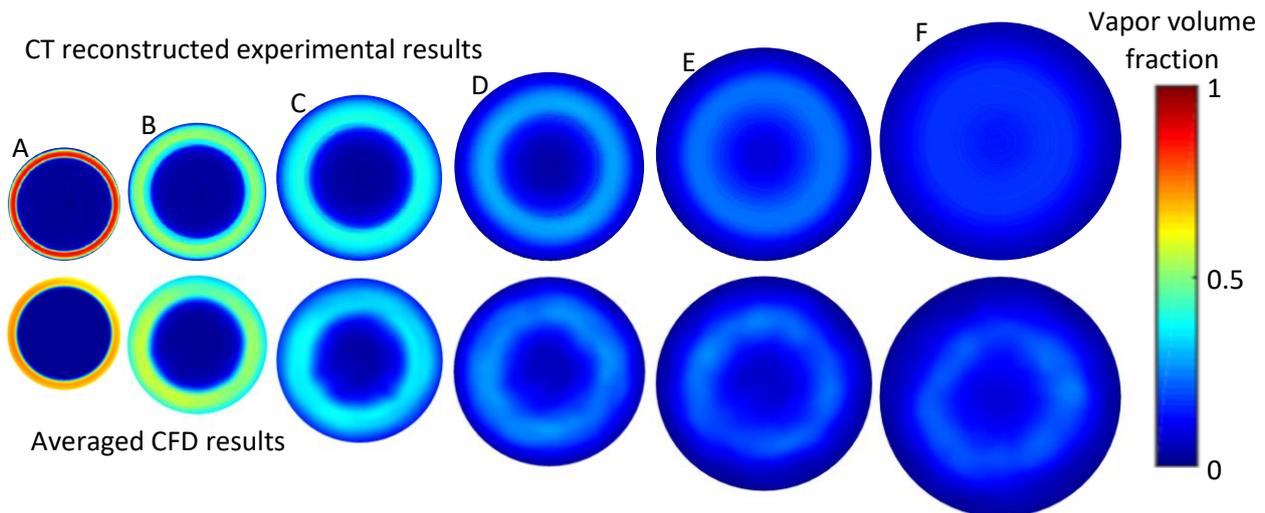
Fig. 3.12 – Condensation shock mechanism: comparison of the average vapor fraction from experimental (top, [93]) and CFD results (bottom). (See Table 3.1 for running conditions) Experimental image reprinted from [93] with permission from Elsevier.

In order to compare with the averaged CT slices, the CFD results for the vapor volume fraction were averaged over 22 shedding cycles (0.5 seconds). Fig. 3.12 presents experimental CT results compared with CFD images and shows very good agreement overall.

There is a minor difference in locations A and B, near the throat of the Venturi, where the experimental CT slices show a layer of liquid against the wall, and a higher concentration of vapor adjacent to that. The averaged CFD results show a lower concentration of vapor and it is distributed up to the wall, with no outer ring of liquid. As the CFD predicts a larger distribution of vapor, the overall volume of vapor is consistent with the experiment. These differences at locations A and B are most likely connected to streak cavitation, as discussed earlier (Fig. 3.6). In the experiment, streak cavitation occurs for a very short distance downstream of the throat, which is not reproduced in the perfectly smooth geometry of the CFD. So, in the experiment, the cavitation is intermittent around the throat circumference. These streaks are also likely to be unsteady (some evidence of this in the frames in Fig. 3.5). Moreover, measurement errors with CT reconstruction will be more significant in the tube periphery, as the X-ray line of sight only passes through a very small volume of mixture. These factors are likely why the CT processing has interpreted total liquid next to the wall.

3.4 - Conclusion

The vapor shedding mechanisms of cavitating flows in an axisymmetric Venturi nozzle were investigated with CFD simulations and compared with relevant experiments. Analysis of the quantitative results with regards to the Strouhal number and loss factor revealed coherent trends and showed the good overall agreement between the experiments and CFD over a wide range of running conditions. Moreover, it was concluded that

the *CN* cavitation number was the more appropriate parameter for use with internal, three-dimensional geometries involving a pressure drop. Two running conditions were studied in detail: one in the re-entrant jet regime and the other in the condensation shock regime. The detailed CFD results confirmed that re-entrant jet and condensation shock were the dominant vapor shedding mechanisms.

Analysis of the full data set over the range of running conditions provided insight into the conditions under which the different vapor shedding mechanisms occurred and demonstrated the extreme sensitivity of the re-entrant jet mechanism, which only occurs over a very narrow range of the running conditions. This signified that a small change in settings would produce a large change in the shedding frequency for this mechanism, which is likely why previous research has had difficulty to reliably simulate it.

For both shedding mechanisms, the details and development of the simulated vapor structures during a shedding cycle closely matched those of the experiments and the measured pressure drop was achieved as well. Moreover, the CFD results provided detail of the flow mechanisms that cannot be extracted from the experiments. Finally, a comparison of average vapor fraction was conducted using CT slices from the experiments and demonstrated overall good agreement with the averaged CFD results. From this, the understanding of cavitation and shedding mechanisms, which can affect flow stability, spray break-up and erosion in orifices, has been expanded.

4 - Cavitation erosion risk indicators for a thin gap within a diesel fuel pump

4.1 – Introduction

Cavitation is common in many fields like naval, automotive and aviation, and often leads to problems such as reduced efficiency, noise and erosion. Consequently, there has been extensive research dedicated to understanding and controlling the effects of cavitation, through experiments and CFD simulations. Nevertheless, erosion caused by cavitation is still an ongoing field of research due to the complexity of the physics in the micro and macro scales of cavitation collapse and of the interaction with the boundary material. This, along with the further complexity that simply having cavitation collapse near a solid wall will not always result in erosion, are some of the reasons why there is no consistently accurate model to predict cavitation erosion. See section 1.2.6.3 for an in-depth discussion about ERIs and section 1.2.8 for a literature review concerning cavitation and cavitation erosion within thin gaps.

The work detailed in this chapter involves a component within a high-pressure fuel pump [143]. It was noted by the Delphi Technologies Pump Team, following endurance tests, that some slight cavitation erosion occurred on the shoe and shoe-guide, which are located under the pumping plunger. The work investigates erosion of the boundaries of this narrow fluid filled gap and the application of potential ERIs.

The details of this assembly and the endurance test findings are given in section 4.2, while section 4.3 explains the dynamics of the shoe within its guide during normal operation. Although the erosion after endurance testing was too slight to result in a problem over the life of the pump, alternative designs were investigated in the interest of robustness for future applications with increased requirements. Some of the designs were successful in avoiding cavitation erosion and showed no signs of damage after testing.

To understand this erosion, a CFD investigation was undertaken on the fluid filled gap between the Shoe and Guide. Section 4.4 describes how both the original design and an alternative design, which avoided erosion, were modelled. Section 4.4.1 defines the ERIs examined which were used to assess the potential risk of surface erosion. The CFD simulations are examined with respect to the cavitation characteristics within the dynamic gap between the Shoe and Guide faces. These results are discussed in section 4.5. In section 4.5.1 the analysis of the results of each potential ERI are presented, comparing the distribution of their maxima to images of the damaged components. Finally, the summary and conclusion are given in section 4.6.
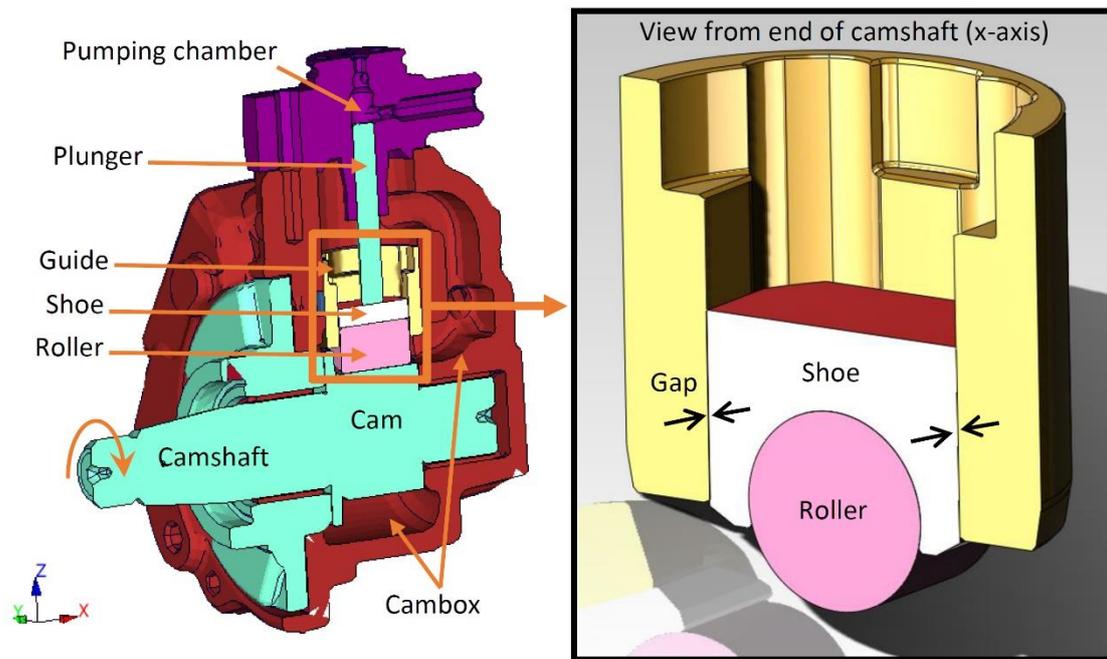
Fig. 4.1 - Cutaway diagram of the fuel pump and the location of the shoe and shoe-guide within.

4.2 - Experimental procedure and results

Fig. 4.1 shows a cutaway of the high-pressure fuel pump and the location of the narrow gap between the sliding faces of the shoe and the guide. The pump pressurizes fuel up to 2000 bar and delivers it to the common rail system [144]. Newly designed or modified components undergo extensive testing before they can proceed to serial production. This testing includes endurance runs, which assess the robustness of the component when exposed to long periods of continuous running at demanding operational conditions. One such endurance test runs the fuel pump at 5000 RPM for a certain period of time that is orders of magnitude longer than the time spent at any running condition in normal use. After this test it was found that the guide face experienced varying patterns of non-critical cavitation erosion. Fig. 4.2-B shows the typical pattern of damage found on the face of the guide, while Fig. 4.2-C shows a specific pattern seen on one sample. Fig 2-C also shows clearly the simple, flat-face geometry of the original design. As mentioned before, the erosion was too slight to result in a problem over the life of the pump, alternative designs were still investigated in the interest of robustness for future applications. One such proposed design had a large vertical groove on the face of the guide (Fig. 4.2-D). Subsequent endurance tests with this modified design produced no erosion on the faces of the shoe and its guide. The guide is made of steel with surface hardening by sintering in accordance with ISO 5755 FD-05N2C-950H.

A: location of the sliding face of the guide in the high-pressure fuel pump

B: Original design guide face: Typical erosion pattern

4mm

2mm

C: Original design guide face: A specific erosion pattern

D: Modified design guide face: Non-eroding

3mm

6mm
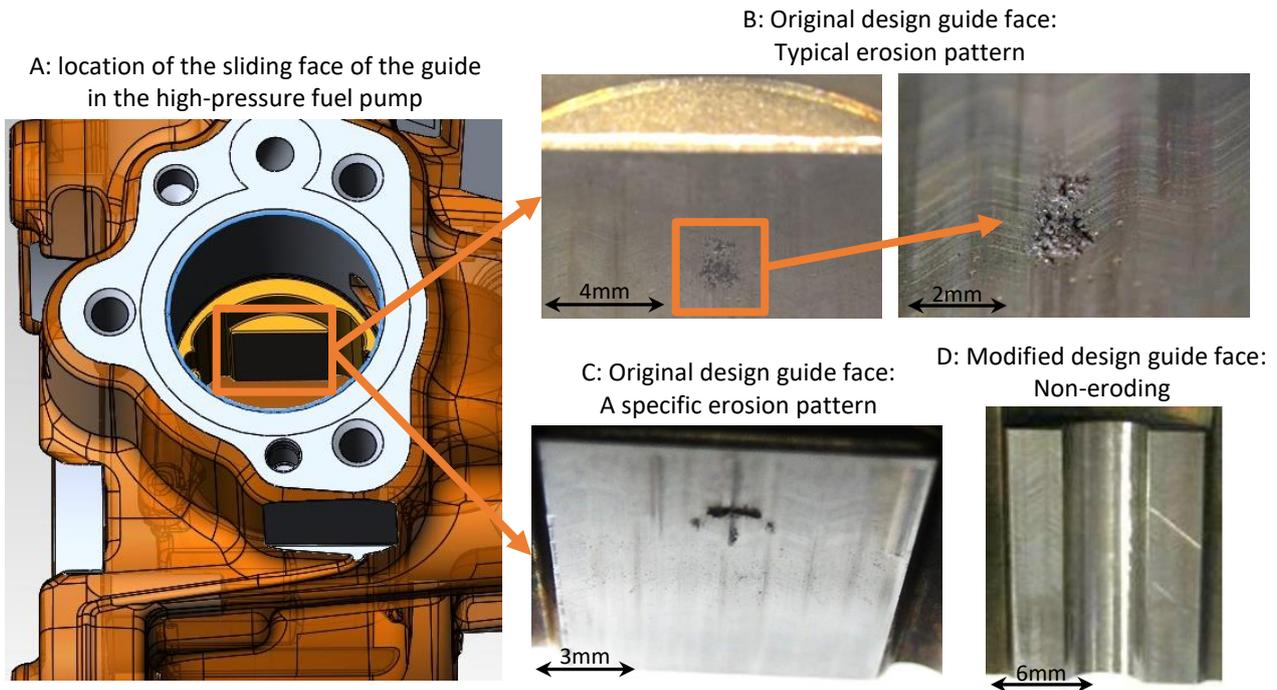
Fig. 4.2 – Examples of the non-critical cavitation erosion, or lack thereof, on the two designs

4.3 - Geometry and dynamics of the shoe and shoe-guide assembly

As the camshaft rotates during the pumping stroke, the cam displaces the roller, shoe and plunger, which pressurises the fuel in the pumping chamber (Fig. 4.3-A). After the top of the stroke, the cam profile and the return spring allow the plunger assembly to retract to its original position, enabling the pumping chamber to refill for the next stroke (Fig. 4.3-C). With this type of pump design, there is a small, yet interesting, lateral movement of the shoe within the guide. The lateral movement is caused by the direction of the force transmitted to the shoe from the rotating cam, via the roller. This lateral thrust causes the shoe to travel at a slight angle within the guide during both the pumping and filling periods. When the plunger reaches the top of its stroke, the direction of the thrust from the cam changes, which causes the shoe to change its tilt angle and move across the small clearance within the guide (Fig. 4.3-B). The gap between the shoe and its guide is fluid filled and is fed by the cambox on all sides. When the shoe moves away from its guide, due to the lateral force, albeit by only tens of microns, the fluid pressure will be reduced. If the flow from the cambox is then unable to fill the increasing volume in the gap at the appropriate rate, cavitation will be generated. It was expected that this possible cavitation creation and its subsequent collapse is what led to the erosion seen on the hardware after endurance tests.
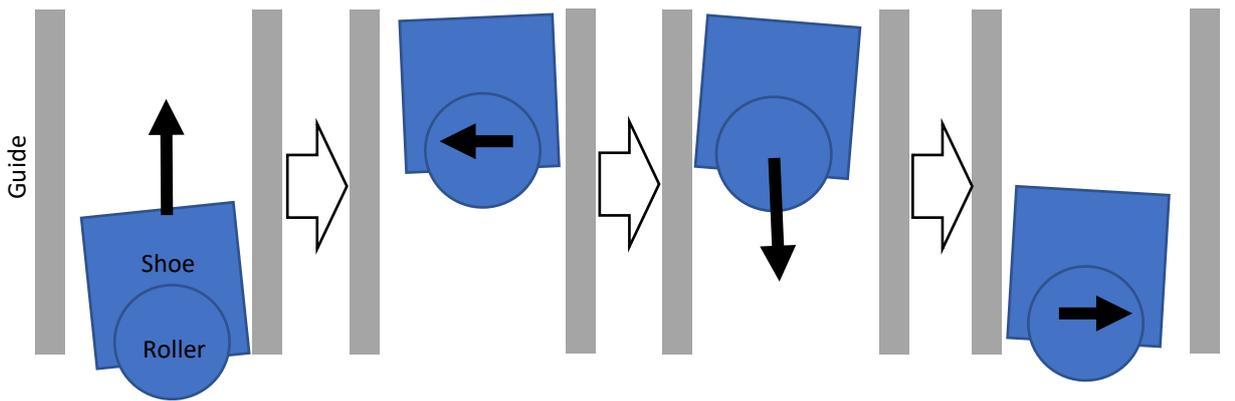
A – Pumping stroke: the shoe is pushed upward due to the rotation of the cam. This moves the plunger which compresses the fuel. The thrust from the cam causes the shoe to tilt.

B – Top of stroke: the shoe is forced laterally across the guide clearance due to the change in direction of the thrust from the cam. This also changes the shoe tilt.

C – Filling stroke: the cam profile and return spring allow the plunger assembly to retract to its original position, enabling the pumping chamber to refill for the next stroke.

D – Bottom of stroke: the shoe returns to begin the pumping cycle again.

Fig. 4.3 - Schematic indicating the shoe motion within its guide during a pumping cycle.
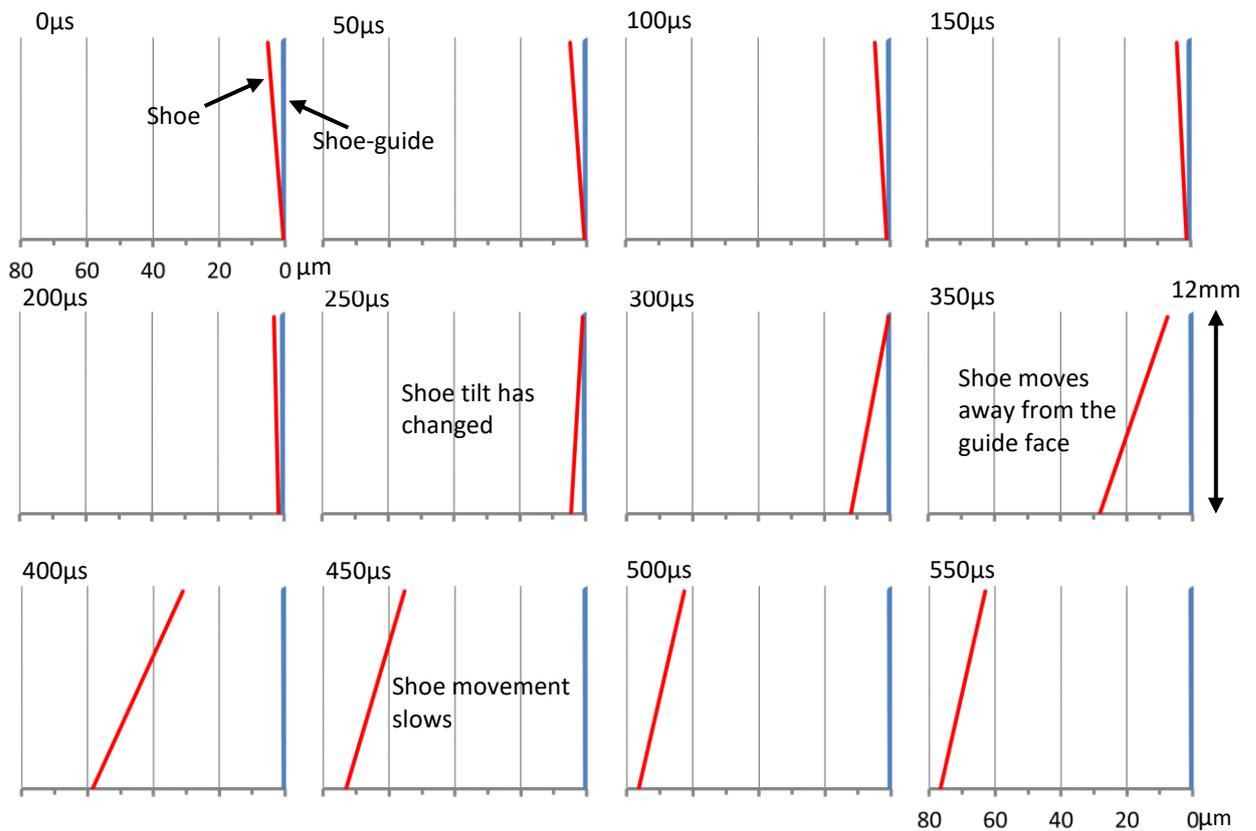
Fig. 4.4 - 2D visualization of the change in shoe orientation at the top of the pumping stroke.
(Note the x-axis scale is in µm while the y-axis scale is in mm.)

An elastohydrodynamic simulation of some of the high-pressure pump components was previously commissioned by Delphi Technologies [145]. As part of that study, the linear and rotational components for the shoe movement were calculated. Although both sides of the shoe are affected by this lateral motion (Fig. 4.3-B and D), it is the side that is in closest contact during the pumping stroke which is of more interest (Fig. 4.3-B). Further detailed visualization of the shoe face movement is given in Fig. 4.4. The shoe movement shown in Fig. 4.4 occurs close to top of the pumping stroke and corresponds to Fig. 4.3-B. The gap clearance ranged from 0.4μm to 79μm.

4.4 - Brief overview of simulation model and methodology

All simulations were done with ANSYS Fluent V17 (see the chapter 2 and [115] for details). The standard ZGB cavitation model was used. When the simulations were run, unrealistic negative pressures did not occur. This indicates it was unnecessary to calibrate the cavitation parameters further [125], therefore the default values of $\Re_B$, α_{nuc}, F_e and F_c were used [115].

The geometry of interest in the original design was a hexahedron, created by the two flat faces of the shoe and its guide and the narrow, uneven gap between them. The faces were approximately 12mm square and the fluid filled gap was fed by the cambox pressure on all other sides. Considering the narrow gap range of 0.4μm to 79μm and the flow rates under investigation, the flow regime was expected to be largely laminar, which calculations confirmed. This can affect the structure of cavitation formed [43].

As with the actual components, the guide face remained stationary for the simulation, while the shoe face moved to vary both the gap width and the tilt, with respect to the guide. The modified design had the same shoe face and the same motion profile but had a semi-circular vertical groove in the guide face with a chamfer included in the groove to gap transition region. A deforming mesh was implemented to accommodate the shoe movement. The simulations begin near the top of the pumping stroke (Fig. 4.3-B) and run over a period of 880μs.

Fig. 4.5 shows the mesh within the groove and the narrow gaps. The detail shown in the enlarged section for the narrow gap was used in both designs. The gap was divided into 20 cells to ensure resolution as per basic CFD requirements. Cell aspect ratio was of course a concern, but care was taken to impose a well-structured deforming mesh as the gap expanded and the flowrate increased. The aspect ratio at the start of the simulation was around 2000 but dropped to 17 as the gap expanded.

A mesh study was carried out on the original design. It was seen that a symmetrical boundary down the centre gave results which were almost identical to those of simulations with the full domain. Different levels of mesh refinement were considered, from 68×10^3 to 3.6×10^6 cells. These changes had almost no effect on flowrate
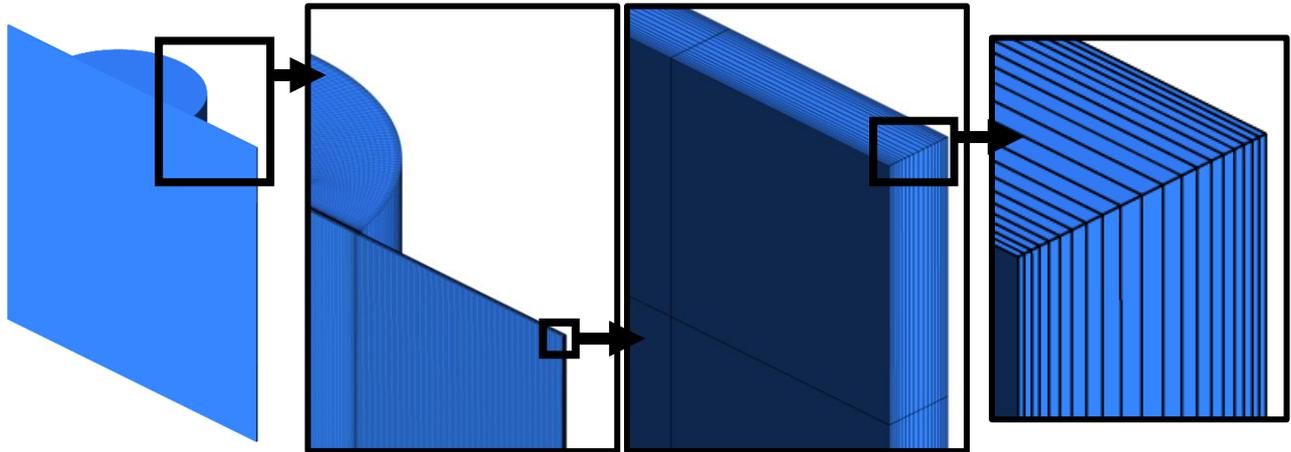
Fig. 4.5 - Mesh of the groove in the guide face and of the narrow gap between the faces of the shoe and the guide.

and so the coarsest mesh could be considered to provide a mesh independent result. However, while flowrate may be an adequate variable to determine mesh independence for many simulations, it may not be an acceptable criterion for some of the ERIs being investigated. As such, for the final simulations, the finest mesh was selected. Hence, the original design had approximately 3.6×10^6 cells and the modified design had about 5.7×10^6 cells.

The pressure boundary condition of four bar was applied to the four sides and matched the averaged values measured in the cambox during regular operation. The fluid properties were modelled as Normafluid (ISO4113), the standard test fluid in the diesel industry and what was used in the endurance tests. These were based on [47] and [122] and were also previously used by Bush et al [32] in experimentally validated CFD simulations. Reference values at 4 bar and 100°C are given in Table 4.1. Given the high pressures expected during cavitation collapse, liquid compressibility was included. See section 2.3.2 for further details about the EoS used.

Table 4.1 – Fluid properties at 4 bar and 100°C.

Property	Liquid (*l*)	Vapour (*v*)
Density (kg/m^3)	764	6
Bulk modulus (bar)	8896	
Speed of sound (m/s)	1079	
Dynamic viscosity (kg/m/s)	8.5e-4	4e-6

4.4.1 - Erosion risk indicators

A total of 10 potential ERIs were investigated, shown in Table 4.2. Details of the potential ERIs are discussed in-depth in section 2.6. The potential ERIs were assessed by examining the magnitude and distribution of maximum values reached during the simulation periods and comparing the results to images of erosion. While the magnitude of these indicators may still be affected by the mesh or time-step (see Appendix C for a cursory study), the difference in the relative values between the two designs should still be preserved. The overall objective is a high level of differentiation between the two designs in the relative magnitude of the ERIs, with strong correlation of maxima locations with erosion as seen on the hardware.

Table 4.2 – List of ERI investigated on the Shoe and Guide.

Variable	Variable name	Variable	Variable name
p	Pressure (static pressure)	R_c	Condensing R
Dp/Dt	Total derivative of pressure	$D\rho/Dt$	Total derivative of density
D^2p/Dt^2	Second total derivative of pressure	$D\alpha_l/Dt$	Total derivative of liquid volume fraction
$(Dp/Dt)^2$	Total derivative of pressure squared	$PPD2$	Second derivation of potential power density
Dp_d/Dt	Total derivative of dynamic pressure	P_a	Acoustic pressure

4.5 - Results and discussion

The results for the original design are given in Fig. 4.6. The time evolution of pressure, velocity, liquid volume fraction and condensing R are shown. These results are provided on the mid-plane in the gap. The first frame in Fig. 4.6, at 187µs, shows the initial effects of the lateral shoe movement. As the shoe changes its angle, pressure builds at the top as that region is compressed. Near the bottom, cavitation is being produced as the fuel flowing into the ultra-narrow gap cannot keep up with the expanding volume. Although this initial lateral movement has these noticeable effects, it is too small to be discernible in Fig. 4.4. At 307µs, the shoe is pulling away from the guide at such a rate that the entire gap has cavitated. By 487µs, the movement of the shoe slows and the fuel flows in from the cambox at the boundaries to collapses the vapour. On the next frame, 547µs, all the vapour has collapsed. The pressure caused by the inward force from this initial collapse rebounds outward, resulting in the creation of a second vapour region followed by its collapse. The initial vapour collapse and rebound are shown in detail in Fig. 4.7, where the distinct shape of the collapsing cavity is clear.

The velocity images on the later frames in Fig. 4.6 and Fig. 4.7 show a skewed cross region. This is where the flows from the four sides meet, which gives rise to the four fingers of liquid growing into the vapour region during the collapse (Fig. 4.7). This characteristic also produced a cross-shape in some of the ERIs, shown later.

Pressure
(bar)

Velocity
Magnitude
(m/s)

Liquid
Volume
Fraction

R
(kg/m^3/s ×10^6)

0   10   20   0   10   20   0.0   0.5   1.0   -1.0   -0.5   0.0

187µs — Early in the simulation the gap near the top is compressed while near the bottom it expands. Hence, the top is pressurized and the bottom cavitates

247µs — Significant flow out of the upper region

307µs — The shoe is now pulling away from the guide causing cavitation to form throughout the narrow gap

367µs — Fuel flows into the narrow gap from all sides and reduces the size of the vapour region

427µs

487µs — As the shoe slows down, the vapour region is rapidly collapsing

547µs — The vapour has now completely collapsed. The vapour implosion causes a significant increase in pressure

607µs — The subsequent pressure collapse causes a rebound of cavitation

667µs — The velocity shows a skewed cross shape. This is from the interaction of flow entering from the four sides

727µs — Collapse of the secondary vapour region

Fig. 4.6 – Original design: full cycle sequence of cavitation creation, collapse and rebound.

51

	Pressure (bar)	Velocity Magnitude (m/s)	Liquid Volume Fraction	R (kg/m³/s ×10⁶)

Liquid fingers are growing at the corners of the vapour region.

The vapour has now completely collapsed. The vapour implosion causes a significant increase in pressure

The initial vapour collapse causes a rebound and a jet shooting upward

The secondary vapour formation is greatly affected by the flow field

Fig. 4.7 – Original design: detailed sequence of the initial vapour collapse and rebound.

Pressure (bar)

Velocity Magnitude (m/s)

Liquid Volume Fraction

R (kg/m³/s ×10⁶)

0   10   20   0   10   20   0.0   0.5   1.0   -1.0   -0.5   0.0

119μs — Early in the simulation the two side gaps near the top are compressed while near the bottom they expand

179μs — Hence, the top is pressurized and the bottom cavitates except in the grooved region

239μs — Significant flow out of the upper region of the gaps

299μs — The shoe is now pulling away from the guide causing cavitation to form throughout the narrow side gaps

359μs — Fuel flows into the narrow gaps from the edges and from the centre groove, which reduces the size of the vapour regions

419μs — As the shoe slows down, the vapour region is rapidly collapsing resulting in high pressures

479μs — The initial vapour collapse and the rebound have now finished

539μs

Fig. 4.8 – Grooved design: full cycle sequence of cavitation creation and collapse.
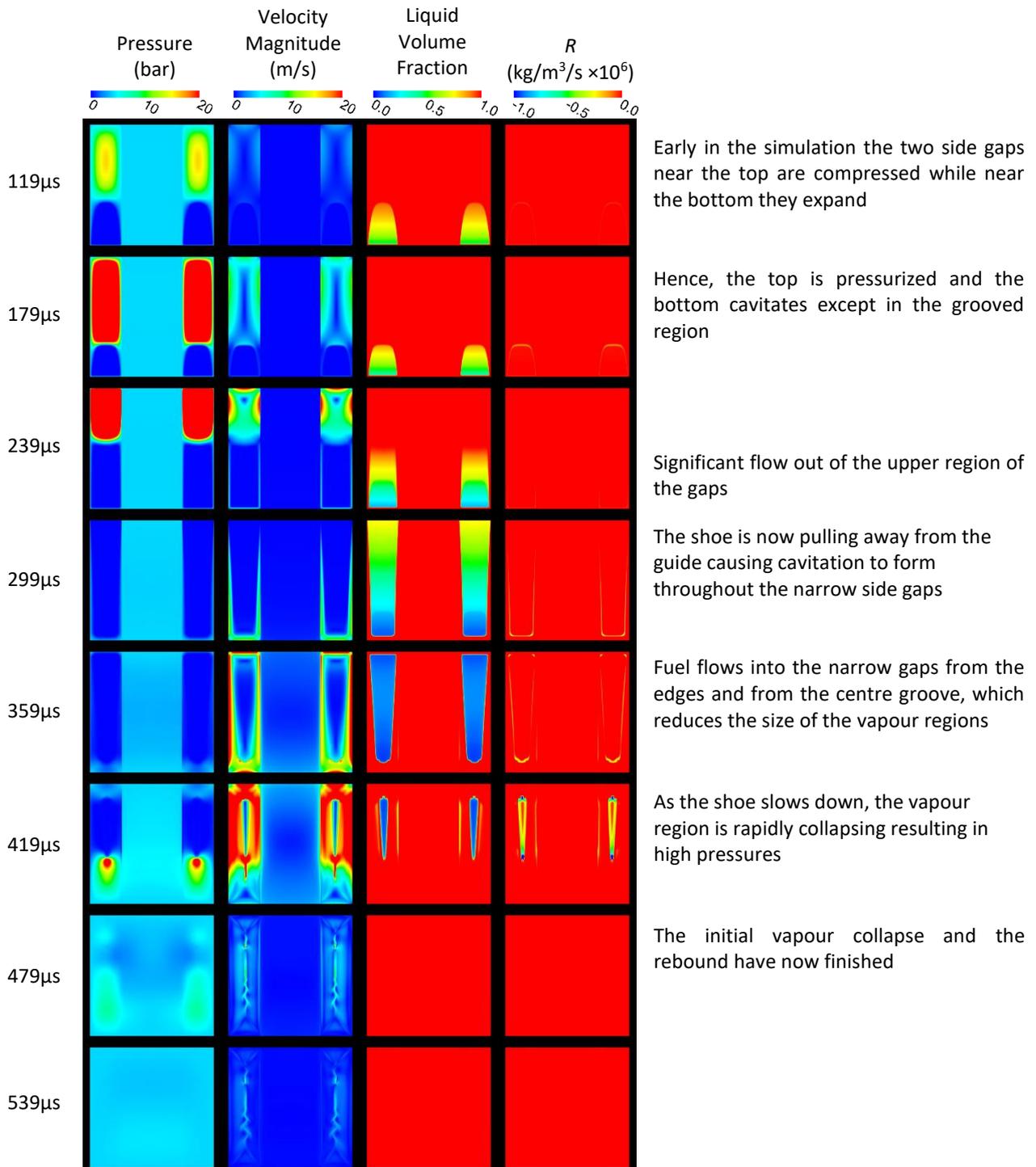
Fig. 4.9 – Grooved design: detailed sequence of the initial vapour collapse and rebound.

Fig. 4.8 shows the cycle of cavitation with the grooved design. By 119μs the effects of the shoe movement are apparent, with pressure increasing near the top and cavitation being produced near the bottom. With this design though, the cavitation is noticeably isolated to the two thin gaps, with no vapour being created in the grooved region. By 299μs, as with the original design, the narrow gaps have almost completely cavitated. However, the vapour completely condenses much earlier than in the original design. A detailed view of the vapour collapse in the grooved design (Fig. 4.9) shows almost all the initial vapour has condensed by 437μs, about 90μs before the original design. By 449μs, a vapour rebound occurs, but is smaller than that produced in the original design.

The difference in collapse time is attributed to the amount and distribution of cavitation formed and the locations where fuel from the cambox can flow into the narrow gap. The groove itself does not cavitate, as the shoe only moves a few microns and so the percentage volume change within the groove is minimal. However, for both designs, the percentage volume change in the gap is significant, and cavitation occurs because the flow from the cambox is insufficient to suppress it.

It can be concluded that in general, the groove in the modified design significantly reduces the region of the narrow gap and increases the access to the cambox pressure. This access reduces the overall amount of cavitation formed in the first place and enables an earlier collapse. However, while these factors are significant, they do not indicate if erosion will occur. Hence the need for validated ERIs.

4.5.1 - Erosion risk indicators

The maximum values related to pressure that occurred throughout the simulation period are presented in Fig. 4.10. This shows the pressure and its derivatives ($p, Dp/Dt, D^2p/Dt^2$ and $(Dp/Dt)^2$) for both the original and the grooved design.

The maxima of pressure, p, seen in the first column of Fig. 4.10, experienced a peak of 1480 bar for the original design and 875 bar for the grooved design. However, these peak values are caused by the shoe movement compressing the fuel early in the simulation (Fig. 4.11) and are not associated with cavitation collapse. Moreover, these values clearly do not exceed the pressure the material would be expected to withstand.
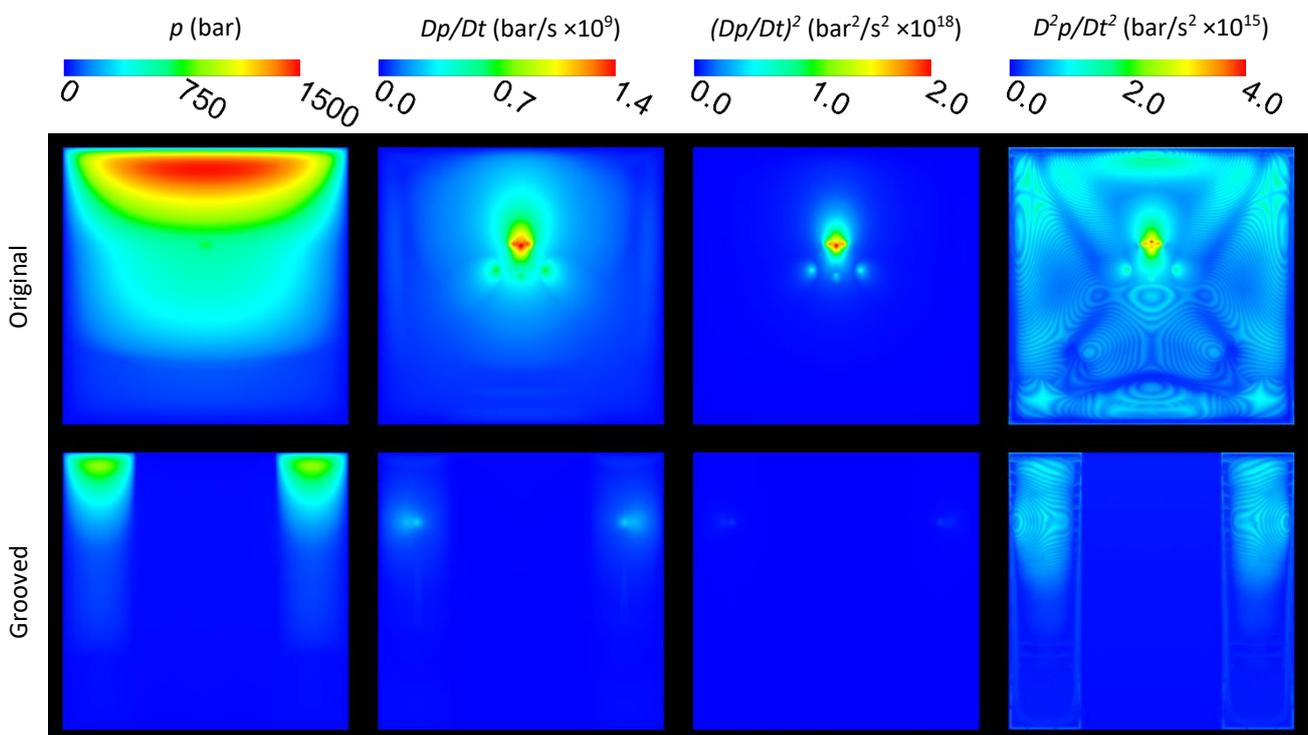
Fig. 4.10 - Potential ERIs: maximum values reached throughout the time period.

These results differ from those of some other researchers who used pressure as an ERI (for example [34]). However, defining absolute values for which damage will occur, rather than relative values or frequencies of occurrence, has significant uncertainties for different components, assemblies and methods of manufacture. Furthermore, fluid properties are not known for pressures of several thousand bar, which affects the predicted pressure values. As such, the absolute maxima of pressure is not a reliable ERI here. However, the spike produced during vapour collapse is interesting. It indicates that the rate of pressure change could be a useful indicator. Furthermore, it comes into play in the calculation of the potential power density ERI (PPD2).
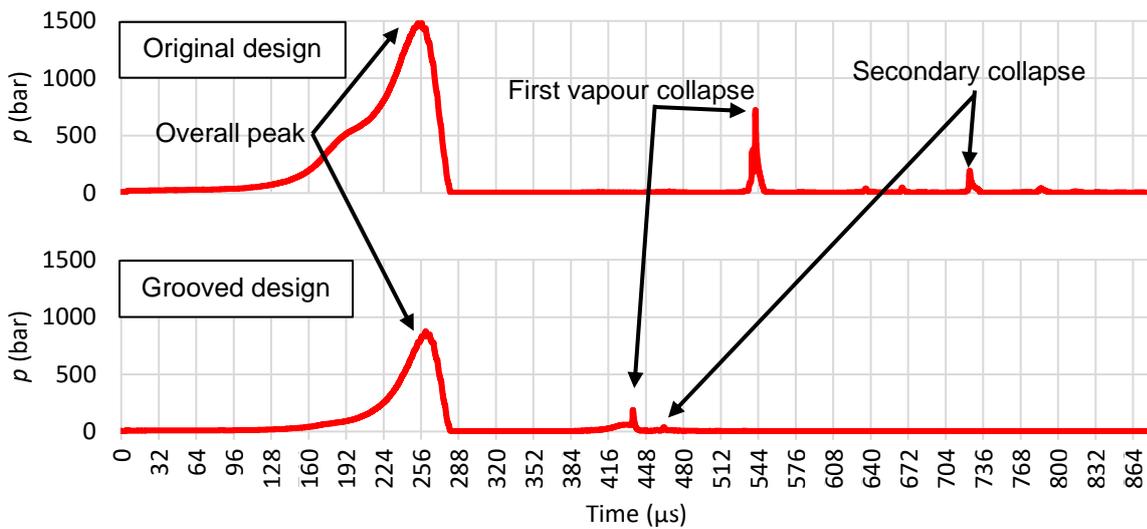
Fig. 4.11 – Maximum values of pressure on the wall during the simulation period.
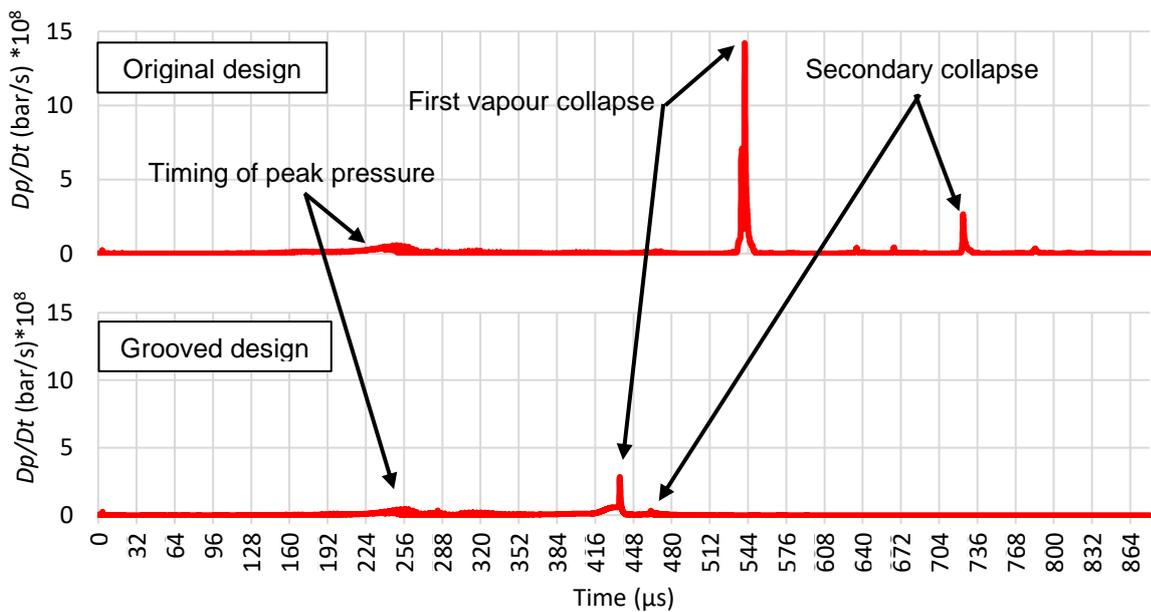
Fig. 4.12 – Maximum values of Dp/Dt on the wall during the simulation period.

The second column in Fig. 4.10 shows the distribution of maximum Dp/Dt for the two designs. A clear peak is seen on the original design and its location coincides with that of the erosion on the hardware (Fig. 4.2). Moreover, Fig. 4.12 shows that this peak occurs during the collapse of vapour. The peak value reached was 14×10^8 bar/s. There is also some activity on the grooved design, but at 2.8×10^8 bar/s it is significantly lower than in the original case. These results show that Dp/Dt is useful as an ERI. The third column in Fig. 4.10 shows maxima of $(Dp/Dt)^2$, which further accentuates the differences between the two designs seen with Dp/Dt. This $(Dp/Dt)^2$ ERI is newly derived for this work and provides distinct advantages.

The fourth column in Fig. 4.10 shows the maxima of D^2p/Dt^2 (see Appendix B for the equation). The CFD results show high values that correlate well with where erosion was found on the original design hardware, but there is also a lot of activity elsewhere in the domain. As such, D^2p/Dt^2 does not provide a better indication of erosion risk than Dp/Dt.

Dp_d/Dt (bar/s $\times 10^8$)

Fig. 4.13 - Potential ERI: maximum values reached throughout the time period.

The maxima for the material derivative of dynamic pressure (Dp_d/Dt) is shown in Fig. 4.13. On the original design, the locations of the peak Dp_d/Dt lines up well with the region of erosion. However, similar values are reached with the grooved design caused by the collapse of vapour. Thusly, for this component at least, the material derivative of dynamic pressure is not considered a viable ERI. As expected, the overall peak values reached are substantially less than those of the static pressure counterparts.

The R during condensation (R_c) and the material derivatives of density ($D\rho/Dt$) and liquid volume fraction ($D\alpha_l/Dt$) were also considered as potential ERIs (Fig. 4.15). As mentioned earlier, a skewed cross-shape is notable. This cross was produced as the inward flows from the boundaries impinged on each other. Unsurprisingly, the maximum values of these indicators produced similar contour images. For all three potential ERIs, the original design has maxima in the location of erosion, but the grooved design has similar values where there was no cavitation erosion present on the hardware after endurance tests. Hence, these parameters do not show potential as ERIs for this component.

Derivations from other researchers' published works were also considered for their potential as ERIs. Accordingly, the distribution of maxima of potential power density, *PPD2* (Eq. 33) and of acoustic pressure, P_a (Eq. 31) were calculated.
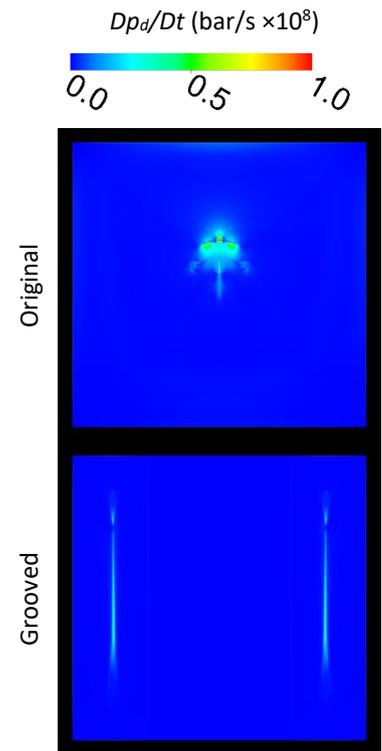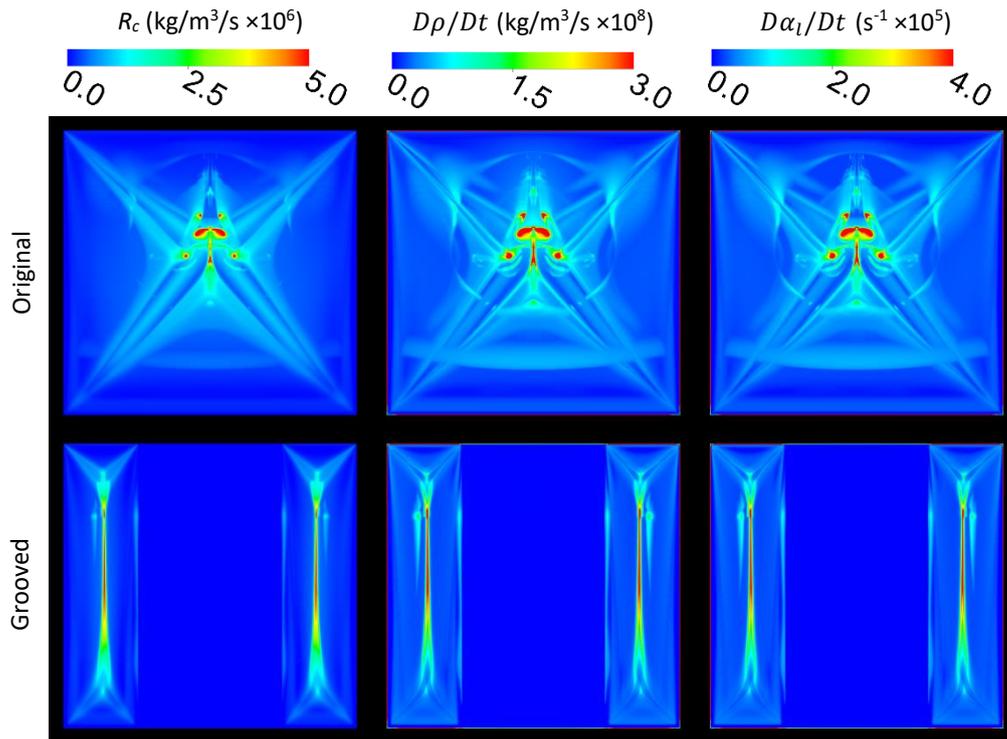
Fig. 4.15 - Potential ERIs: maximum values reached throughout the time period.
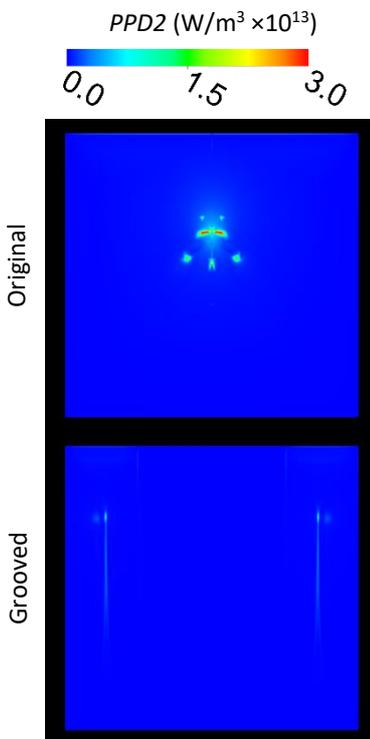

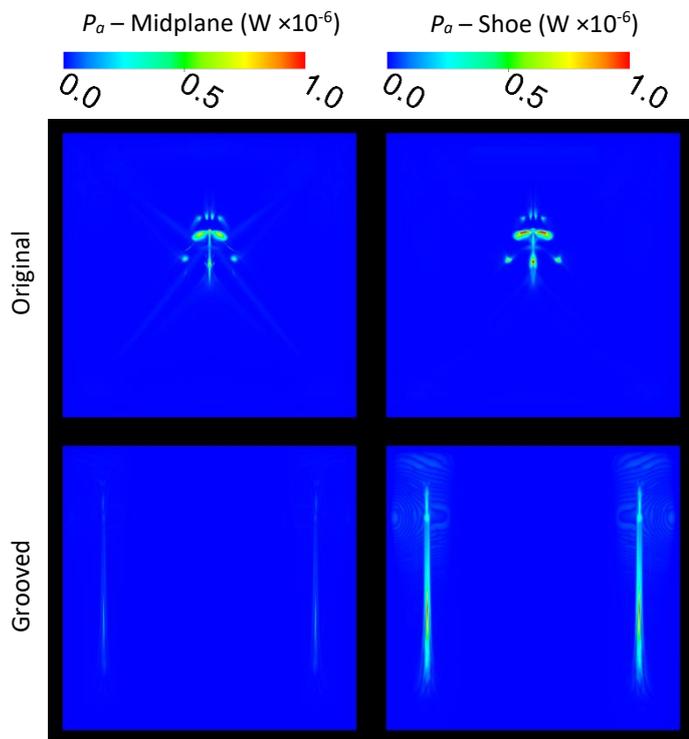Fig. 4.14 - Potential ERIs: maximum values reached throughout the time period.

Fig. 4.16 - Potential ERI: maximum values reached throughout the time period.

The distribution of maxima for *PPD2* is shown in Fig. 4.14. *PPD2* shows a clear difference between the original and grooved designs. Moreover, on the original design, *PPD2* produces a clear shape that resembles the distinctive erosion pattern seen on a particular hardware sample, shown in Fig. 4.2-C. Hence, *PPD2* is a good ERI and provides clearer results.

All the CFD images shown so far have been on the mid-plane between the shoe and the guide. The ERIs directly on the faces of the shoe and the guide were also investigated but did not change the assessments for 9 out of the 10 ERIs (see Appendix D). Acoustic power (P_a) was the one exception, as seen in Fig. 4.16. The distribution of the maxima on the mid-plane could indicate that P_a would be a reliable ERI, with high values only in the region of erosion on the original design. However, unlike the other ERIs considered, the results on the shoe surface contradict this. The maxima on the shoe surface on the grooved design reach similar values as the original design, which indicates that P_a would be misleading as an ERI.

The qualitative assessments of the different ERIs tested are summarized in Table 4.3. ERIs that did not provide a clear difference between the prototype and modified design are labelled "poor." ERIs that provided the clearest difference between the two designs, and where the locations of the maxima correlated well with erosion seen on the hardware, are labelled "good." The other erosion indicators are labelled "some" as they provide only a limited indication of erosion potential.

Table 4.3 – List of potential ERIs and their correlation level.

Variable	Variable name	ERI correlation
p	Pressure (static pressure)	Poor
Dp/Dt	Material derivative of pressure	Some
D^2p/Dt^2	Second material derivative of pressure	Some
$(Dp/Dt)^2$	Material derivative of pressure, squared	Good
Dp_d/Dt	Material derivative of dynamic pressure	Poor
R_c	*R* during condensation	Poor
$D\rho/Dt$	Material derivative of density	Poor
$D\alpha_l/Dt$	Material derivative of liquid volume fraction	Poor
PPD2	Second derivation of potential power density	Good
P_a	Acoustic power	Poor
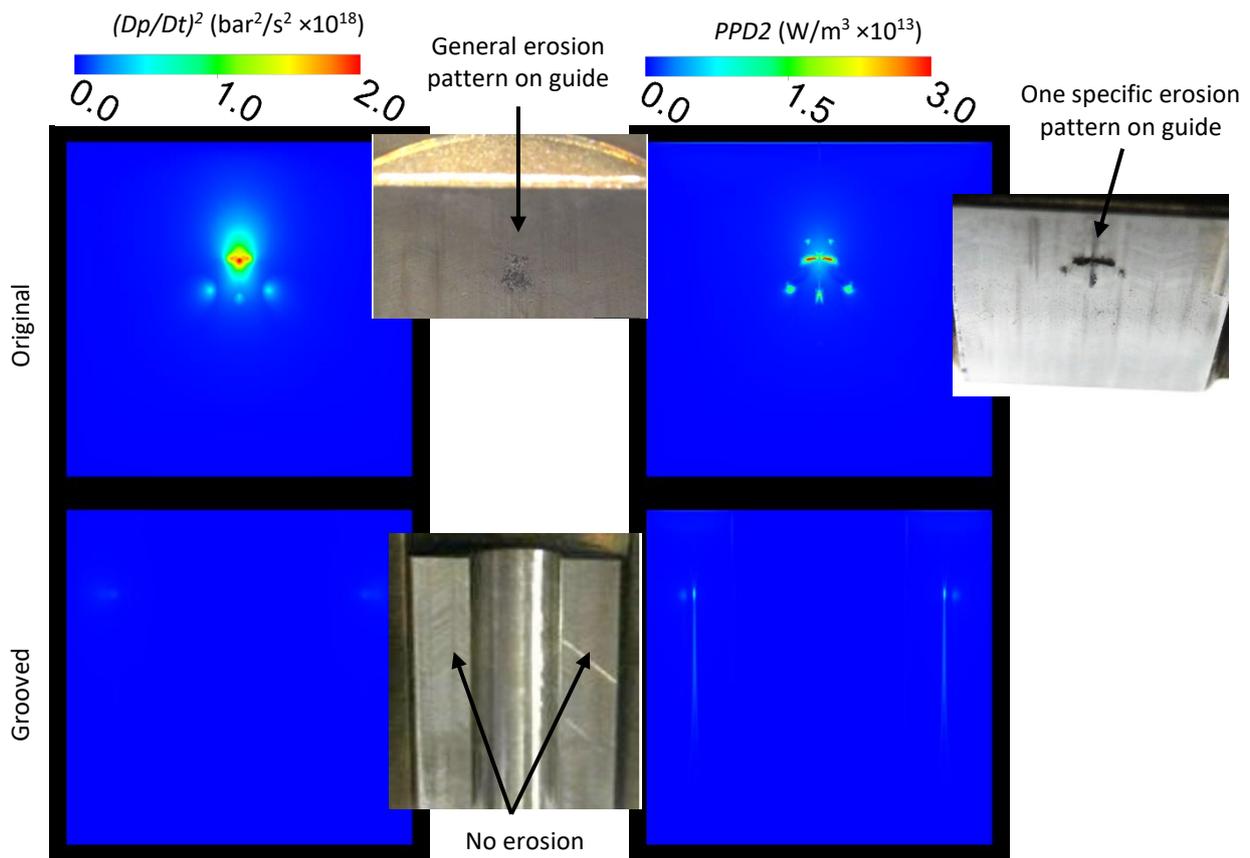
Fig. 4.17 – The two most successful ERIs and images of hardware.

Fig. 4.17 shows the two best ERIs, $(Dp/Dt)^2$ and *PPD2*, and how well the location of the maxima correlates with that of erosion on the hardware. These two indicators targeted the correct location and showed significantly higher peak values on the original design. They also reproduce the distinctive pattern of erosion seen on the original hardware design on the guide.

These two ERIs can be applied to product design and development. For example, an existing production component that is free of erosion can be used as a control case to establish the distribution and intensity of the ERIs. The ERIs for any new or modified design can then be compared with the control case. A significant worsening of the ERI characteristics would indicate a region at risk of erosion. In this way, considerable time and cost would be saved during product development.

4.6 - Conclusion

The fluid dynamics of a thin liquid filled gap were investigated. This gap occurs within a Shoe and Guide assembly, which is located below the pumping plunger in a high-pressure fuel pump. Two designs were considered, the original, which experienced non-critical cavitation erosion, and a modified design, that had a groove in the guide face which eliminated the erosion. The dynamic CFD simulations provided understanding

and visualization of the cavitation characteristics in the gap. These results confirmed that the creation and collapse of cavitation within the gap was caused by the expected small lateral movement of the shoe, which occurred near the top of the pumping stroke.

The results for the two different designs were further analysed to evaluate several potential ERIs. Each indicator was assessed by comparing the distribution of its maximum values with images of cavitation erosion on the hardware. Almost all the ERIs targeted the correct region at risk of erosion on the original design. However, it is important to note that it was only by comparing the CFD results of the damaged design with those of the undamaged design that a reliable assessment of the ERIs could be made. Accordingly, the ERIs that gave the most accurate results were $(Dp/Dt)^2$ and *PPD2* (Eq. 33). $(Dp/Dt)^2$ was newly derived for this research and *PPD2* was proposed by Fortes-Patella et al [71] [72]. It is now anticipated that using these two ERIs to guide product design and development will save considerable time and cost.

5 - Cavitation erosion risk indicators for a Control Orifice within a diesel injector

5.1 - Introduction

The diesel injector is of critical importance to the performance of engines and is an area for continued development to meet future environmental and performance standards. As cavitation cannot be avoided in diesel injectors, due to the flow conditions required for optimal performance, it is essential to further understand and manage cavitation. By doing this, advancements in the optimization of performance and production can be achieved, while avoiding potential complications due to cavitation or cavitation erosion.

This section is dedicated to further determining ERIs, and how they compare when applied to flow within a Control Orifice in a prototype high-pressure diesel injector. Two designs of the same component were used to validate the findings, one eroding and on non-eroding. ERIs, many newly developed for this work, were assessed with both designs. By benchmarking the CFD results with a non-eroding design the ERIs could be more thoroughly evaluated. Furthermore, this work utilized an increased mass transfer rate (R), which comes from Koukouvinis et al [40]. Another aspect considered as an ERI was the frequency of spike occurrence from selected ERIs, rather than just examining maximum values and their distribution on the walls [125]. Moreover, the component utilized in this CFD study has a direct link to the real-world, unlike specialized test geometries (see [30], [40] or [73] for example).

See section 1.2.6.3 for an in-depth literature review of ERIs from previous researchers and section 1.2.9 for a thorough review of cavitation in control orifices. As a brief reminder, regarding the erosive properties of cavitation, Gavaises et al [33] indicated that bubble implosion could have a significant effect on erosion within diesel injector tips. They had proposed erosion was associated with acoustic pressure calculated from the cumulative effect of many bubbles collapsing close to a boundary. Koukouvinis et al [68] went on to simulate the effects of the energy released by cavitation collapse on the internal surfaces of diesel injector tips. They were able to predict some regions of cavitation erosion based on a cavitation aggressiveness index. This index was related to peak pressures and the rate of change regarding the pressure and vapour volume fraction. Mihatsch et al [73] also studied cavitation erosion potential due to the rate of vapour collapse, but on a multicell volume basis rather than a single mesh cell basis. They were also able to show agreement between regions of cavitation erosion in CFD and experimental results. However, with all three of these references, there were no designs free of erosion to benchmark and compare the eroding results to.

In chapter 4, (and in Brunhart et al [146]) the ERIs in a narrow gap of a high-pressure diesel fuel pump were investigated. Out of 10 potential ERIs, two were found to be useful, the squared value of the rate of pressure change $(Dp/Dt)^2$ and the second definition of potential power density (*PPD2*). The importance of a non-eroding designs was made apparent as almost all the potential ERIs indicated the correct location of erosion as compared to the hardware, while only a select few of the potential ERIs gave corresponding low results on the non-eroding design.

This section investigates a Control Orifice (Fig. 5.1) in an automotive high-pressure fuel injector. It is called the spill orifice (SPO) and is one of the orifices involved in controlling the rate of opening and closing the needle valve during fuel injection. As with all prototypes, the designs were subjected to extensive testing during product development, including endurance tests. During development, one such endurance test resulted in significant cavitation erosion of the orifice. Further development of the component eliminated the erosion and subsequent prototypes were free from damage.

A CFD investigation was conducted to understand the flow-field and cavitation characteristics in and around this control orifice, and to explore possible indicators for cavitation erosion risk. The analyses used two design levels: the original geometry which suffered from erosion (prototype design) and a subsequent prototype design where the erosion had been eliminated (modified design).

For increased accuracy and detail, this work utilized a hybrid LES-RANS turbulence model: Detached Eddy Simulation (DES). This type of model has shown improvement over RANS models and resolves issues like early cavitation collapse and poor vapour phase transport, which are known issues with RANS models [33] [28] [29] [32]. The DES simulations were first run using the standard ZGB model. Then a modified ZGB method was used, which enabled significant changes to be specified to the rate of mass transfer. The CFD results were examined and different simulation methods considered. The potential ERIs were examined and compared with photographic evidence of damage on early prototype components.

In section 5.2 and 5.3 the hardware geometry and experimental results are presented, respectively. The specific simulation methodology is described in section 5.4 (more general topics are covered in chapter 2). In section 5.5, results for three different cases are presented. Focus is placed on cavitation structures and potential ERIs considered. Finally, a summary and conclusion are presented for the SPO in section 5.6.

5.2- Experimental procedure and results

Newly proposed injector designs must all go through a rigorous testing process. One of these tests is an endurance test, which consists of exposing the prototype injector to a high typical load cycle (2200 bar injection cycle) for x-many cycles. This type of test is essential to determine if a prototype can withstand

everyday use and is ready for serial production. An example of slight damage following endurance testing can be seen in Fig. 5.1 and sever damage in Fig. 5.2. After these early prototype tests the component was redesigned and retested. The erosion was eliminated, and the subsequent prototype designs were free from damage. The material used was automotive high strength steel with surface treatment.
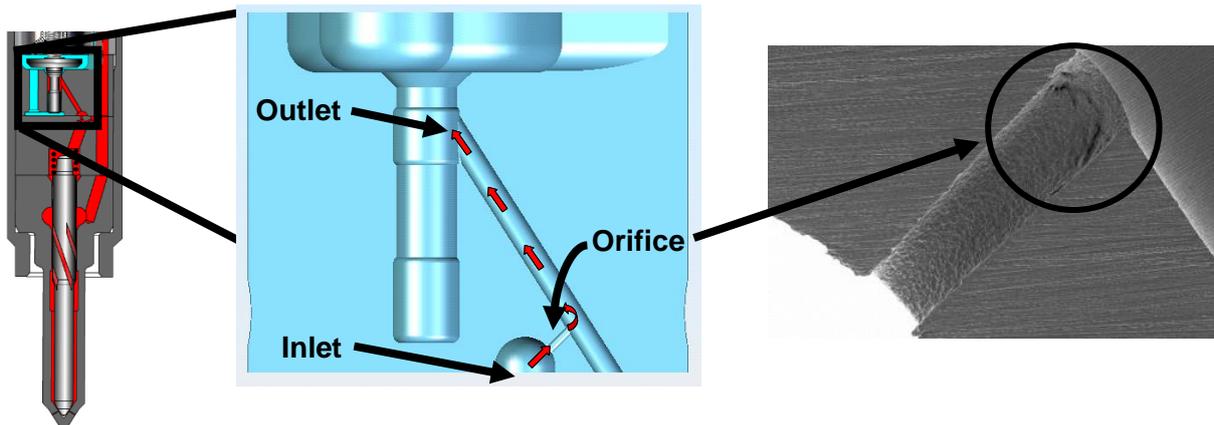
Fig. 5.1 - Left: Location of the Control Orifice in a sketch of a diesel injector. Centre: General geometry used in the simulation showing flow direction and regions of interest. Right: An early prototype after an endurance test. Specimen shows signs of cavitation erosion in the region circled.
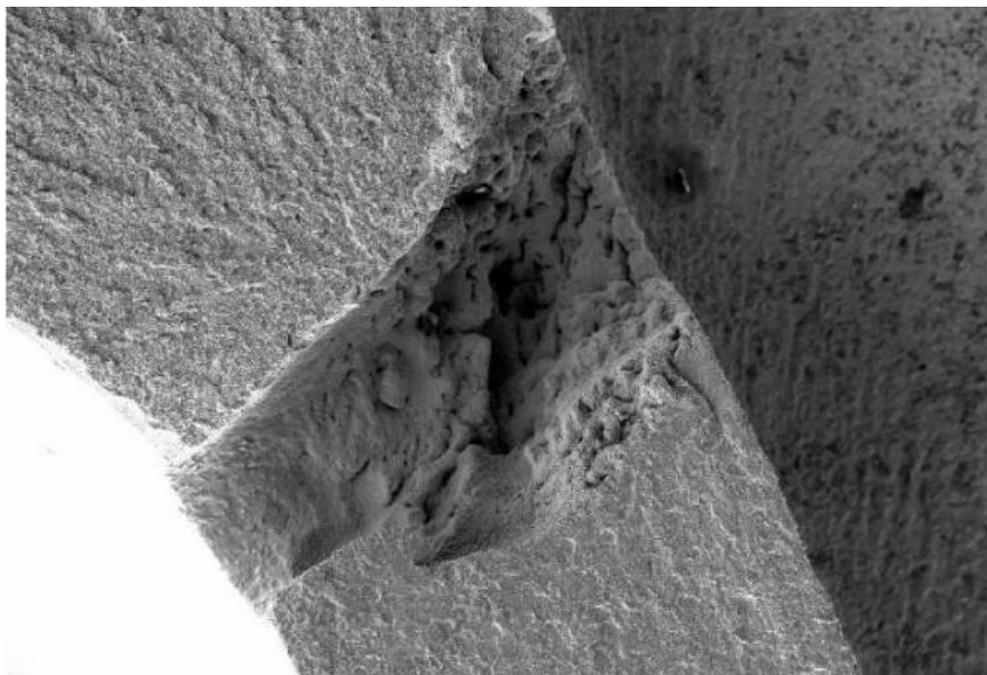

Fig. 5.2 - An early prototype sample showing sever signs of cavitation erosion after an endurance test. Subsequent design modifications eliminated the erosion.
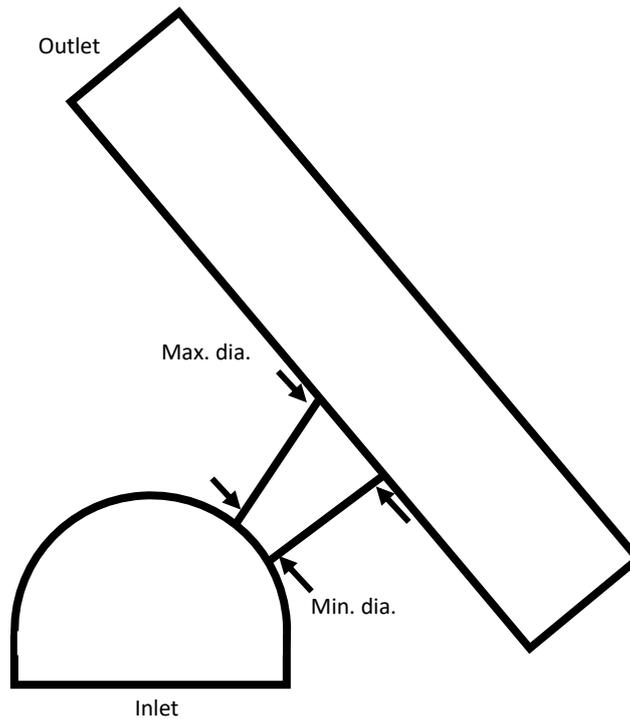
Fig. 5.3 – Basic geometry of the Control Orifice

5.3 - Geometry

Exact dimensions cannot be given as the design comes directly from an industry prototype, but the general schematic is shown in Fig. 5.3. Both the original and modified designs had an orifice entry diameter in the region of 0.22mm and a slight divergent taper in the direction of flow. The differences between the designs are relatively miniscule and in the order of a few microns. The taper for the modified geometry was slightly less, (i.e. closer to parallel) and the entry diameter was a few microns smaller. Both designs passed manufacturing pass-off tests, which look for specific required flowrates given different standard pressure conditions. This ensures that the orifices will perform as required under the different operating conditions.

5.4 - Brief overview of simulation model and methodology

The inlet volume consisted of a polyhedral mesh. The mesh throughout the orifice and outlet drilling was constructed of hexahedral cells (Fig. 5.4). The first cell size on the orifice wall was 100nm which provided a suitable Y+ close to 1 throughout the simulations. The length of the cell in the direction of the flow in the orifice was about 4μm, which corresponds to λ, the Taylor length scale [116]. The CFL criteria was met (CFL < 1) with a time-step of 2ns and corresponded to τ, the Kolmogorov time scale. Both designs had a mesh of around 9×10^{6} cells. Coarser meshes were also tested and resulted in poorer characteristics, such as Y+ and number of iterations for convergence, but they had the same flow rate.
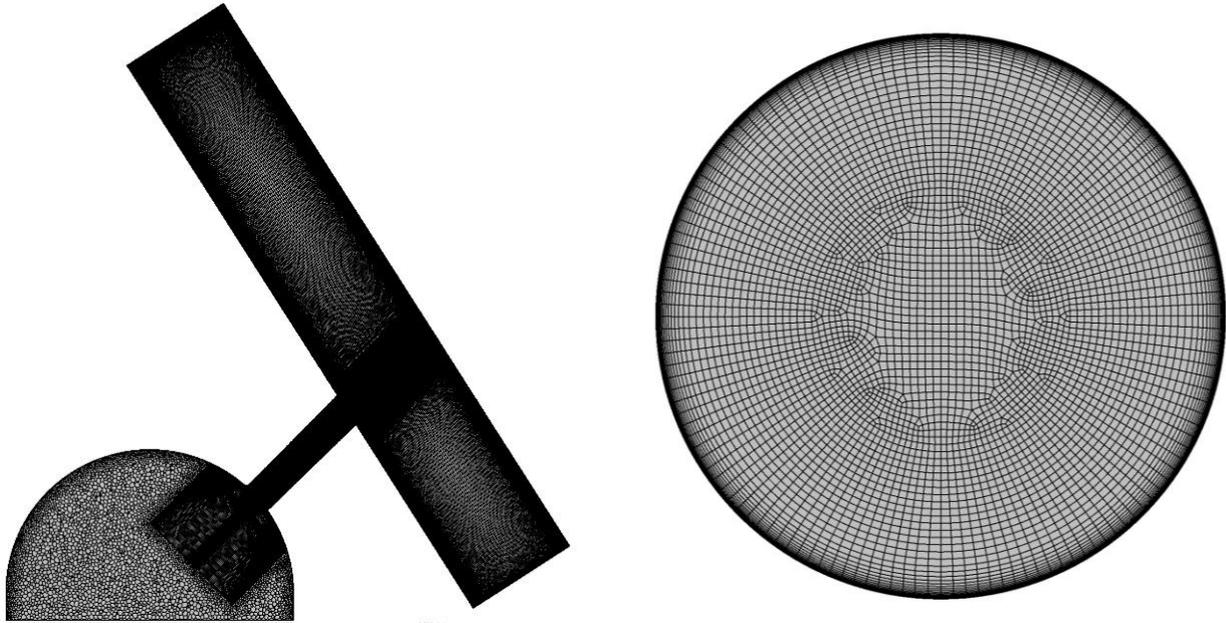
Fig. 5.4 – Mesh on the mid-plane of the whole domain and a cross section in the orifice.

Initial CFD simulations used RANS with a *k-ε* turbulence model alongside the standard ZGB cavitation model. The RANS simulations were used for the low computational costs and previously seen accuracy in predicting the coefficient of discharge (Cd) when implemented with due care ([44] [133]).

Later simulations used a DES turbulence model. The simulations were implemented in ANSYS Fluent v17 as Improved Delayed Detached Eddy Simulation (IDDES), as first proposed by Shur et al [37]. IDDES is a more recent version of DES and is better suited for high Re flows. This simulation setup was previously validated with experiments for a similar operating environment by Bush et al [32] and is also congruent with Koukouvinis et al [40]. See section 2.2.3 for further details about the DES turbulence model and why it was used for this study.

The simulations were run with constant boundary conditions. An upstream pressure of 1380 bar and downstream pressure of 340 bar were used. These pressures were selected as they were present during much of a 2200 bar injection cycle and provided the largest pressure difference across this orifice. The resulting *CN* and Re was 3.06 and 40,000, respectively. The CFD simulations were initially tested against manufacturing pass-off flow tests as a benchmark.

As the pressure drop is relatively high a compressible fluid was used. The EoS are representative of Normafluid (ISO4113), a standard fluid used in automotive testing. These EoS come from [47] and [122] and are discussed in-depth in chapter 2.3.2. Reference values are given at 60°C and 340 bar in Table 5.1. The vapour was considered incompressible as any large change in pressure occurs while the fluid is in the liquid phase. Note though that due to mass transfer, the mixture can still be considered compressible [6].

For some simulations R was increased, similarly to the work of Koukouvinis et al [40]. The ZGB cavitation model was implemented with the value of the mass transfer constants defined to create an effect closer to that of a barotropic model (see chapter 2.5 for details). For this work, a large but practical value of 1×10^8 for both F_{evap} and F_{cond} was used. It should be noted though that the increased mass transfer rate is not compatible with RANS simulations. Increasing R to such a high degree results in almost no cavitation being present when using RANS due to the unrealistic rapid pressure recovery.

Table 5.1 – Fluid properties at 340 bar and 60°C.

Property	Liquid (*l*)	Vapour (*v*)
Density (kg/m^3)	816	6
Bulk modulus (bar)	15,973	
Speed of sound (m/s)	1,399	
Dynamic viscosity (kg/m/s)	2.13×10^{-3}	4×10^{-6}

5.4.1 - Erosion risk indicators

This work also explores variations of published ERIs and several new ones (Table 5.2). The potential ERIs were assessed by examining the magnitude and distribution of the maximum values reached during the simulation periods. The ERI results were then compared to the location of erosion as seen on hardware. The overall sign of a successful ERI was a high level of correlation of maxima locations with erosion as seen on the original hardware design, along with low peak values on the modified design. Frequency of maxima occurrence was also considered for four of the potential ERIs.

Table 5.2 – List of ERIs investigated with this geometry.

Variable	Variable name	Variable	Variable name
p	Pressure (static pressure)	$D\alpha_l/Dt$	Total derivative of liquid volume fraction
Dp/Dt	Total derivative of pressure	$d\alpha_l/dt$	Partial derivative of liquid volume fraction
D^2p/Dt^2	Second total derivative of pressure	$d^2\alpha_l/dt^2$	Second partial derivative of liquid volume fraction
dp/dt	Partial derivative of pressure	p_d	Dynamic pressure
$-Dp/Dt$	Negative values of the total derivative of pressure	Dp_d/Dt	Total derivative of dynamic pressure
$(Dp/Dt)/V_{cell}$	Total derivative of pressure divided by the cell volume	$\nabla \cdot (\boldsymbol{U})$	Divergence of velocity
$(Dp/Dt)^2$	Total derivative of pressure squared	$D\boldsymbol{U}/Dt$	Acceleration
$D\rho/Dt$	Total derivative of density	$PPD2$	Second derivation of potential power density
$d\rho/dt$	Partial derivative of density	P_a	Acoustic pressure
R_c	Condensing R		

5.5 - Results and discussion

An overview of the three cases examined is given in Table 5.3. The first results presented are from a RANS simulation with the standard ZGB cavitation model and default R values. Then the results of a DES simulation with the same ZGB cavitation model and R values are presented. Lastly, results of a DES simulation coupled with ZGB and an increased R are examined.

Table 5.3 – List of the different simulations sets and results overview

Case	Description	ZGB R variables	Min pressure (bar)	General outcome (Original vs. modified)
1	RANS with standard ZGB and default values	Default F_{cond}=3e4, F_{evap}=7.5e4	-500	Region of recirculation and backflow in the original design
2	DES with standard ZGB and default values	Default F_{cond}=3e4, F_{evap}=7.5e4	-500	No obvious differences between designs
3	DES with increased R	Increased R F_{cond}=F_{evap}=10^8	-8	Several ERIs show difference between the two designs

5.5.1 - Case 1 – RANS simulation, default ZGB R values

Fig. 5.5 show cavitation and velocity on the mid-plane for both the original and modified designs. The results for the eroding geometry show a region of recirculation and backflow at the end of the topside of the Control Orifice, whereas the non-eroding geometry does not. This region correlated with part of the location of erosion seen in the failed endurance test images (Fig. 5.1 & Fig. 5.2).
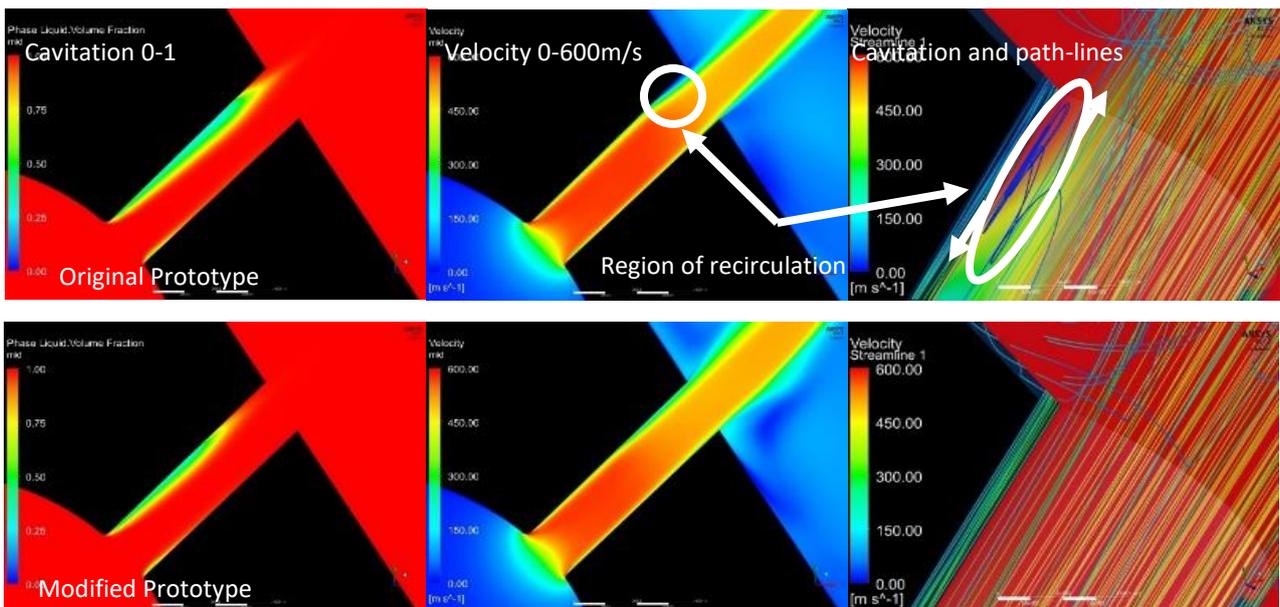

Fig. 5.5 - Mid-plane section of the original and modified RANS simulations (Case 1, RANS with standard ZGB). Region of recirculation and backflow prominent in the original design.

For much of the CFD work performed in industry, the RANS technique for modelling turbulence is still the method of choice due to its acceptable time scale compared with LES/DES techniques. Hence, it is worth noting that the Case 1 RANS model results demonstrated a significant difference between the original and modified geometries. However, it is possible this difference was only case specific. Although, it is interesting that the difference was in the region of erosion which suggests that backflow and recirculation, close to collapsing vapour structures, may result in an increased risk of erosion. Nevertheless, further analysis is required.

5.5.2 - Case 2 – DES simulation, default ZGB R values

The maximum pressure (p) on the wall (Fig. 5.6) appears to be relatively stable. Maximum values of Dp/Dt appears to have some activity, the values are relatively small (2 orders of magnitude less than in case 3, where R is increased). Furthermore, the other potential ERI results showed no substantial differences between the original and modified geometries. As such, no conclusions could be drawn as to which of the potential ERIs were viable with these turbulence and cavitation models. Moreover, there was still an unreasonable negative pressure present, and so the R values were increased.
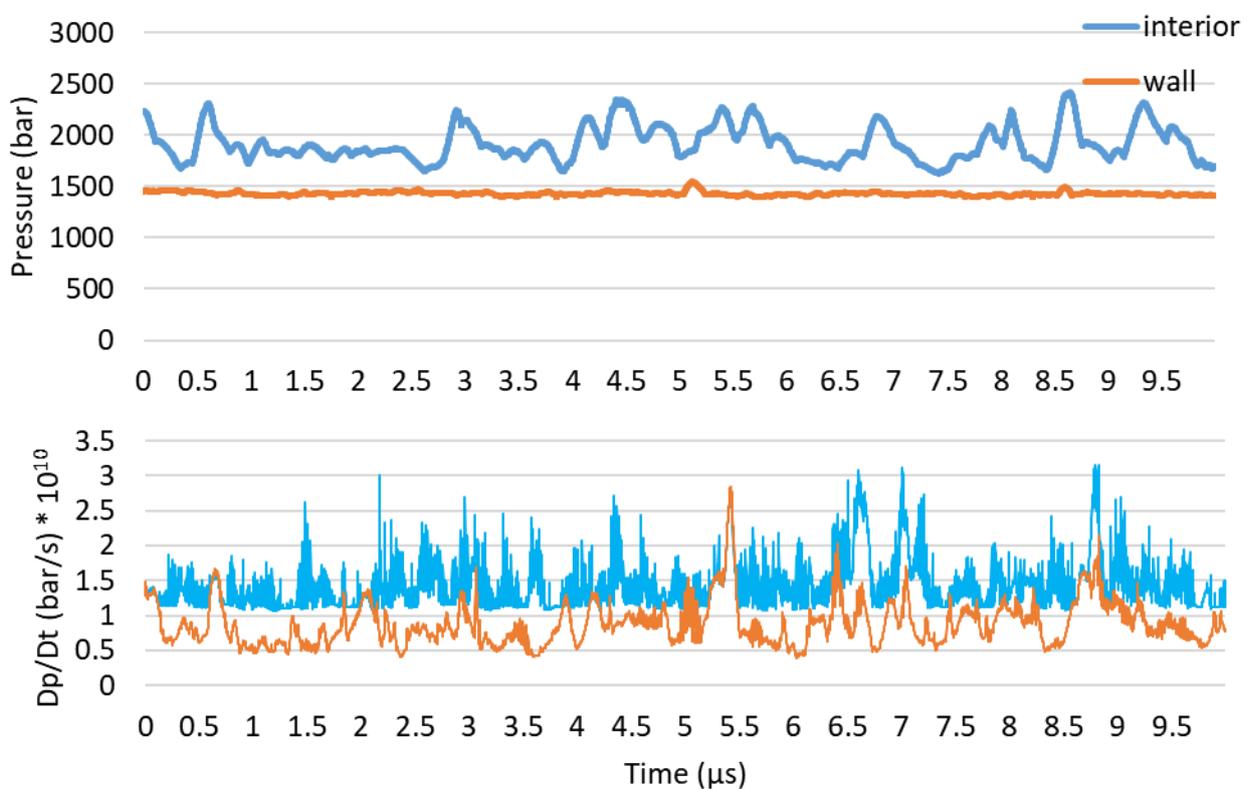

Fig. 5.6 - Case 2 (DES with default R). Maximum p and Dp/Dt in the entire domain (interior) and on any surface (wall) for 10 µs after initialization on the original prototype design.

5.5.3 - Case 3 – DES simulation, increased ZGB *R* values

A key improvement from increasing *R* was the lack of negative pressure predicted, which commonly occurs in cavitating simulations and is a non-physical effect (Table 5.3). This negative pressure is a numerical inaccuracy due to the low mass transfer rate. When post-processing, users generally cap the vapour pressure and ignore the negative values. However, it should be noted that while convergence was obtained using the increased *R* there was a noticeable increase in the run time of case 3 compared to case 2.

An important effect of increasing *R* was the unsteadiness of the vapour region, which in turn led to more vapour pockets breaking off and collapsing (Fig. 5.7). This is assumed to be more realistic and is what is expected to lead to cavitation erosion. Maxima of two potential ERIs are shown to emerge from a collapse of vapour in Fig. 5.7. Throughout the image sequence there can be seen a region of vapour traveling in the orifice and eventually collapsing. On the same time-step there is seen new maxima on both p and Dp/Dt in the same region that the vapour collapsed.

5.5.3.1- Potential ERI – pressure and its derivatives

Plots of maxima related of static pressure and its first and second derivative (p, Dp/Dt and D^2p/Dt^2) throughout the simulated domain and on the wall for both designs over 70μs are now examined. Fig. 5.8 shows plots of the maxima of p. The peak values reached internally are lower in the original design than compared to the modified design. However, there are many more spikes of p on the wall with the original design. In total, there are 104 spikes over 2000 bar on the original design while there are only 9 spikes on the modified design. Above 3000 bar the number of spikes drops to only 12 on the original design and none on the modified design. This indicates that while there are energetic events occurring with both designs there are significantly more occurring on the walls of the original designs. However, these pressures are relatively low when considering plastic deformation of the injector material. Moreover, as mentioned in the literature review section, relying on absolute values of peak static pressure could lack robustness with the current state of CFD and so is not likely to be able to predict impulse peak pressures accurately.

Fig. 5.9 shows the plots of peak values of Dp/Dt. It is immediately apparent that there is much more activity on the original design than on the modified. Considering a cut-off value of 2e11 bar/s, there are 1748 spikes on the original design while there are only 163 spikes on the modified design. This is a much higher number of spikes than compared to p. This high activity on the original design holds true at a higher cut-off of 5e11 bar/s also, where there are 522 spikes on the original design, while there are only 34 spikes on the modified design. An FFT analysis was also preformed and showed no obvious dominate frequency (see Appendix D).

White, Vapour = 5% liquid fraction
Green, Q-criterion = 1e14 1/s^2 Top
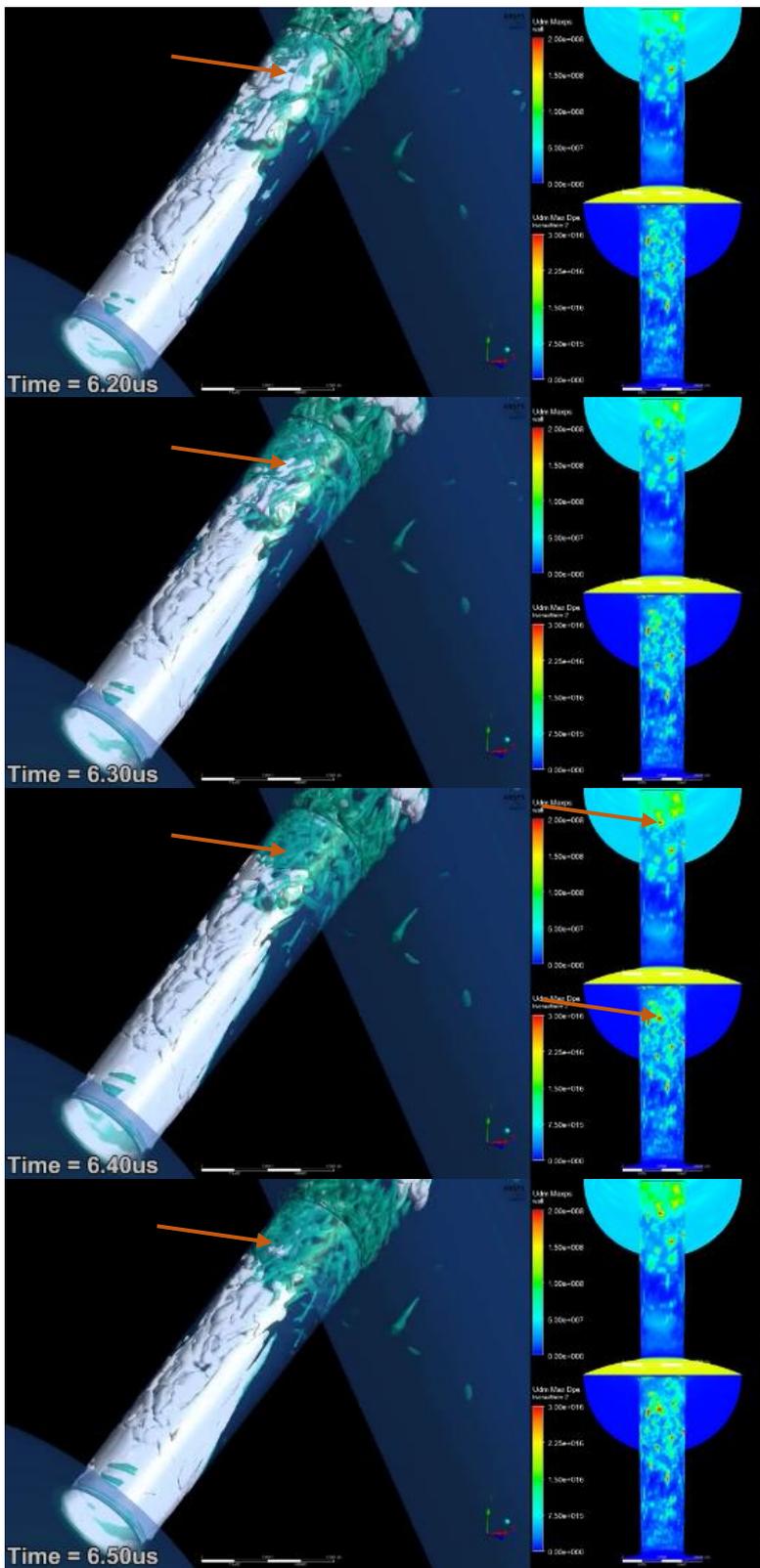
Static pressure (*p*)
0 to 2000 bar

Material derivative of pressure (*Dp/Dt*)
0 to 3e11 bar/s

Vapour collapses which leads to a spike in *p* and *Dp/Dt*

Vapour reappears after the rebound

Fig. 5.7 – Image sequence of vapour collapsing leading to a peak *p* and *Dp/Dt* as noted by the red arrows.

Plots of D^2p/Dt^2 (see Appendix B for the full equation) maxima are shown in Fig. 5.10. It is again apparent that there is more activity on the original design, but the differences between the two designs are not as strong as with p or $Dp/Dt.$ At 2e25 bar/s[2] there were about 5 times more events on the original design. This dropped to 2.5 times more events at 5e25 bar/s[2]. While D^2p/Dt^2 indicates more activity on the original design it may be harder to differentiate an eroding and non-eroding design.

While peak values are important the location of the peak values is crucial as they may have occurred anywhere in the CFD domain. Hence further analysis regarding the location of the activity was necessary.

Fig. 5.8 - Case 3 (DES with increased mass transfer rates). Maximum *p* in the entire domain (interior) and on any surface (wall) for 70 μs after initialization.
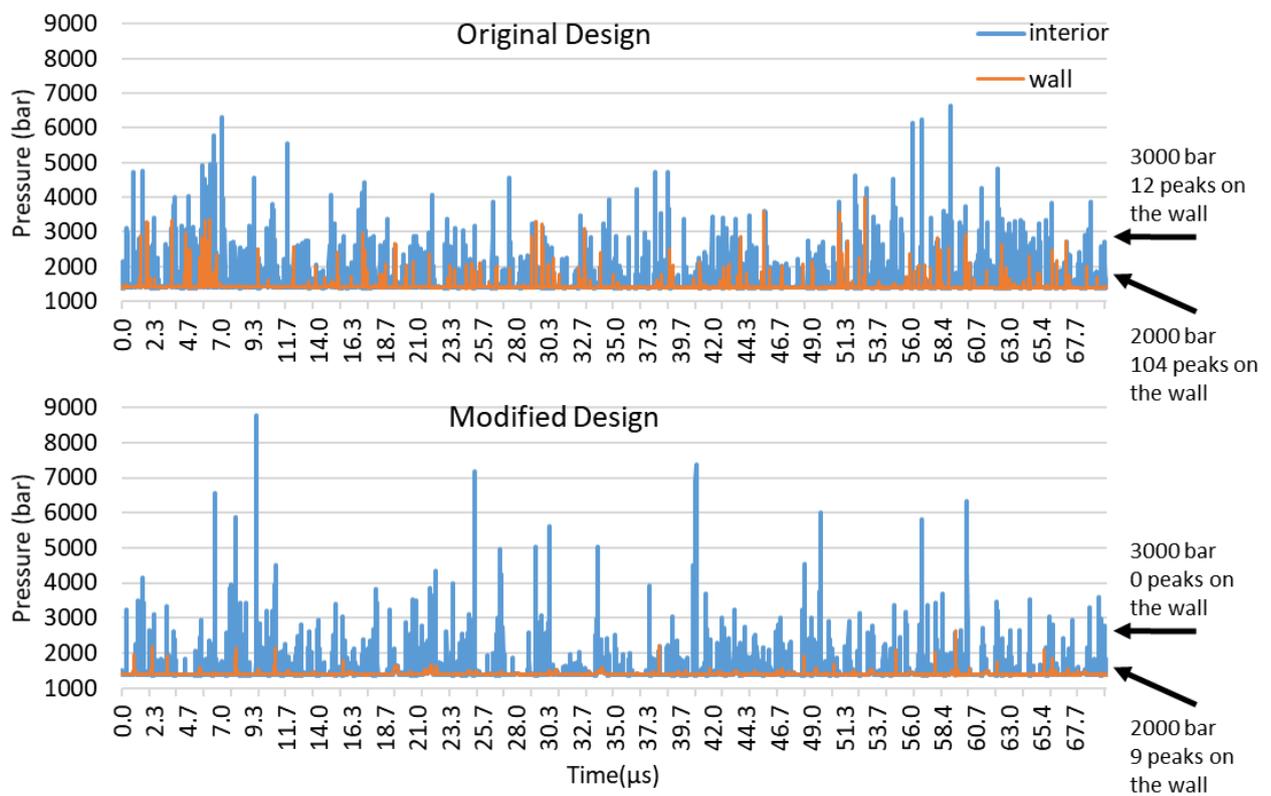
Fig. 5.9 - Case 3 (DES with increased mass transfer rates). Maximum Dp/Dt in the entire domain (interior) and on any surface (wall) for 70 µs after initialization.

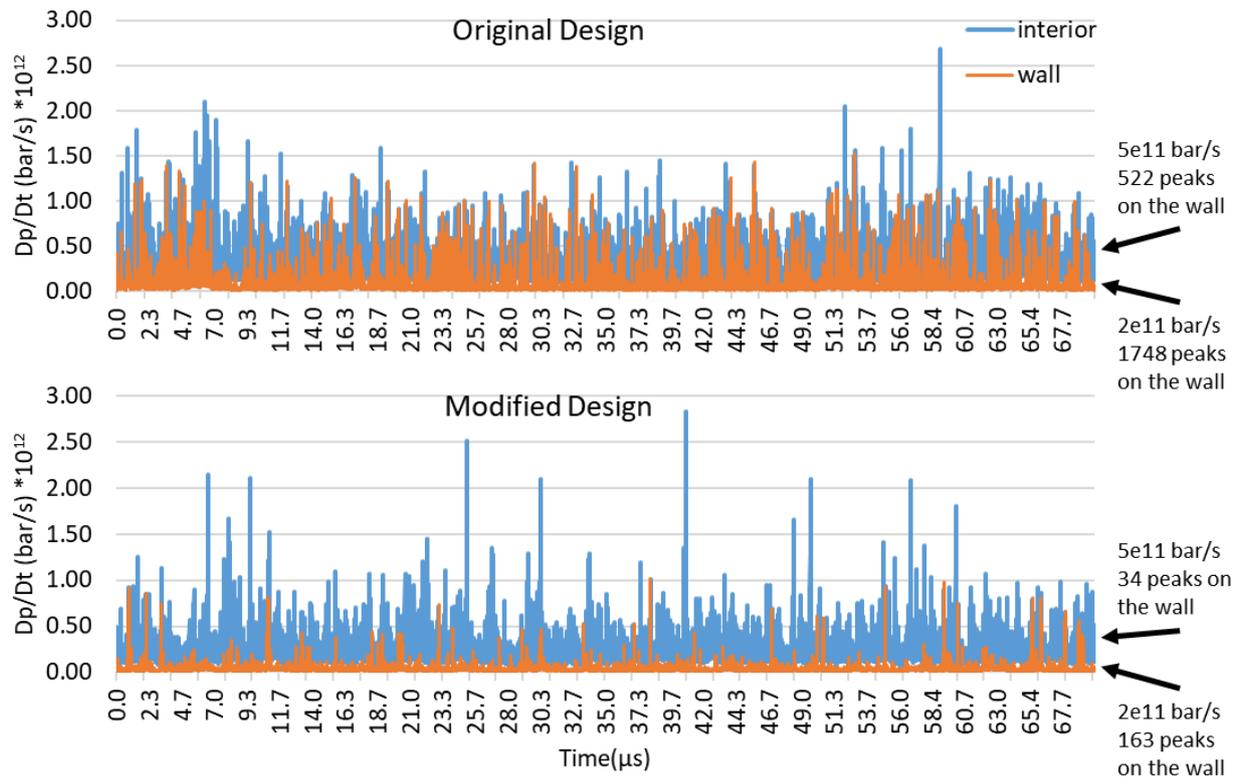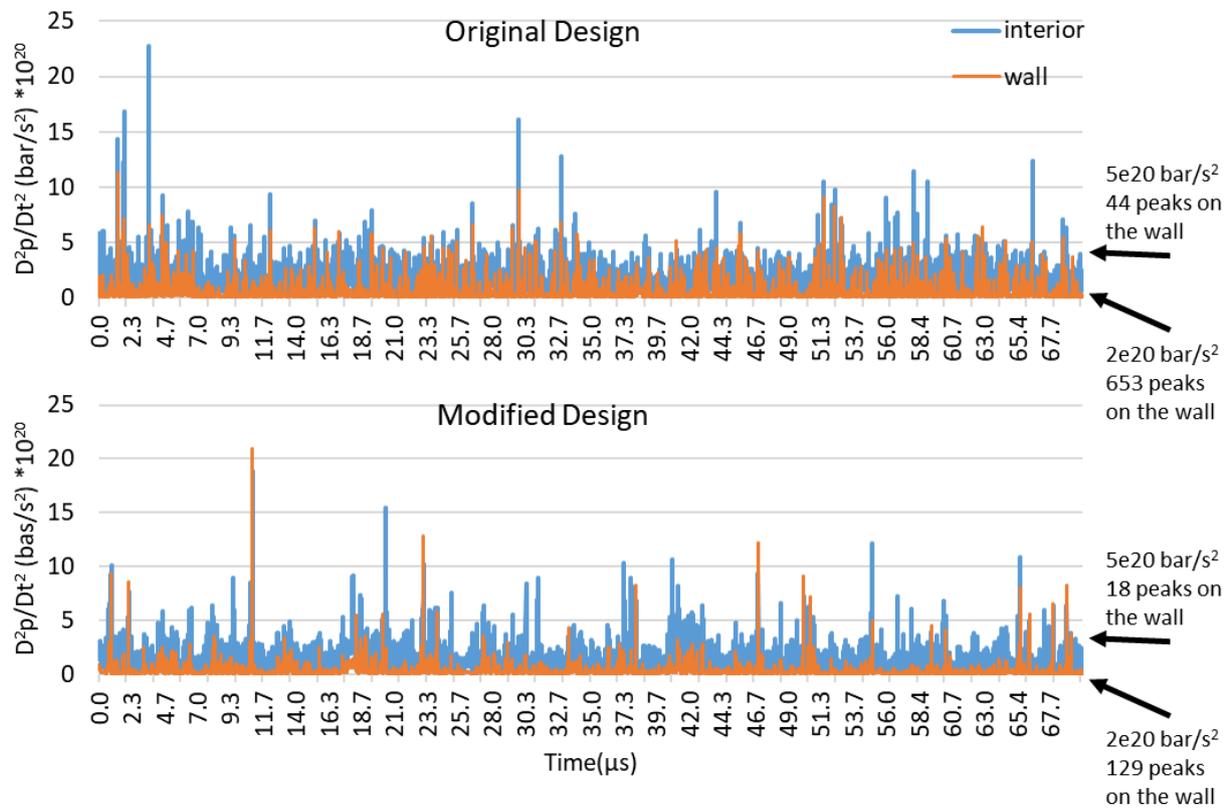Fig. 5.10 - Case 3 (DES with increased mass transfer rates). Maximum D^2p/Dt^2 in the entire domain (interior) and on any surface (wall) for 70 µs after initialization.
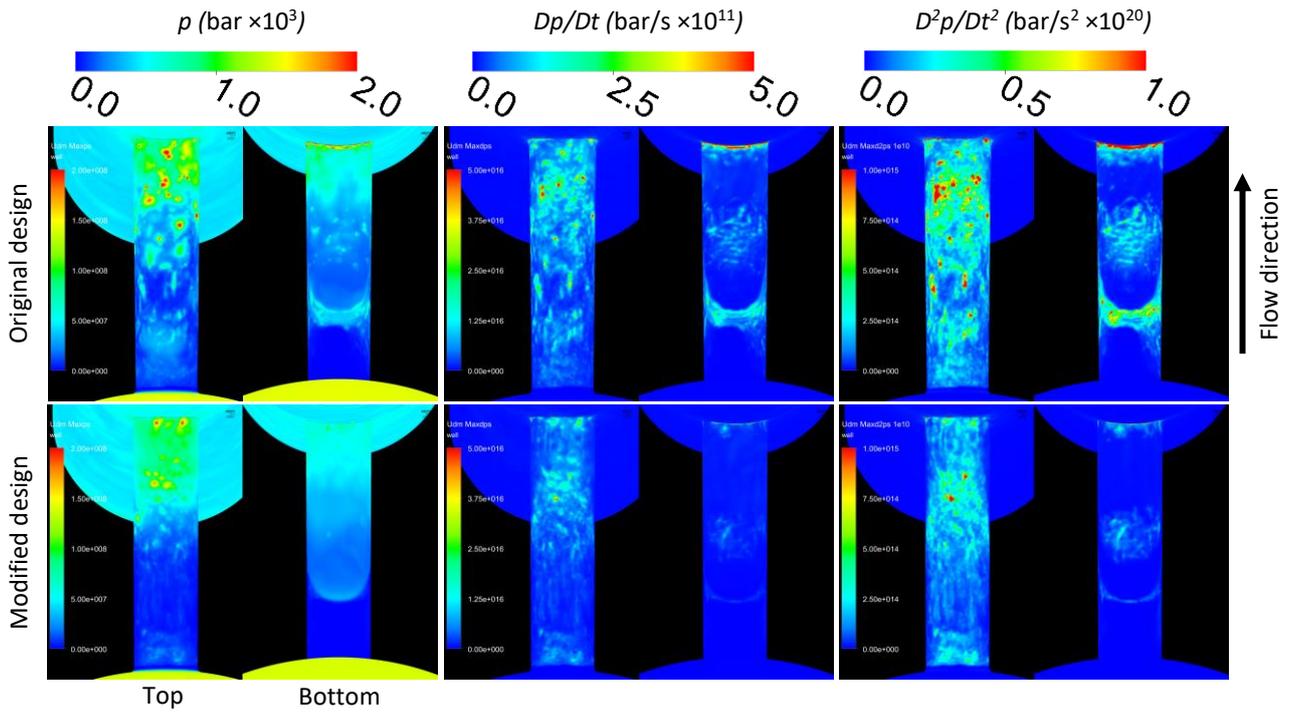
Fig. 5.11 – Peak values of variables related to *p* on the wall after 50 μs.

The differences between the original and modified designs becomes even more apparent when examining images of the peak values on the orifice. Fig. 5.11 shows the peak values on the wall of the orifice of p, Dp/Dt and D^2p/Dt^2 after 50μs. Similar maxima of p (Fig. 5.11, first column) occur towards the outlet of the orifice in both the original and modified design. Dp/Dt and D^2p/Dt^2 in the second and third columns of Fig. 5.11, respectively, show some improvement. The original prototype design shows many more maxima occurring, with almost no activity occurring on the bottom of the modified design. There are some similar maxima occurring on the top of the modified designs, but considerably fewer. Moreover, the peak values on the original design are importantly in the same regions of erosion as seen on the hardware. As such, all three of these potential ERIs show some usefulness as ERIs.

5.5.3.2 - Potential ERI – variables related to rate of pressure change

Dp/Dt has shown promise as an ERI in previous papers [66] [67]. To explore possible improvements to Dp/Dt different modifications were considered (Fig. 5.12). The first column shows the peak values of Dp/Dt on the wall of the orifice as a baseline. Comparing this to dp/dt maxima in the second column there are virtually no differences apparent. This indicates that the spatial component of the total derivative ($U \cdot \nabla p$) has almost no effect compared to the temporal part.
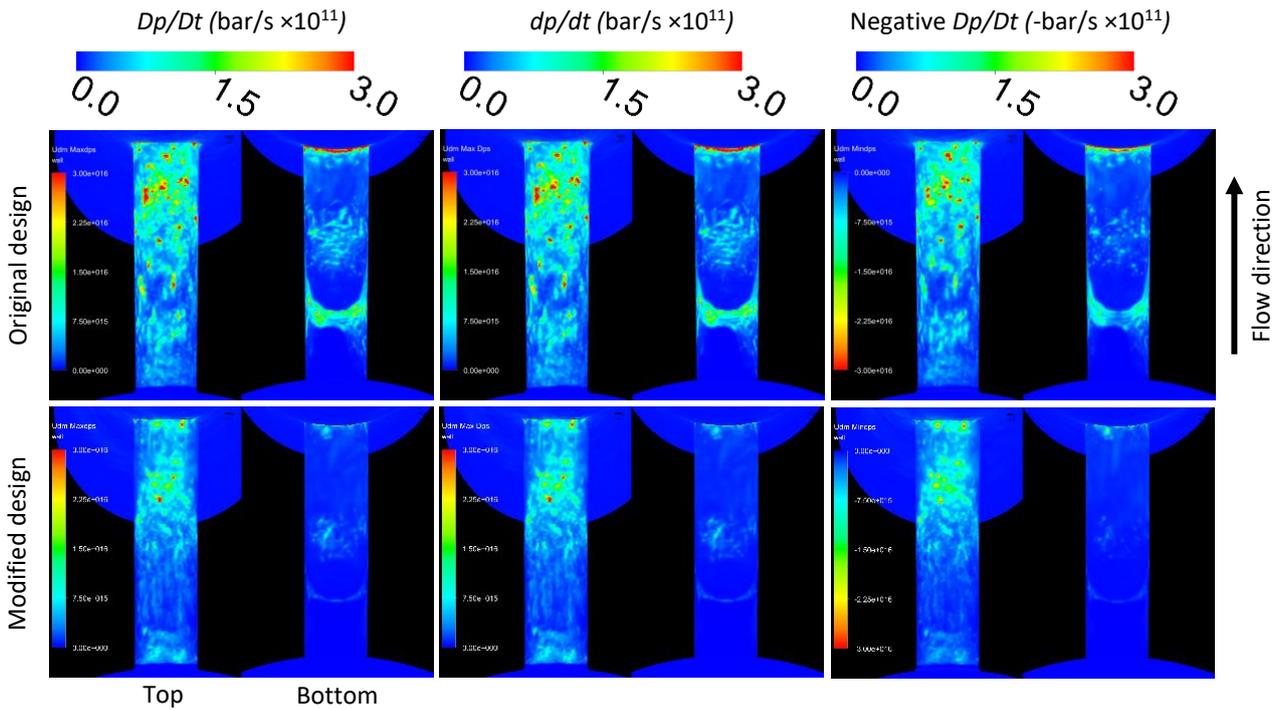
Fig. 5.12 – Peak values of variables related to *dp/dt* on the wall after 50 µs.

Comparing positive maxima of Dp/Dt in the first column to the negative values of Dp/Dt in the third column it is seen that the locations of the maxima are the same. Although, the negative maxima regions are slightly reduced in size. These negative values are likely due to the rebound of the vapour cavities after the initial collapse. The collapse and rebound events occur in such close succession that the negative values of Dp/Dt could also potentially be used as an erosion indicator. However, it does not provide any further benefit than the other values.

Other equations focusing on Dp/Dt were also examined, the material derivative of pressure divided by the cell volume ($(Dp/Dt)/V_{cell}$) and the material derivative of pressure squared ($(Dp/Dt)^2$), as seen in the first and second column of Fig. 5.13, respectively. The maxima of $(Dp/Dt)/V_{cell}$ demonstrates considerable difference between the two designs. The activity seen on the modified design is minimal when compared to the original design. However, an issue with this variable are the high values occurring at the exit of the orifice on both designs. This is likely due to the change in cell size near the orifice exit. The orifice exit had a sharp edge which could have been slightly rounded by a radius of a few micrometres to eliminate this issue. While this omission was unimportant for the general flow it had a noticeable effect on this proposed ERI. Even so, before the flow reaches the outlet of the orifice, there is good evidence $(Dp/Dt)/V_{cell}$ is a useful erosion risk indicator.
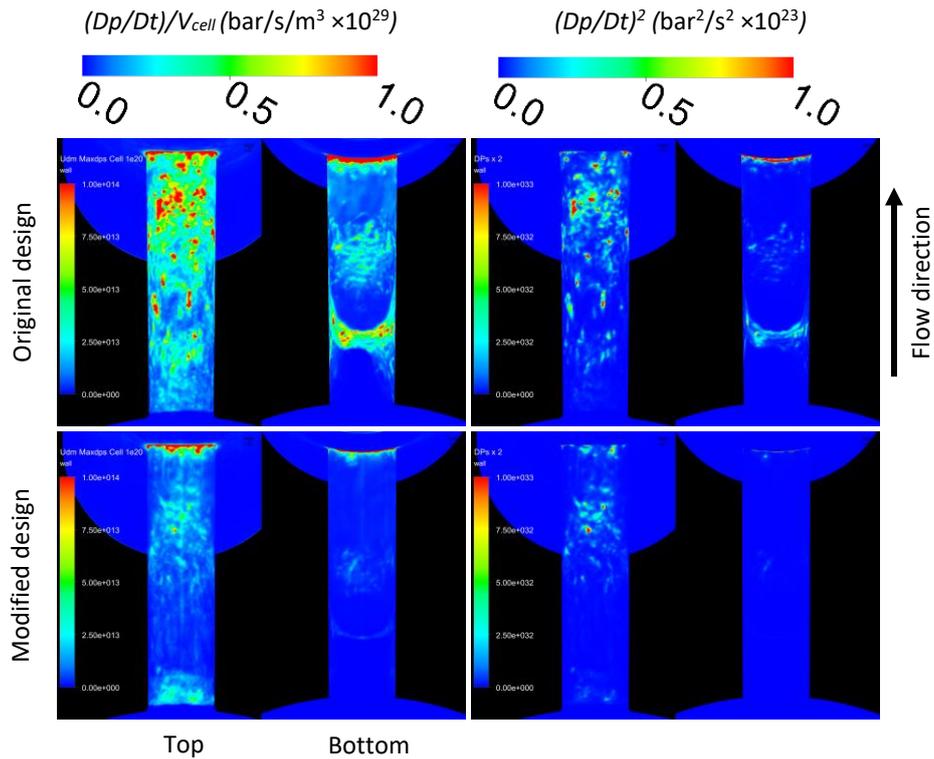
Fig. 5.13 – Peak values on the wall after 50 μs.

The usefulness of $(Dp/Dt)^2$ as an ERI was seen in the previous section on the Shoe and Guide. Here, maxima of $(Dp/Dt)^2$, in the second column of Fig. 5.13, also shows considerable contrast between the two designs. Again, there is minimal activity on the modified design. The activity on the original design is comparatively high and in a similar region as erosion seen on the hardware. As such, $(Dp/Dt)^2$ is considered a useful ERI.

5.5.3.3 - Potential ERI – variables related to density

Maximum values of the material derivative of density ($D\rho/Dt$) at each time-step were plotted over 70μs (Fig. 5.14). Like Dp/Dt there is much more activity on the original design than on the modified. Considering a cut-off of 4e11 kg/m³/s there are almost 10 times more spikes occurring with the original design than on the modified. This ratio is still maintained at a higher cut-off limit of 8e11 kg/m³/s. While the maxima of $D\rho/Dt$ does show a clear distinction between the two designs the location of the maxima must also be considered.

The maxima distribution of $D\rho/Dt$, $d\rho/dt$ and R_c over 50μs can be seen in Fig. 5.15. While there are noticeably more regions of high maxima on the original design for both the total and partial derivatives, they are not completely in the region of erosion as seen on hardware tests. The bottom side of the original design has maxima in the correct location while the top side shows maxima along most of the orifice length when it should only be in the downstream half. Furthermore, the modified design has maxima near the entrance of the orifice where there should not be any erosion risk. So, while $D\rho/Dt$ and $d\rho/dt$ may not show the exact

location at risk of erosion, they do show a clear difference between designs. They may be more accurate if they were coupled with another variable that could limit the maxima near the orifice entrance.

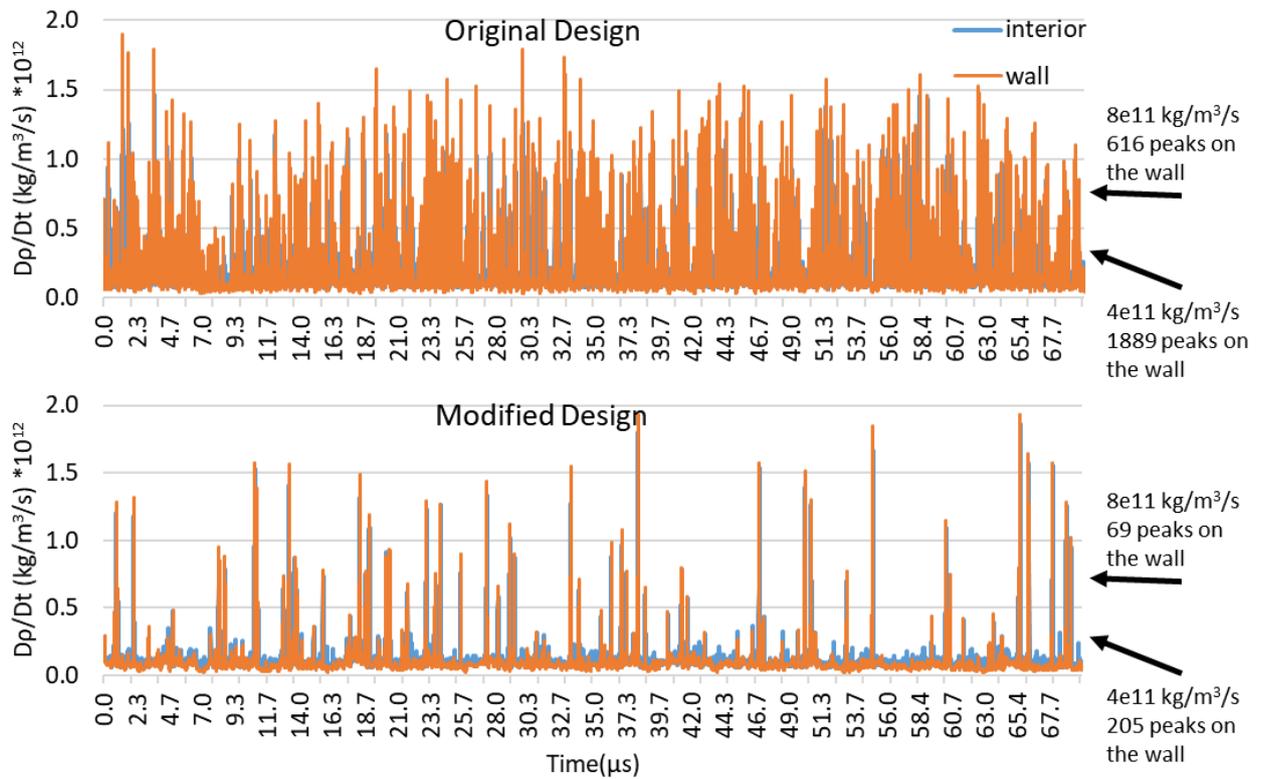Fig. 5.14 - Case 3 (DES with increased mass transfer rates). Maximum $D\rho/Dt$ in the entire domain (interior) and on any surface (wall) for 70 µs after initialization.
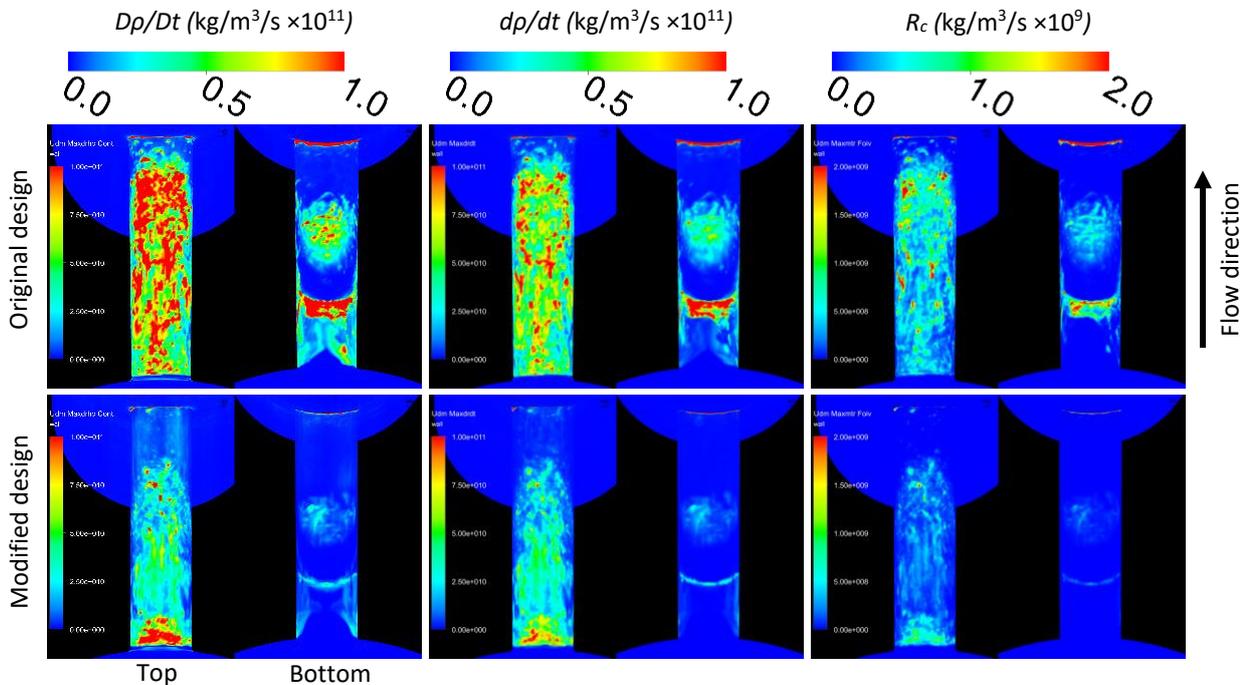
Fig. 5.15 – Peak values of variables related to density on the wall after 50 µs.

Maxima of R_c can be seen in the third column of Fig. 5.18. While there is some activity at the entrance of the modified design, there is a strong indication of erosion on the original design that correlates well to regions of erosion on the hardware. It has been seen that R_c may not be a useful ERI in the previous chapter for the Shoe and Guide. However, with the increased mass transfer rate implemented in this work, R_c appears to have some usefulness as an ERI.

5.5.3.4 - Potential ERI – variables related to liquid fraction

Potential ERI related to derivatives of liquid volume fraction (α_l) are shown in Fig. 5.16. The first column shows maxima of $D\alpha_l/Dt$ with a large region of high maxima on the modified design. While $D\alpha_l/Dt$ does not appear to be a viable ERI when comparing designs, $d\alpha_l/dt$, in the second column, could have potential. Peak values of $d\alpha_l/dt$ occur in larger regions on the original design than on the modified. However, both designs show some activity near the orifice inlet where there was no erosion. In the third column peak values of $d^2\alpha_l/dt^2$, which is part of P_a, are shown in the Control Orifice. While there is still some activity near the orifice inlet of both designs, the peaks on the original design are more pronounced than with $d\alpha_l/dt$ and there is less overall activity on the modified design. Even though peak values of $D\alpha_l/Dt$ may not be a valid erosion risk indicator, other derivatives, specifically $d^2\alpha_l/dt^2$, appear to be good ERIs.
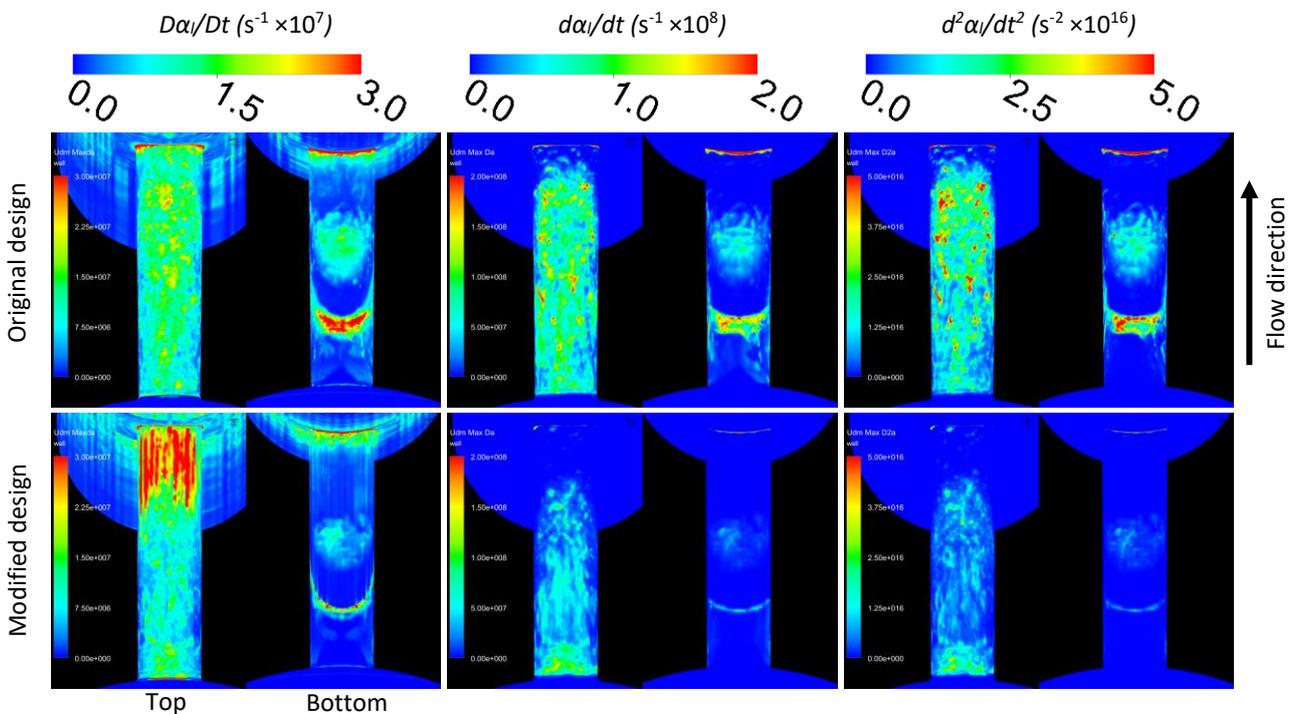
Fig. 5.16 – Peak values of variables related to liquid fraction on the wall after 50 μs.
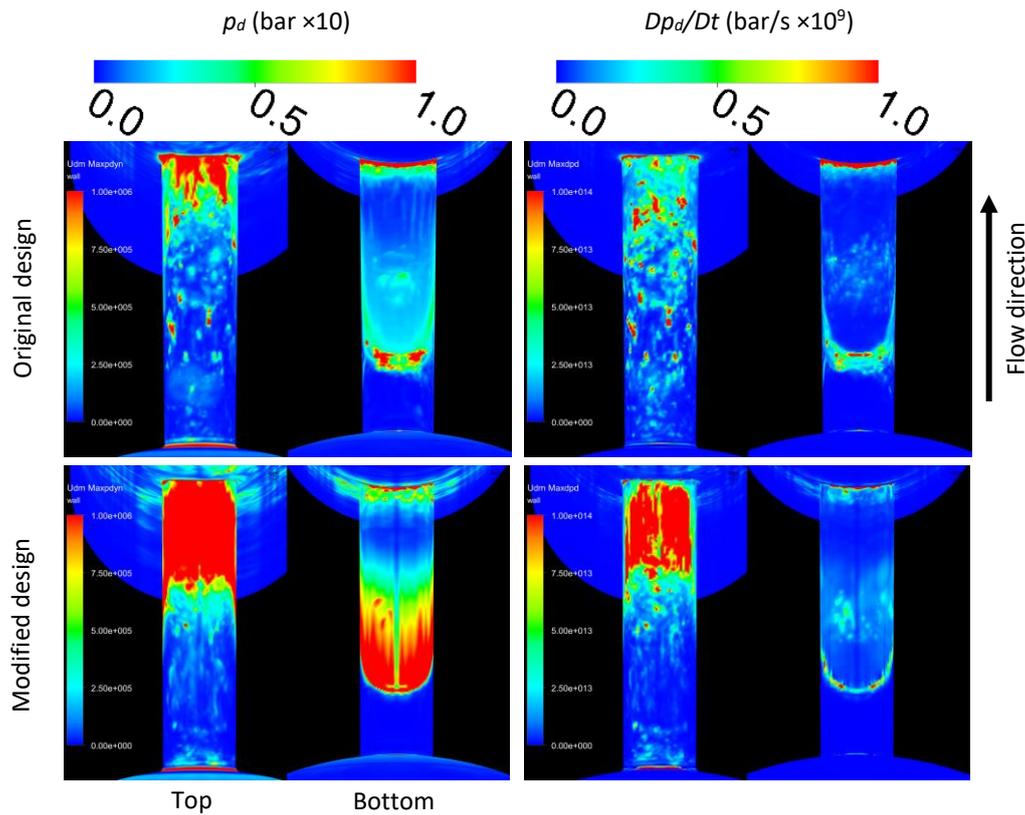
Fig. 5.17 – Peak values of variables related to p_d on the wall after 50 µs.

5.5.3.5 - Potential ERI – variables related to dynamic pressure

Peak values of dynamic pressure (p_d) and its derivative (Dp_d/Dt) were also considered as potential ERIs (Fig. 5.17). Both variables show maxima that correlate to the region of erosion on the original prototype hardware. However, the maxima on the modified design, that is erosion free, are higher. This is a perfect example of how necessary it is to include the modified prototype design that is free of erosion. This indicates that peak values of both, p_d and Dp_d/Dt, are not suitable as ERIs.

5.5.3.6 - Potential ERI – variables related to velocity

Dynamic pressure has a strong relation to velocity. To explore velocity in general as an ERI two other variables were investigated. They were $\nabla \cdot \boldsymbol{U}$ and acceleration ($D\boldsymbol{U}/Dt$), as seen in Fig. 5.18. The first column of Fig. 5.18 shows peak values of $\nabla \cdot \boldsymbol{U}$, which is part of a *PPD2* that showed promise as an ERI on the Shoe and Guide assembly. The potential ERI does show more activity on the original design with more maxima in the regions that saw erosion in the hardware. However, there is still considerable activity on the modified design. Furthermore, it is not as clear as *PPD2*, which is examined shortly. So, evidently the combination of variables plays an essential role for *PPD2*.
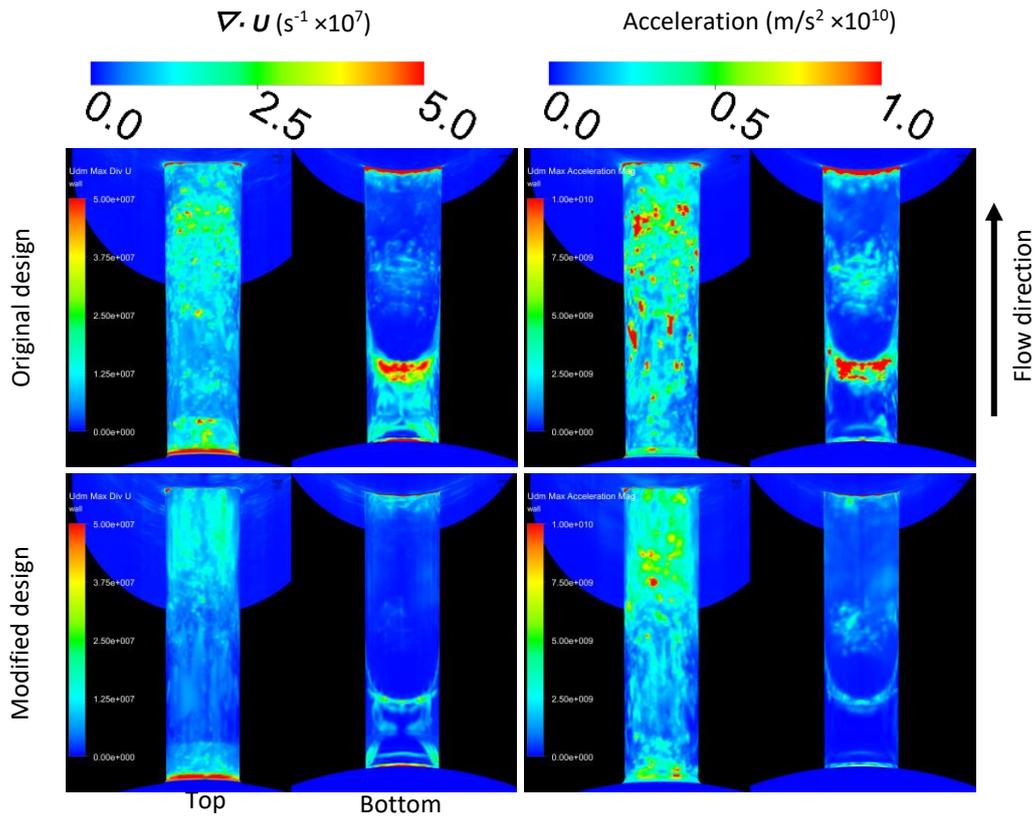
Fig. 5.18 – Peak values of $\nabla \cdot \boldsymbol{U}$ (first column) and acceleration (second column) on the wall after 50 μs.

In the second column of Fig. 5.18, maxima of acceleration are shown. On the bottom there is a clear difference in maxima, with the original design indicating a large region at risk of erosion. However, on the top of the orifice it is less clear, but there are still more regions in red on the original design. Although p_d and Dp_d/Dt did not show good correlation, the acceleration does have some potential as an ERI. Moreover, velocity terms cannot be wholly neglected as ERIs.

It should be noted here that even though the no-slip condition was applied to the walls a velocity component is still present. This is due to the cell centre being used for calculations in the contour plots, rather than the nodes on the wall. As such, there is a velocity component.

5.5.3.7 - Potential ERI – equations from the literature

Two potential ERIs related to vapour collapse energy are shown in Fig. 5.19. The first column shows maxima of *PPD2* with many more high peaks on the original design than the modified. The location of the maxima on the original design also correlate remarkably well to the regions of erosion from endurance tests. This is true for both the top and bottom of the Control Orifice. Therefore, *PPD2* is a useful ERI for this case.
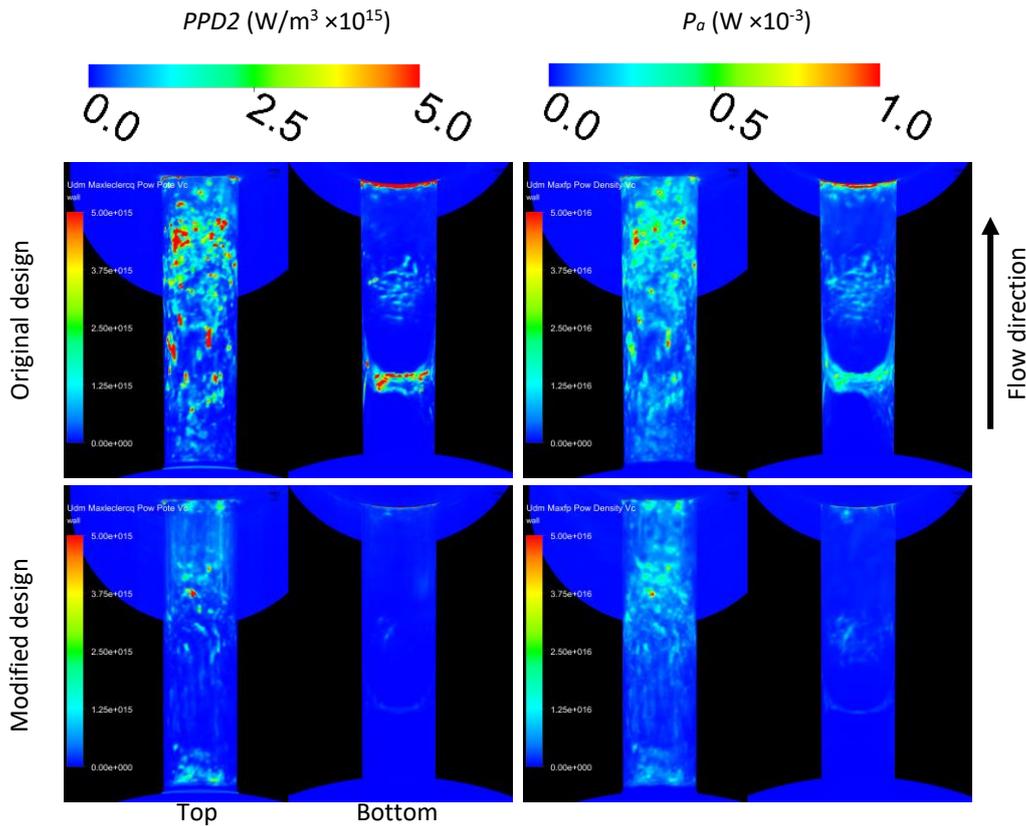
Fig. 5.19 – Peak values of *PPD2* (first column) and P_a (second column) on the wall after 50 μs.

Maxima of P_a are shown in the second column of Fig. 5.19. There is some distinction between the two designs, with more regions of maxima occurring on the original design, specifically in the regions of erosion as seen on hardware. However, there is some activity on the modified design as well. Therefore, P_a only shows some signs it is a useful ERI.

5.5.3.8 - Potential ERI – Summary

The qualitative assessments of the different ERIs tested are summarized in Table 5.4. ERIs that did not provide a clear difference between the prototype and modified design are labelled "poor." ERIs that provided the clearest difference between the two designs, and where the locations of the maxima correlated well with erosion seen on the hardware, are labelled "good." The other erosion indicators are labelled "some" as they provide only a limited indication of erosion potential.

Fig. 5.20 shows the five best ERIs ($(Dp/Dt)/V_{cell}$, $(Dp/Dt)^2$, R_c, $d^2\alpha/dt^2$, and *PPD2*) and how well the location of the maxima correlates with that of erosion on the hardware. These five indicators targeted the correct location and showed significantly higher peak values on the original design. Importantly, the same successful ERIs from the Shoe and Guide work were also successful here. It should also be noted that many of

the ERIs deemed unsuitable for the Shoe and Guide assembly work provided some usefulness in this work. This is likely due to these variables being sensitive to *R* values and turbulent levels. So, some of these potential ERIs may be more appropriate under different running conditions and should be investigated in future work.

It is now expected that these five ERIs, two of which are the same as the Shoe and Guide, can be applied to product design and development. As mentioned in the previous chapter, an existing production component that is free of erosion can be used as a control case to establish the distribution and intensity of the ERIs. The ERIs for any new or modified design can then be compared with the control case. A significant worsening of the ERI characteristics would indicate a region at risk of erosion. In this way, considerable time and cost would be saved during product development.

Table 5.4 – List of potential ERIs and their correlation level.

| Variable	Variable name	ERI correlation
p	Pressure (static pressure)	Some
Dp/Dt	Material derivative of pressure	Some
D^2p/Dt^2	Second material derivative of pressure	Some
dp/dt	Partial derivative of pressure	Some
$-Dp/Dt$	Negative values of the total derivative of pressure	Some
$(Dp/Dt)/V_{cell}$	Material derivative of pressure divided by the cell volume	Good
$(Dp/Dt)^2$	Material derivative of pressure, squared	Good
$D\rho/Dt$	Material derivative of density	Some
$d\rho/dt$	Partial derivative of density	Some
R_c	Condensing *R*	Good
$D\alpha_l/Dt$	Material derivative of liquid volume fraction	Poor
$d\alpha_l/dt$	Partial derivative of liquid volume fraction	Some
$d^2\alpha_l/dt^2$	Second partial derivative of liquid volume fraction	Good
p_d	Dynamic pressure	Poor
Dp_d/Dt	Material derivative of dynamic pressure	Poor
$\nabla \cdot (\boldsymbol{U})$	Divergence of velocity	Some
$D\boldsymbol{U}/Dt$	Acceleration	Some
$PPD2$	Second derivation of potential power density	Good
P_a	Acoustic pressure	Some
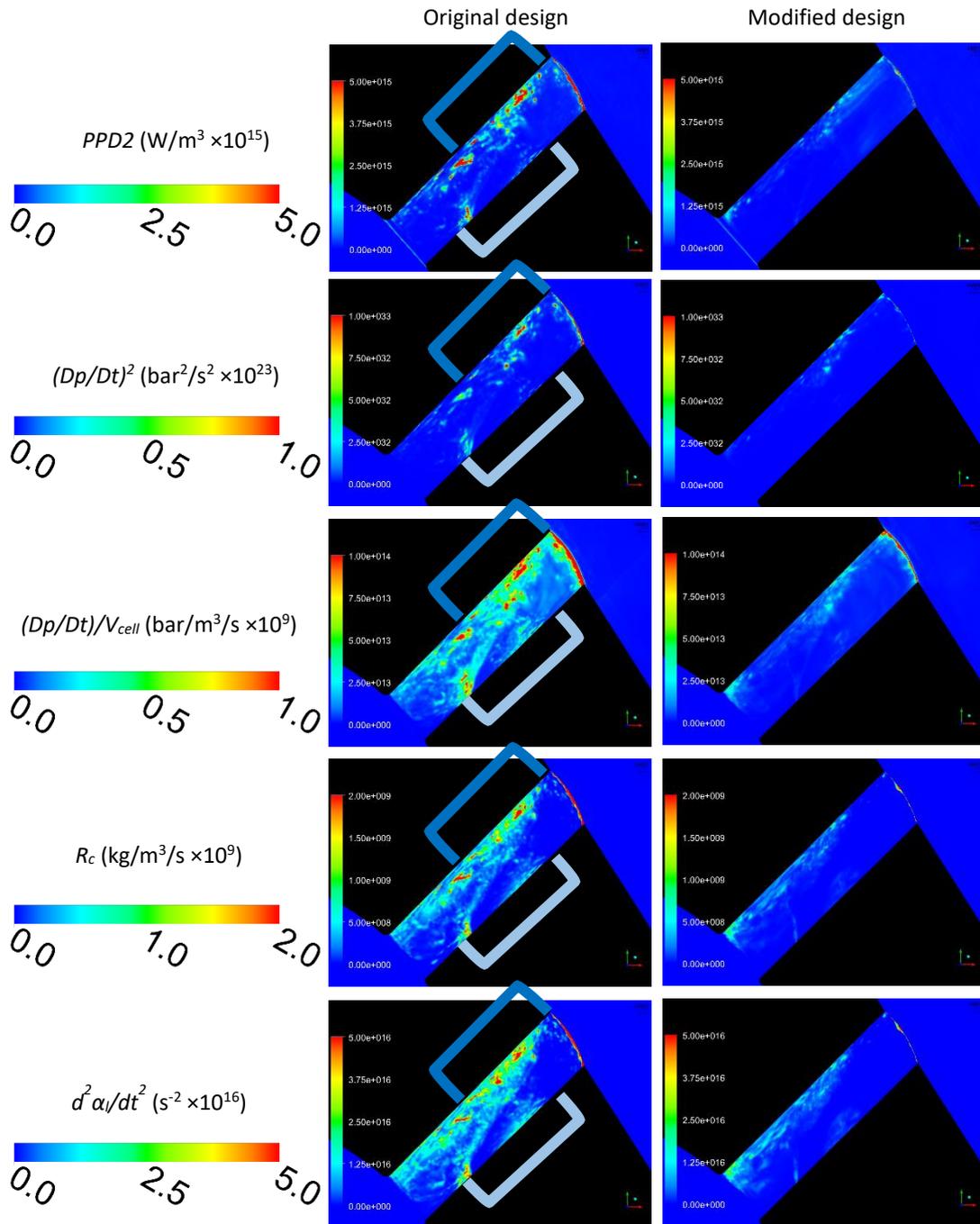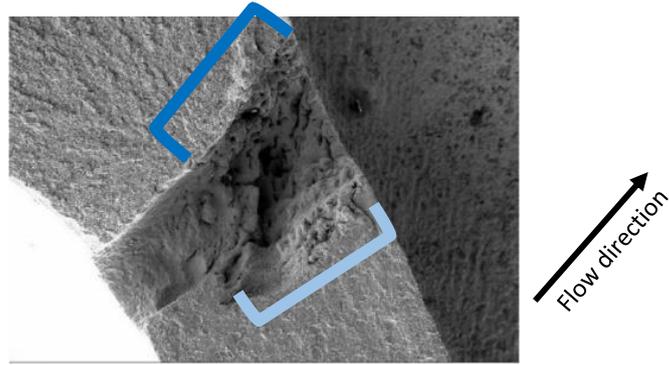
Fig. 5.20 – Interior side view of the best ERIs. Peak values on the wall after 50 μs.

5.6 - Conclusion

Currently, there is no accurate and consistent method to predict cavitation erosion. Cavitation occurring in the flow does not mean there will be erosion. Moreover, the amount of cavitation does not necessarily indicate the level of erosion risk. For this study two designs of a prototype Control Orifice from a diesel injector were investigated, one which experienced erosion, the original prototype design, and one that was erosion free, the modified prototype design. The two prototype designs were run under the same conditions and tested 19 potential ERIs in total. Some ERIs from the previous chapter and some new ones. The potential ERIs were evaluated in terms of the magnitude, location of maxima, and a select few in terms of frequency of peak occurrence.

For much of the CFD work performed in industry, the RANS technique for modelling turbulence is still the method of choice due to its acceptable time scale compared with LES/DES techniques. Hence, it is worth noting that the RANS model results (Case 1) showed a significant difference between the eroding and non-eroding designs. It is possible this difference was only case specific. However, it is interesting that the difference was in the region of erosion which suggests that backflow and recirculation, close to collapsing vapour structures, may result in an increased risk of erosion.

By employing an increased R with the DES turbulence model in case 3, more accurate and potentially useful results were produced, as opposed to case 2, which had default ZGB R values. For case 3, in terms of vapour and Q-criterion, the results demonstrated minimal visual differences between the original and modified prototype designs. However, in terms of the five best performing ERIs, there was considerable differences between the designs. This is especially true when considering the differences between the designs is in the order of microns. The location of the maxima for the top five ERIs correlated well with images of cavitation erosion from endurance tests on the original prototype hardware, while there were few maxima on the modified design. Furthermore, the frequency may be a useful component to support an ERI.

6 - Conclusions, impact and future work

6.1 - Summary of conclusions

This thesis presented novel results of CFD investigations of ERIs and cavitation shedding characteristics. Detailed conclusions have been provided in the previous chapters. The most important points are summarized below.

Two broad topics of cavitation modelling and understanding have been advanced in this work. The first topic concerns the prediction of cavitation erosion by means of ERIs. For the first time, a method to indicate erosion has been demonstrated which is robust across components of significantly different geometry and flow dynamics. The method has been validated to a level previously unseen by testing it on both eroding and non-eroding design levels. The non-eroding results provided an invaluable benchmark for the eroding results.

The second advancement concerns vapour shedding. From a new reprocessing of a large data set, insight was gained which revealed under which conditions the shedding mechanisms would occur. As a result, two shedding mechanisms were demonstrated in CFD simulations, one of which had not previously been achieved for the Venturi nozzle studied.

For the erosion prediction, the two fuel injection examples studied are real-world components from industry. This contrasts with much published research which uses specially made experimental test pieces of simplified design. Moreover, the pump Shoe and Guide assembly had a relatively low flow rate, and the injector Control Orifice had a relatively high flow rate. This meant that the cavitation erosion was produced with significantly different geometries, flow conditions and cavitation characteristics. Furthermore, each component type had two design levels, the original design, which eroded, and a modified design, which was free of erosion. This enabled the ERIs to be benchmarked against a control case, which is unique in this type of work and provided the deciding factor for many of the ERIs.

There were 19 potential ERIs tested in total, many of which were novel for this work. Two ERIs were found to identify erosion on both components. These were $(Dp/Dt)^2$ and *PPD2*. $(Dp/Dt)^2$ was newly derived for this research. An additional two of the successful five ERIs, that were only tested on the Control Orifice component, were also found to be useful and were likewise newly derived for this research. These were $d^2\alpha_l/dt^2$ and $(Dp/Dt)/V_{cell}$.

Regarding vapour shedding, both the re-entrant jet and the condensation shock shedding mechanisms were demonstrated in CFD simulations of a Venturi nozzle. Significantly, the re-entrant jet regime has not been

reliably shown before in simulations of this component. For the condensation shock regime, a higher degree of correlation with experimental results was achieved than in previous studies.

6.2 - Real world impact

The work presented here has identified useful ERIs for fuel injection components and has expanded the knowledge of cavitation characteristics. This knowledge can now be used to guide the design and development processes. This is especially true when designing systems like a high-pressure fuel line where erosion must be eradicated from all locations before a design reaches serial production. Currently, cavitation occurs in almost all high-pressure fuel line designs, whether they erode or not. Although CFD simulations are used extensively in this design process, there is no reliable method to indicate if a new or modified design will be subject to erosion. As such, the design process is guided by the designer's experience. Prototype components are manufactured and subjected to endurance and other experimental testing to check robustness to a range of factors, including possible cavitation erosion. If erosion occurs, design modifications are made, and the new prototype is again manufactured and tested. While designer's knowledge and past experiences are indeed valuable inputs, there is room for considerable improvement. The methods developed in this research will now be included in the development process, with the ERIs being used to identify regions likely to erode before prototype designs are manufactured and tested. In this way, the iterations of prototype manufacturing and testing will be reduced, bringing about a worthwhile reduction in the time and cost of design and development.

In addition to fuel injection components, eroding conditions of an expanding, liquid filled gap are also found in components like gear pumps, bearings and cylinder liners. Control orifices can be found in almost every engine and pump. The successful ERIs from this work may also be useful to the components in these different applications, among many others.

6.3 - Future work

To progress this work further there are several areas available to investigate. Along with further confirming the useful ERIs presented above, other areas of research include R, fluid properties at extreme pressures, the minimum values of ERIs that induce erosion and ERIs relationship with turbulence models.

A general question from this work concerns the mass transfer rate (R). Should R, either evaporating or condensing, be instantaneous or is it more appropriate that R has a range of values. In the ZGB cavitation model, the default condensing R is almost half of that for evaporating. It would be worthwhile to investigate

the rates of evaporation and condensation, which may bring about improvements in both RANS and LES modelling. Determining realistic *R* values would have a large effect on ERIs as well, as the rate of bubble collapse would be greatly affected.

The fluid properties are not available for Normafluid above 2500 bar. Considering collapsing vapour clouds in simulations, the calculated peak pressures and resulting fluid properties can only be assumed. Considering the automotive industry, the rail pressure is being increased to reduce emissions. To maintain the accuracy of simulations for these future designs realistic fluid property inputs are needed. As such, studying fluid properties up to 4000 or 5000 bar would be beneficial.

Finally, the ERIs discussed in the previous chapters could be further investigated. The absolute values needed to result in erosion are not known and should be explored. Furthermore, the ERIs relationship to turbulence models could be also be further explored. The results presented here have shown that using different models has some influence on the ERIs. Moreover, the Control Orifice results indicate that the number of times a value of an ERI goes above a certain threshold may also be significant in indicating erosion, as opposed to maximum values. This was clearly demonstrated as the two Control Orifice designs had similar peak pressure values, but the original design, which suffered from erosion, experienced over 10 times more pressure spikes over 2000 and 3000 bar. This was true for other potential ERIs as well. Additionally, the ERIs could be tested with different model types (pressure or density based), cavitation model (single fluid or mixture) or turbulence models. Investigations into the above topics would be the next steps in building from the work present here and furthering the important field of cavitation erosion research.

Publications

Journal publications:

M. Brunhart, C. Soteriou, C. Daveau, M. Gavaises, P. Koukouvinis, M. Winterbourn, "Cavitation erosion risk indicators for a thin gap within a diesel fuel pump," *Wear*, 442, 2019. DOI-10.1016/j.wear.2019.203024.IJER

Under review at time of submission - M. Brunhart, C. Soteriou, M. Gavaises, I. Karathanassis, P. Koukouvinis, S. Jahangir and C. Poelma, "Investigation of cavitation and vapor shedding mechanisms in a Venturi nozzle," *Physics of Fluids*, 2020

Conference publications:

M. Brunhart, C. Soteriou, C. Daveau, M. Gavaises, P. Koukouvinis and M. Winterbourn, "Investigation on the removal of the cavitation erosion risk in a prototype control orifice inside a diesel injector," in *Fuel Systems – Engines, IMechE*, London, 2018.

M. Brunhart, C. Soteriou, C. Daveau, M. Gavaises, P. Koukouvinis and M. Winterbourn, "Initial findings of an investigation on the removal of the cavitation erosion risk in a prototype control orifice inside a diesel injector," in *10th International Symposium on Cavitation*, Baltimore, 2018.

Appendix A

Procedures for running the different simulations

Venturi nozzle

- Hybrid initialization, coupled solver
- Run for at least 0.075s with a 5e-6s timestep and low URFs. Longer if convergence is unsteady
- Run for at least 0.05s with a 1e-6s timestep, depending on data and convergence, with higher URFs and 4 iterations/timestep (residuals ~1e-5, about 100 hour run time on 60 nodes, 20 nodes per core).

Shoe and Guide

- Standard initialization, piso solver
- For the fine mesh, run for 900µs with a 6.67e-8s timestep and 25 iterations/timestep (residuals ~1e-5, about 120 hours run time on 60 nodes, 12 nodes per core). Time for initialization was already included in the face movement profile.

Control orifice (SPO)

- Hybrid initialization, simple solver
- Run RANS until converged
- Switch to DES and run for 10µs with a 2e-9s timestep and 27 iterations/timestep to initialize (residuals ~1e-8, about 70 hour run time on 96 nodes, 12 nodes per core). Continue running to collect data.

Appendix B

The second material derivative was derived and is defined as:

$$\frac{D^2\varphi}{Dt^2} = \frac{\partial^2\varphi}{\partial t^2} + \frac{\partial\varphi}{\partial x}\left(\frac{\partial u}{\partial t} + \boldsymbol{U}\cdot\nabla u\right) + \frac{\partial\varphi}{\partial y}\left(\frac{\partial v}{\partial t} + \boldsymbol{U}\cdot\nabla v\right) + \frac{\partial\varphi}{\partial z}\left(\frac{\partial w}{\partial t} + \boldsymbol{U}\cdot\nabla w\right)$$

$$+ 2\left(uv\frac{\partial^2\varphi}{\partial x\partial y} + vw\frac{\partial^2\varphi}{\partial y\partial z} + uw\frac{\partial^2\varphi}{\partial x\partial z}\right) + 3\left(u^2\frac{\partial^2\varphi}{\partial x^2} + v^2\frac{\partial^2\varphi}{\partial y^2} + w^2\frac{\partial^2\varphi}{\partial z^2}\right)$$

where φ is the variable of choice and u, v and w are the respective velocity components. This assumes $\partial x\partial y$ and $\partial y\partial x$, and similar, while mathematically interchangeable, are also computationally the same.

Appendix C

Initial mesh study concerning the ERIs on the Shoe and Guide

Important factors to consider that could affect potential ERIs is the density of the mesh and the time-step size. These factors were briefly explored for some potential ERIs applied to the thin fluid filled gap in the Shoe and Guide assembly. Maxima of pressure (Fig. C.1), *Dp/Dt* (Fig. C.2) and *PPD2* (Fig. C.3) are shown. The original prototype design had 3.6 million cells for the fine mesh and 6.8 thousand cells for the coarse mesh. The modified prototype design had 5.7 million cells for the fine mesh and 200 thousand for the coarse mesh (refinement was needed at the groove to gap transition). The time-step used with the fine mesh was 6.67e-8s and 6.67e-7s for the coarse mesh.

The flow rate and other flow characteristics were essentially the same between these simulations. However, some peak values of potential ERIs did vary. The peak pressure appears to be relatively independent of the mesh and time-step (Fig. C.1), the absolute maxima of *Dp/Dt* and *PPD2* are different. Importantly though, the relative differences are maintained between the original and modified prototype designs, with higher values occurring on the original design. This should be further investigated in future work.

Fig. C.1 - Images of maximum *p* values reached throughout the simulation on the mid-plane with different mesh densities and time-steps.

Dp/Dt (0 to 1 Pa/s ×10^{14})

Coarse mesh   Fine mesh
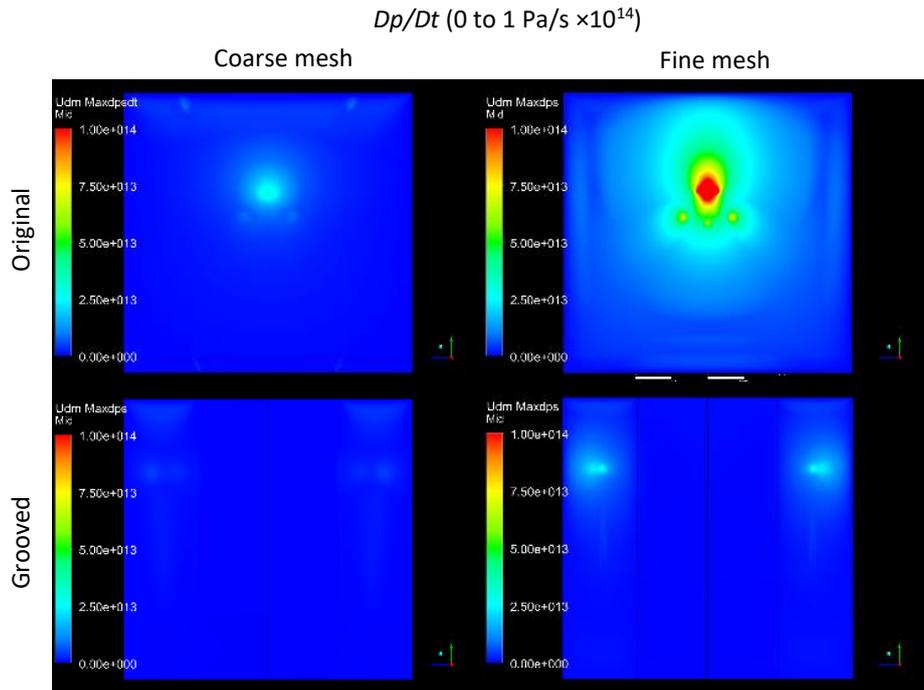
Fig. C.2 - Images of maximum Dp/Dt values reached throughout the simulation on the mid-plane with different mesh densities and time-steps.

$PPD2$ (0 to 3 W/m^3 ×10^{13})

Coarse mesh   Fine mesh
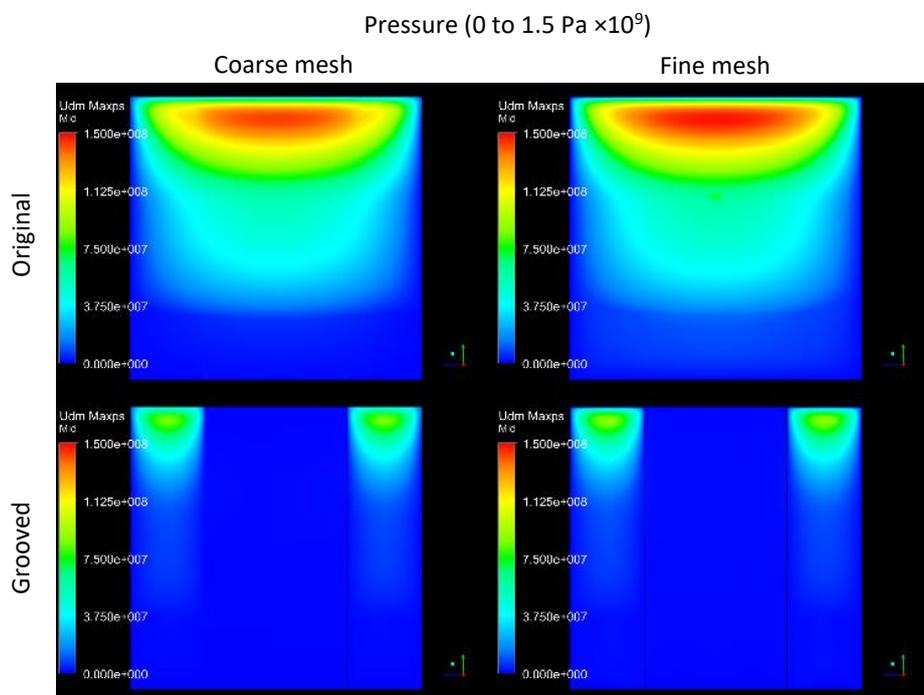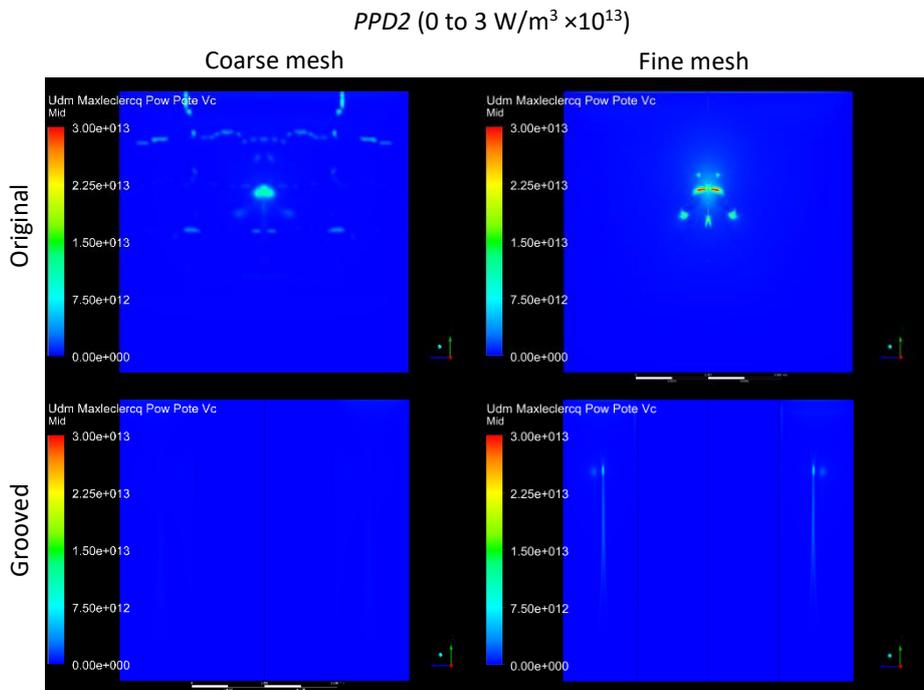

Fig. C.3 - Images of maximum $PPD2$ values reached throughout the simulation on the mid-plane with different mesh densities and time-steps.

Appendix D

Comparison of peak values of potential ERIs on the guide face, mid-plane and shoe face (Fig. D.1).

The ERI maxima images shown chapter 4 concerning the Shoe and Guide were mainly on the mid-plane between the shoe and the guide. The ERIs directly on the faces of the shoe and the guide were also investigated but did not change the assessments for 9 out of the 10 ERIs. Acoustic power (P_a) was the one exception, as shown below.
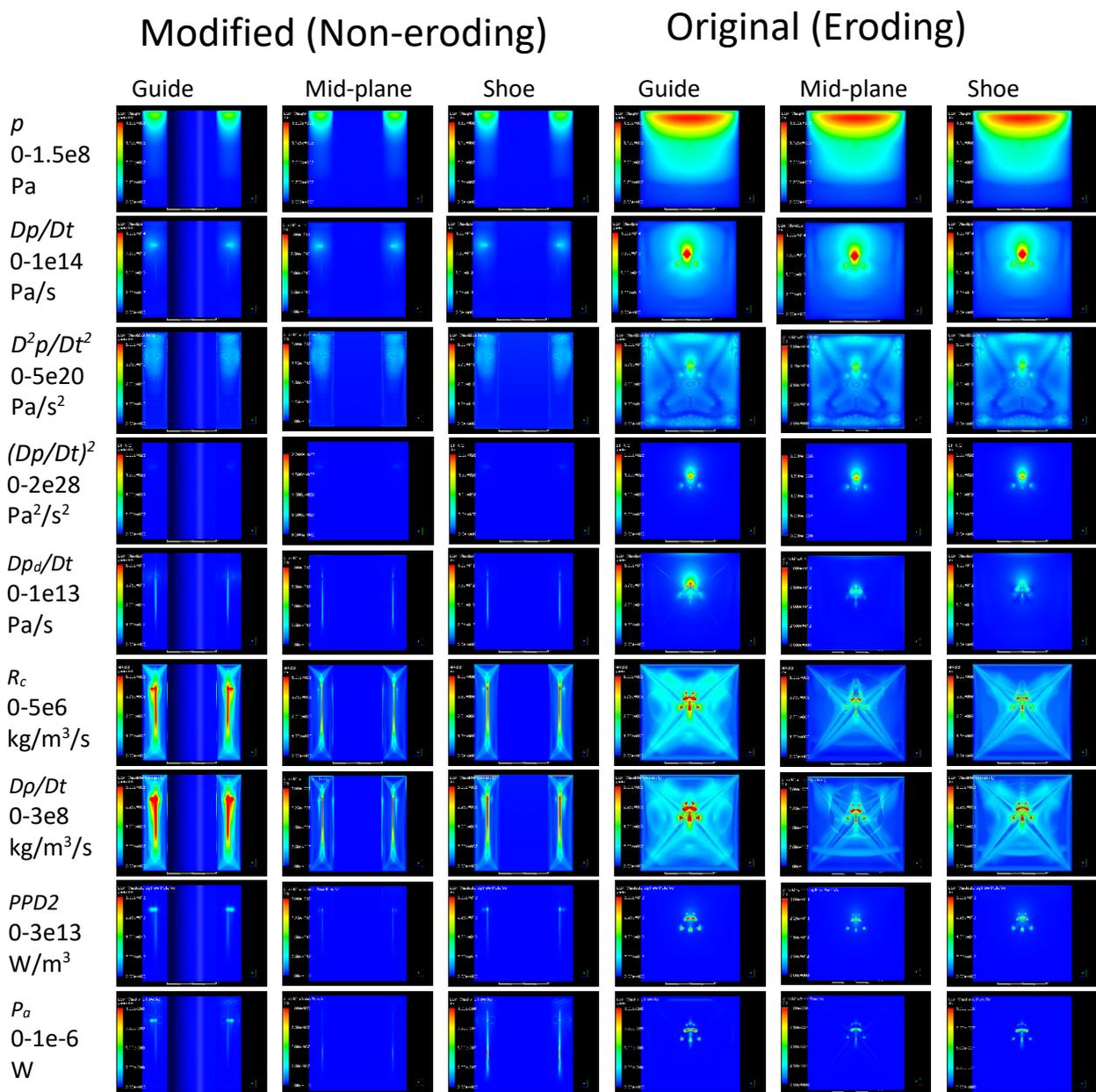
Fig. D.1 – Comparison of the maxima values of potential ERIs on different planes.

Appendix E

An FFT analysis was conducted with the SPO case 3 data (DES simulation with an increased rate of mass transfer). Peak values of pressure and *Dp/Dt* occurring on the wall (Fig. E.1, Fig. E.2) were examined and showed no obvious dominating frequencies.
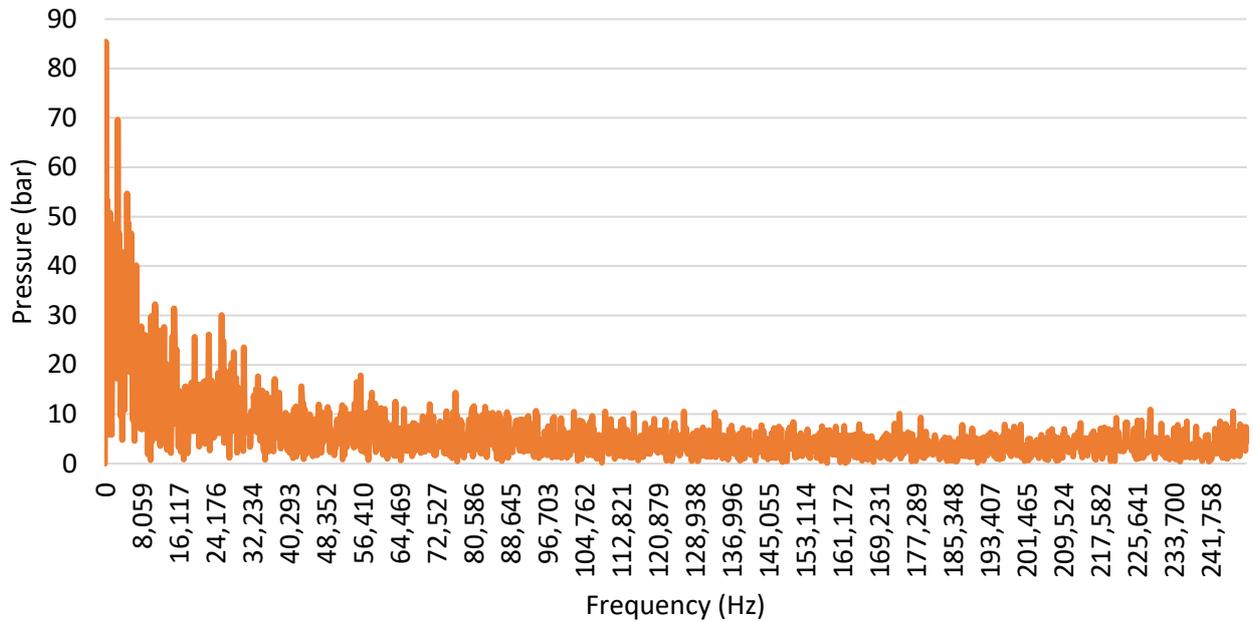
Fig. E.1 – FFT of the maximum pressure occurring on the wall of the SPO in case 3.
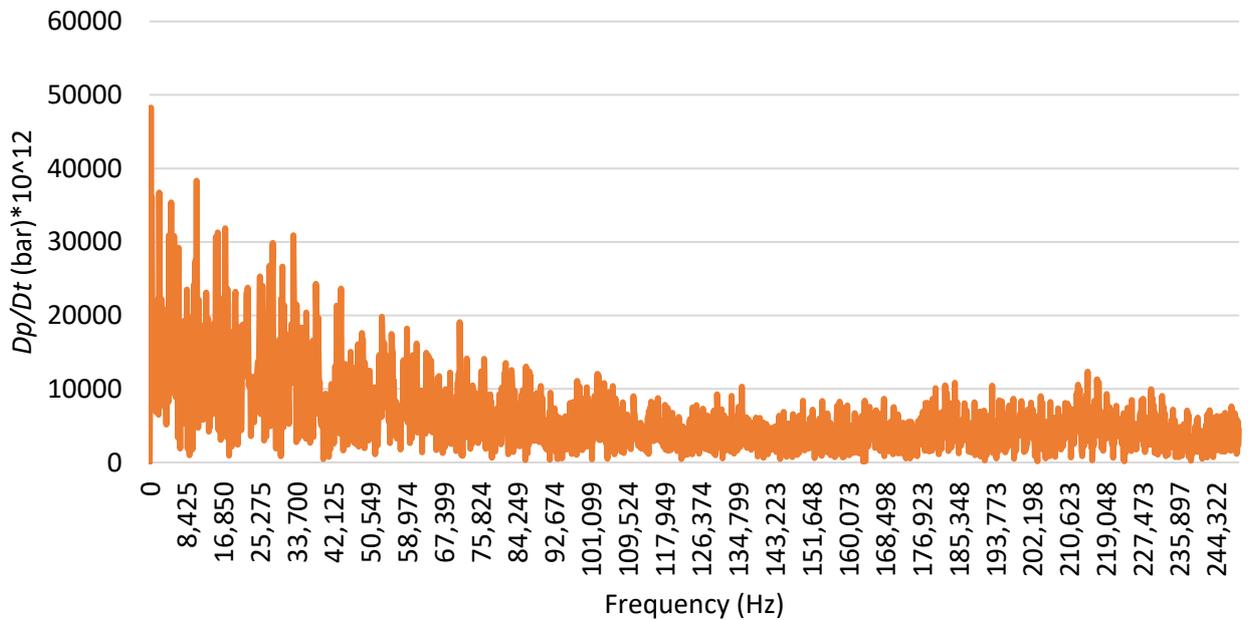
Fig. E.2 – FFT of the maximum *Dp/Dt* occurring on the wall of the SPO in case 3.

References

[1] ExxonMobil, "2018 Outlook for Energy: A View to 2040," ExxonMobil, 2018.

[2] N. Keeler, D. Lane, D. Mellors and S. Tullis, "Beyond Euro VI – An FIE System and Combustion Optimisation Approach," *SIA,* 2015.

[3] J. Franc, M. Riondet, A. Karimi and G. Chahine, "Material and velocity effects on cavitation erosion pitting," *Wear,* vol. 274, 2012.

[4] M. Euler, "Théorie plus complète des machines qui sont mises en movement par la réaction de l'eau," in *L'Académie Royale des Science et Belles Lettres*, Berlin, 1756.

[5] S. Barnaby and J. Thornycroft, "Torpedo boat destroyers," *Proc. Inst. Civ. Engers.,* vol. 122, no. 57, 1895.

[6] J.-P. Franc and J.-M. Michel, Fundementals of Cavitation, New York: Kluwer Academic Publishers, 2005.

[7] C. Brennen, Cavitation and Bubble Dynamics, Oxford University Press, 1995.

[8] Rayleigh, "On the pressure development in a liquid during the collapse of a spherical cavity," *Philosophical Magazine,* vol. 34, no. 200, pp. 94-98, 1917.

[9] E. Ghahramani, M. H. Arabnejad and R. E. Benson, "A comparative study between numerical methods in simulation of cavitating bubbles," *Int. J. of Multi. Flow,* vol. 000, pp. 339-359, 2018.

[10] P. Koukouvinis, M. Gavaises, A. Georgoulas and M. Marengo, "Compressible simulations of bubble dynamics with central upwind schemes," *Int. J. of CFD,* vol. 30, no. 2, 2016.

[11] N. Kyriazis, P. Koukouvinis and M. Gavaises, "Numerical investigation of bubble dynamics using tabulated data," *Int. J. of Multiphase Flow,* vol. 93, pp. 158-177, 2017.

[12] M. Plesset, "The dynamics of cavitation bubbles," *Journal of Applied Mechanics,* vol. 16, pp. 277-282, 1949.

[13] W. Moss, "Understanding the periodic driving pressure in the Rayleigh-Plesset equation," *Journal of Acoustical Society of America,* vol. 101, no. 2, pp. 1187-1190, 1997.

[14] J. R. Blake, G. S. Keen, R. P. Tong and M. Wilson, "Acoustic cavitation: the fluid dynamics of non-spherical bubbles," *Philosophical Transactions of the Royal Society of London Series A-Mathematical Physical and ENgineering Sciences,* vol. 357, no. 1751, pp. 251-267, 1999.

[15] A. Kubota, H. Kato and H. Yamaguchi, "A new modelling of cavitating flows - a numerical study of unsteady cavitation on a hydrodfoil section," *Journal of Fluid Mechanics,* vol. 240, pp. 59-96, 1992.

[16] Y. Chen and S. Heister, "Two-phase modeling of cavitated flows," *Computers and FLuids,* vol. 24, no. 7, pp. 799-809, 1995.

[17] Y. Delannoy and J. Kueny, "Two phase flow approach in unsteady cavitation modelling," in *Cavitation and Multiphase Forum*, ASME FED, 1990.

[18] D. Schmidt, C. Rutland and M. Corradini, "A numerical study of cavitation flow through various nozzle shapes," *SAE paper 971597,* 1997.

[19] D. Schmidt, C. Rutland and M. Corradini, "A fully compressible two-dimensional model of small high-speed cavitating nozzles," *Atomization and Sprays,* vol. 9, no. 3, pp. 255-276, 1999.

[20] G. Wallis, One-dimensional Two-phase Flow, McGraw-Hill, 1969.

[21] J. Reboud, B. Stutz and O. Coutier-Delgosha, "Two-phase flow structures of cavitation; experiment and modelling of unsteady effects," in *Third Internation Symposium on Cavitation*, Grenoble, 1998.

[22] O. Coutier-Delgosha, J. Reboud and Y. Delannoy, "Numerical simulation of the unsteady behaviour of cavitating flows," *International Journal for Numerical Methods in Fluids,* vol. 42, 2003.

[23] J. Sauer and G. Schnerr, "Unsteady cavitating flow - A new cavitation model based on a modified front capturing method and bubble dynamics," in *ASME Fluid Engineering Division Summer Meeting*, Boston, 2000.

[24] A. Singhal, M. Athavale, H. Li and Y. Jiang, "Mathematical basis and validation of the full cavitation model," New Orleans, 2001.

[25] P. J. Zwart, A. G. Gerber and T. Belamri, "A Two-Phase Flow Model for Predicting Cavitation Dynamics," in *5th international Conference on Multiphase Flow*, Yokohama, Japan, 2004.

[26] W. Yuan, J. Sauer and G. Schnerr, "Modelling and computation of unsteady cavitation flows in injection nozzles," in *1st International Colloquium on Microhydrodynamics*, Paris, 2000.

[27] H. Liu, J. Wang, Y. Wang, H. Zhang and Z. Huang, "Influence of the empirical coefficients of cavitation model on predicitng flow on the centrifugal pump," *Int. J. Nav. Archit Ocean Eng.,* vol. 6, pp. 119-131, 2014.

[28] B. Befrui, P. Spiekermann, M. Shost and M. Lai, "VoF-LES Studies of GDi Multi-Hole Nozzle Plume Primary Breakup and Comparison with Imaging Data," in *ILASS Europe Conference on Liquid Atomization and Spray Systems*, Chania, 2013.

[29] R. Bensow, "Simulation of the unsteady cavitation on the Delft Twist11 foil using RANS, DES and LES," in *Second International Symposium on Marine Propulsors*, Hamburg, 2011.

[30] C. Egerer, S. Hickel, S. Schmidt and N. Adams, "Analysis of turbulent cavitating flow in a micro-channel," in *SHF Conference on Hydraulic Machines and Cavitatio*, Grenoble, 2013.

[31] S. Salim, K. Ong and S. Cheah, "Comparison of RANS, URANS and LES in the Prediction of Airflow and Pollutant Dispersion," in *WCECS*, San Francisco, USA, 2011.

[32] D. Bush, C. Soteriou, M. Winterbourn and C. Daveau, "Investigating hydraulic control components in high performance injectors," in *IMechE Fuel Injection*, London, 2015.

[33] M. Gavaises, D. Papouluas, A. Andritotis and E. Giannadakis, "Link between cavitation development and erosion damage in diesel injector nozzles," *SAE Technical Paper 2007-01-0246,* 2007.

[34] P. Koukouvinis, M. Gavaises, J. Li and L. Wang, "Large eddy simulaiton of diesel injector including cavitation effects and correlation to erosion damage," *Fuel,* vol. 175, pp. 26-39, 2016.

[35] P. R. Spalart, W.-H. Jou, M. Strelets and S. R. Allmaras, "Comments on the Feasibility of LES for Wings and on a Hybrid RANS/LES Approach," in *1st AFOSR International Conference on DNS/LES*, 1997.

[36] P. R. Spalart, S. Deck, S. M. L, K. D. Squires, M. K. Strelets and A. Travin, "A new version of detached-eddy simulation, resistant to ambigous grid densities," in *Theoretical Computational Fluid Dynamics*, 2006.

[37] M. L. Shur, P. R. Spalart, M. K. Strelets and A. K. Travin, "A hybrid RANS-LES approach with delayed-DES and wall-modelled LES capabilities," *International Journal of Heat and Fluid Flow,* vol. 29, no. 6, pp. 1638-1649, 2008.

[38] B. Befrui, G. Corbinelli, M. D'Onofrio and D. Varble, "GDI Multi-Hole Injector Internal Flow and Spray Analysis," in *SAE International 2011-01-1211*, 2011.

[39] P. Koukouvinis, H. Naseri and M. Gavaises, "Performance of turbulence and cavitation models in prediction of incipient and developed cavitation," *Int. J. of Engine Research,* vol. 18, 2016.

[40] P. Koukouvinis, N. Mitroglou, M. Gavaises, M. Lorenzi and M. Santini, "Quantitative predictions of cavitation presence and erosion-prone locations in a high-pressure cavitation test rig," *J. Fluid Mech.,* vol. 819, pp. 21-57, 2017.

[41] M. Gavaises, F. Villa, P. Koukouvinis, M. Marengo and J. Franc, "Visualisation and LES simulation of cavitation cloud formation and collapse in an axisymmetric geometry," *International Journal of Multiphase Flow,* vol. 68, pp. 14-26, 2015.

[42] W. Edelbauer, J. Strucl and A. Morozov, "Large eddy simulation of cavitating throttle flows," in *Advances in Hydroinformatics, part III*, Springer, 2014, pp. 501-517.

[43] C. Soteriou, R. Andrews and M. Smith, "Further studies of cavitation and atomization in diesel injection," *SAE Technical Paper 1999-01-1486,* 1999.

[44] C. Soteriou, M. Smith and R. Andrews, "Diesel injection - laser light sheet illumination of the development of cavitation in orifices," in *IMechE C529/018/98*, 1998.

[45] J. Wloka, S. Pflaum and G. Wachtmeister, "Potential and challenges of a 3000 bar common-rail injection system considering engine behavior and emission level," *SAE Int. J. Engines ,* vol. 3, pp. 801-813, 2010.

[46] G. Boccardo, F. Millo, A. Piano, L. Arnone, S. Manelli, S. Fagg, P. Gatti, O. Erik, D. Queck and J. Weber, "Experimental investigation on a 3000 bar fuel injection system for a SCR- free non-road diesel engine," *Fuel,* vol. 243, pp. 342-351, 2019.

[47] M. Choraęzewski, F. Dergal, T. Sawaya, I. Mokbel, J. Grolier and J. Jose, "Thermophysical properties of Normafluid (ISO 4113) over wide pressure and temperature ranges," *Fuel,* vol. 105, pp. 440-450, 2013.

[48] T. Okada, Y. Iwai and K. Awazu, "A study of cavitation bubble collapse presssures and erosion part 1: A method for measuring of collapse pressures," *Wear,* vol. 133, no. 2, pp. 219-232, 1989.

[49] W. Nour, U. Dulias, J. Schneider and K. Gahr, "The effects of surface finish and cavitating liquid on the cavitation erosion of alumina and silicon carbide ceramics," *Ceramics,* vol. 51, no. 1, pp. 30-37, 2007.

[50] N. Naseri, "Modelling of nozzle cavitation in newtonian and viscoelastic fluids," City, University of London, PhD thesis, 2019.

[51] Y. Iwai and S. Li, "Cavitation erosion in waters having different surface tensions," *Wear,* vol. 254, pp. 1-9, 2003.

[52] Z. Zhang and H. Zhang, "Surface tension effects on the behavior of a cavity growing, collapsing, and rebounding near a rigid wall," *Physical Review E,* vol. 70, 2004.

[53] X. Liu, J. He, J. Lu and X. Ni, "Effect of surface tension on a liquid-jet produced by the collapse of a laser-induced bubble against a rigid boundary," *Optics and Laser Technology,* vol. 41, pp. 21-24, 2009.

[54] A. Theodorakakos, M. Gavaises, R. Pearson and M. Gold, "Influence of fuel on cavitation inception and further development in diesel fuel injectors," *IMECHE,* 2014.

[55] H. Temperley and D. Trevena, "Metastability of the liquid-vapor transition and related effects," *J. of Stat. Phys.,* vol. 77, no. 2, pp. 501-508, 1994.

[56] W. McNamara III, Y. Didenko and K. Suslick, "Sonoluminescence temperatures during multi-bubble cavitation," *Nature,* vol. 401, 1999.

[57] B. Budich, S. Schmidt and N. Adams, "Numerical simulation and analysis of condensation shocks in cavitating flow," *J. Fluid Mech.,* vol. 838, pp. 759-813, 2018.

[58] G. Strotos, P. Koukouvinis, A. Theodorakakos, M. Gavaises and G. Bergeles, "Transient heating effects in high pressure Diesel injector nozzles," *International Journal of Heat and Fluid Flow,* vol. 51, pp. 257-267, 2015.

[59] E. Young, Cavitation, McGraw-Hill Book Co., 1989.

[60] S. Joshi, J. Franc, G. Ghiglitti and M. Fivel, "SPH modelling of a cavitaiton bubble collapse near an elasto-visco plastic material," *Journal of the Mechanics and Physics of Solids,* vol. 125, pp. 420-439, 2019.

[61] S. Roy, J. Franc, C. Pellone and M. Fivel, "Determination of cavitaiton load spectra - part 1: static finite element approach," *Wear,* vol. 344, pp. 110-119, 2015.

[62] I. Jones and D. Edwards, "An experimental study of forces generated by the collapse of transient cavities in water," *J. Fluid Mech.,* vol. 596, 1960.

[63] E. Cadoni and D. Forni, "Strain rate effects on reinforcing steels in tension," *EPJ Web of Conferences,* vol. 94, 2015.

[64] O. Vinogradova, N. Bunkin, N. Churaev, O. Kiseleva, A. Lobeyev and B. Ninham, "Submicrocavity structure of water between hydrophobic and hydrophilic walls as revealed by optical cavitation," *Journal of Colloid and Interface Science,* vol. 173, no. 2, pp. 443-447, 1995.

[65] A. Philipp and W. Lauterborn, "Cavitation erosion by single laser-produced bubbles," *J. Flui Mech.,* vol. 361, pp. 75-116, 1998.

[66] N. Soda and Y. Tanaka, "Cavitaiton erosion of a flat surface near a rotating shaft," *Wear,* vol. 74, pp. 275-286, 1982.

[67] P. Koukouvinis, G. Bergeles and M. Gavaises, "A new methodology for estimating cavitation erosion: application on a high speed cavitation test," in *11th World Congress on Computational Mechanics*, Barcelona, Spain, 2014.

[68] P. Koukouvinis, G. Bergeles and M. Gavaises, "A cavitation aggressiveness index within the Reynolds averaged Navier Stokes methodology for cavitating flows," *Journal of Hydrodynamics,* vol. 27, no. 4, 2015.

[69] P. Koukouvinis, G. Bergeles, j. Li, L. Wang, A. Theodorakakos and M. Gavaises, "Simulation of cavitation inside diesel injectors, including erosion modelling," in *IMeche Fuel Systems*, 2016.

[70] Y. Wang and C. Brennen, "Numeriacl computation of shock waves in a spherical cloud of cavitation bubbles," *Journal of Fluids Engineering,* vol. 121, no. 4, pp. 872-880, 1999.

[71] R. Fortes-Patella, J. L. Reboud and L. Briancon-Marjollet, "A phenomenological and numerical model for scaling the flow aggressiveness in cavitation erosion," in *Cavitation Erosion Workshop*, Val de Reuil, 2004.

[72] R. Fortes-Patella, A. Archer and C. Flageul, "Numerical and experimental investigations on cavitation erosion," *IOP Conference Series: Earth and Environmental Science,* vol. 15, 2012.

[73] M. S. Mihatsch, S. J. Schmidt and N. A. Adams, "Cavitation erosion prediction based on analysis of flow dynamics and impact load spectra," *Physics of Fluids,* vol. 27, no. 10, 2015.

[74] R. T. Knapp, "Recent investigations of the mechanics of cavitation and cavitation damage," *Trans. ASME,* vol. 77, no. 5, pp. 1045-1054, 1955.

[75] R. A. Furness and S. P. Hutton, "Experimental and theoretical studies of two-dimensional fixed-type cavities," *Journal of Fluids Engineering,* pp. 515-521, 1975.

[76] E.-J. Foeth, T. J. C. van Terwisga and C. van Doorne, "On the collapse structure of an attached cavity on a three-dimensional hydrofoil," *Trans. ASME J. Fluids Eng.,* vol. 130, no. 7, 2008.

[77] T. Pham, F. Larrarte and D. Fruman, "Investigation of unsteady sheet cavitaiton and cloud cavitaiton mechanisms," *J. FLuids Eng.,* vol. 121, no. 2, pp. 289-296, 1999.

[78] C. Stanley, T. Barber and G. Rosengarten, "Re-entrant jet mechanism for periodic cavitaiton shedding in a cylindrical orifice," *Int. J. Heat Fluid Flow,* vol. 50, pp. 169-176, 2014.

[79] Y. Kawanami, H. Kato, H. Yamaguchi, M. Tanimura and Y. Tagaya, "Mechanism and control of cloud cavitaiton," *J. Fluids Eng.,* vol. 119, no. 4, pp. 788-794, 1997.

[80] J. Jakobsen, "On the mechanism of head breakdown in cavitating inducers," *J. Basic Eng.,* vol. 86, no. 2, pp. 291-305, 1964.

[81] I. J. Campbell and A. S. Pitcher, "Shock waves in a liquid containing gas bubbles," *Proceedings of the Royal Society of London. Series A, Mathematical and Physical Sciences,* vol. 243, no. 1235, pp. 534-545, 1958.

[82] G. E. Reisman, Y. C. Wang and C. E. Brennen, "Observations of shock waves in cloud cavitation," *J. Fluid Mech.,* vol. 355, p. 255–283, 1998.

[83] K. R. Laberteaux and S. L. Ceccio, "Partial cavity flows. Part 1. Cavities forming on models without spanwise variation," *J. Fluid Mech.,* vol. 431, p. 1–41, 2001.

[84] C. Wang, B. Huang, G. Wang, M. Zhang and N. Ding, "Unsteady pressure fluctuation characteristics in the process of breakup and shedding of sheet/cloud cavitaiton," *Int. J. Heat Mass Transf.,* vol. 114, pp. 769-785, 2017.

[85] M. A. Arabnejada, A. Amini, M. Farhat and R. E. Bensow, "Numerical and experimental investigation of shedding mechanisms from leading-edge cavitation," *Int. J. of Multi. Flow,* vol. 119, pp. 123-143, 2019.

[86] R. Arndt, C. Song, M. Kjeldsen, J. He and A. Keller, "Instability of partial cavitation: a numerical/experimental approach," in *23rd Symposium on Naval Hydrodynamics*, Val deReuil, 2000.

[87] H. Ganesh, S. Makiharju and S. Ceccio, "Bubbly shock propagation as a mechanism afor sheet-to-cloud transition of partial cavities," *J. of Fluid Mech.,* vol. 802, pp. 37-78, 2016.

[88] T. Trummler, S. Schmidt and N. Adams, "Investigation of condensation shocks and re-entrant jet dynamics in a cavitating nozzle flow by Large-Eddy Simulation," *Int. J. Multiphase Flow,* vol. 125, 2020.

[89] A. Sou, B. Bicer and A. Tomiyama, "Numerical simulation of incipient cavitation flow in a nozzle of fuel injector," *Computers and Fluids,* vol. 103, pp. 42-48, 2014.

[90] B. Bicer and A. Sou, "Numerical models for simulation of cavitation in diesel injector nozzles," *Atomization and Sprays,* vol. 25, no. 12, pp. 1063-1080, 2015.

[91] W. Hogendoorn, "Cavitation: Experimental investigation of cavitation regimes in a converging-diverging nozzle," Delft University of Technology, Master Thesis, 2017. http://resolver.tudelft.nl/uuid:823a18f0-66a8-4ffd-a688-c3dadf62c4da.

[92] S. Jahangir, W. Hogendoorn and C. Poelma, "Dynamics of partial cavitation in an axisymmetric converging-diverging nozzle," *Int. J. of Multiphase Flow,* vol. 106, no. 34, 2018.

[93] S. Jahangir, E. C. Wagner, R. F. Mudde and C. Poelma, "Void fraction measurements in partial cavitation regimes by X-ray computed tomography," *Int. J. of Multiphase Flow,* vol. 120, no. 103085, 2019.

[94] B. Cointe, "Cavitation: CFD analysis of cavitaiton dynamics in a converging-diverging nozzle," Delft University of Technology, Master Thesis, 2018. http://resolver.tudelft.nl/uuid:af624f59-e477-4dbe-a5b7-39902a0b1b99.

[95] T. M. Mitchell and F. G. Hammitt, "Collapse of a spherical bubble in a pressure gradient," in *ASME Cavitation Forum*, Detroit, 1970.

[96] D. Dowson and C. M. Taylor, "Proceedings of the 1st Leeds-Lyon Symposium on tribology," in *Mechanical Engineering Publications*, 1974.

[97] P. Dellis and C. Arcoumanis, "Cavitaiton development in the lubricaiton film of a reciprocating piston-ring assembly," *Journal of Engineering Tribology,* vol. 218, no. 157, 2004.

[98] A. Unsworth, D. Dowson and V. Wright, "'Cracking joints'. A bioengineering study of cavitation in the metacarpophalangeal joint," *Annals of the rheumatic diseases,* vol. 30, no. 4, 1971.

[99] J. B. Hunt, A. J. Ryde-Weller and F. A. H. Ashmead, "Cavitation between meshing gear teeth," *Wear,* vol. 71, no. 65, 1981.

[100] J. A. Cole and C. J. Hughes, "Oil flow and film extent in complete journal bearings," *Proc. Instn. Mech. Engers.,* vol. 170, pp. 499-510, 1956.

[101] Y. Zhou, J. He and F. G. Hammit, "Cavitation erosion of diesel engine wet cylinder liners," *Wear,* vol. 76, 1982.

[102] D. Parkins and W. Stanley, "Characteristics of an oil squeeze film," *Journal of Lubrication Technology,* vol. 104, no. 4, pp. 497-502, 1982.

[103] S. R. Gonzalez-Avila, E. Klaseboer, B. C. Khoo and C. Ohl, "Cavitation bubble dynamics in a liquid gap of variable height," *Journal of Fluid Mechanics,* vol. 682, pp. 241-260, 2011.

[104] P. A. Quinto-Su, K. Y. Lim and C. Ohl, "Cavitation bubble dynamics in microfluidic gaps of variable height," *Physical Review E,* vol. 80, 2009.

[105] C. T. Hsiao, J. K. Choi, G. L. Chahine, T. A. Hay, Y. A. Ilinskii, E. A. Zabolotskaya, M. F. Hamilton, G. Sankin, F. Yuan and P. Zhong, "Modelling single- and tandem-bubble dynamics between two parallel plates for biomedical applications," *Journal of Fluid Mechanics,* vol. 716, pp. 137-170, 2013.

[106] N. Mitroglou, M. McLorn, M. Gavaises, C. Soteriou and M. Winterbourn, "Instantaneous and ensemble average cavitation structures in Diesel micro-channel flow orifice," *Fuel,* vol. 116, pp. 736-742, 2014.

[107] M. Winterbourn, C. Soteriou, M. Mitroglou, M. Gavaises and C. Daveau, "Visualising injection events in a fully operational diesel injector with a multi-hole transparent tip," in *Thiesel*, 2014.

[108] C. Soteriou, M. Smith and R. Andrews, "Cavitation hydraulic flip and atomization in direct injection diesel sprays," in *IMechE C465/051/93*, 1993.

[109] C. Soteriou, R. Andrews and M. Smith, "Direct Injection Diesel Sprays and the Effect of Cavitation and Hydraulic Flip on Atomization," *SAE Technical Paper,* 1995.

[110] C. Soteriou, M. Lambert, S. Zuelch and D. Passerel, "The flow characteristics of high efficiency diesel nozzles with enhanced geometry holes," *Thiesel,* 2006.

[111] F. Orley, S. Hickel, S. Schmidt and N. Adams, "Large-Eddy Simulation of turbulent , cavitating fuel flow inside a 9-hole Diesel injector including needle movement," *International J of Engine Research,* 2016.

[112] F. Payri, X. Margot, S. Patouna, F. Ravet and M. Funk, "A CFD Study of the Effect of the Needle Movement on the Cavitation Pattern of Diesel Injectors," *SAE Int.,* vol. 24, 2009.

[113] E. Lehmann, C. Grunzweig, S. Jollet, M. Kaiser, H. Hansen and F. Dinkelacker, "Visualisation of diesel injector with neutron imaging," in *Cavitation Symposium*, Lausanne, 2015.

[114] N. Kyriazis, P. Koukouvinis and M. Gavaises, "Modelling cavitation during drop impact on solid surfaces," *Advances in Colloid and Interface Science,* vol. 260, pp. 46-64, 2018.

[115] Ansys, Inc., "Ansys Fluent Theory Guide," SAS IP, Canonsburg, PA., 2013.

[116] S. Pope, Turbulent flows, Cambridge Unversity Press, 2000.

[117] J. Boussinesq, "Essai sur la théorie des eaux courantes," *Mémoires présentés par divers savants à l'Académie des Sciences,* vol. 23, no. 1, pp. 1-68, 1877.

[118] T. Shih, W. Liou, A. Shabbir, Z. Yang and J. & Zhu, "A new k-ϵ eddy viscosity model for high reynolds number turbulent flows," *Computers and Fluids,* vol. 24, no. 3, pp. 227-238, 1995.

[119] S.-E. Kim, D. Choudhury and B. Patel, "Computations of Complex Turbulent Flows Using the Commercial code ANSYS Fluent," in *CASE/LaRC/AFOSR Symposium on Modeling Complex Turbulent Flows*, Hampton, Virginia, 1997.

[120] F. Menter and Y. Egorov, "The Scale-Adaptive Simulation Method for Unsteady Turbulent Flow Predictions . Part 1 : Theory and Model Description," *Flow Turbulence Combust,* vol. 85, pp. 113-138, 2010.

[121] J. Smagorinsky, "General Circulation Experiments with the Primitive Equations. I. The Basic Experiment," *Month Wea. Rev.,* vol. 91, pp. 99-164, 1963.

[122] E. H. Ndiaye, J. Bazile, D. Nasri, C. Boned and J. L. Daridon, "High pressure thermophysical characterization of fuel used for testing and calibrating diesel injection systems," *Fuel,* vol. 98, 2012.

[123] P. Koukouvinis, G. Bergeles and M. Gavaises, "A new methodology for estimating cavitation erosion: application on a high speed cavitation test," in *11th World Congress on Computational Mechanics*, Barcelona, Spain, 2014.

[124] F. G. Hammitt, "Observations on cavitation damage in a flowing system," *ASME Journal of Basic Engineering,* pp. 347-367, 1963.

[125] M. Brunhart, C. Soteriou, C. Daveau, M. Gavaises, P. Koukouvinis and M. Winterbourn, "Investigation on the removal of the cavitation erosion risk in a control orifice inside a prototype diesel injector," in *IMechE Fuel Systems*, London, 2018.

[126] T. Melissaris, N. Bulton and T. van Terwisga, "On cavitation aggresiveness and cavitation erosion on marine propellers using URANS method," in *10th International Cavitation Symposium*, Baltimore, 2018.

[127] P. Gorkh, S. Schmidt and N. Adams, "Numerical investigation of cavitation-regimes in a converging-diverging nozzle," in *10th International Symposium on Cavitation (CAV18)*, Baltimore, 2018.

[128] G. Chen, G. Wang, C. Hu, B. Huang, Y. Gao and M. Zhang, "Combined experimental and computational investigation of cavitation evolution and excited pressure fluctuation in a convergent-divergent channel," *Int. J. Multiphase Flow,* vol. 72, pp. 133-140, 2015.

[129] H. Zhang, Z. Zuo, K. Morch and S. Liu, "Thermodynamic effects on venturi cavitation characteristics," *Physics of Fluids,* vol. 31, no. 097107, 2019.

[130] B. Stutz and J.-L. Reboud, "Two-phase flow structures of sheet cavitation," *Physics of Fluids,* vol. 9, no. 12, pp. 3678-3686, 1997.

[131] T. Colonius, "Modeling artificial boundary conditions for compressible flow," *Ann. Rev. Fluid Mech.,* vol. 36, pp. 315-345, 2004.

[132] A. Gnanaskandan and K. Mahesh, "Large Eddy Simulation of the transition from sheet to cloud cavitation over a wedge," *Int. J. of Multiphase Flow,* vol. 83, pp. 86-102, 2016.

[133] Delphi Technologies, *Internal documents.*

[134] J. Tullis, "Cavitation guide for control valves," US Nuclear Regulatory Commission, Washington, 1993.

[135] J. Rose, J. Cooper and H. Spiers, Technical data on fuel, London: Scottish Academic Press, 1977.

[136] W. Bergwerk, "Flow patterns in diesel nozzle spray holes," *Proc. of the Inst. of Mech Eng.,* vol. 173, no. 25, pp. 655-660, 1959.

[137] M. Gavaises, A. Andriotis, D. Papoulias, N. Mitroglou and A. Theodorakakos, "Characterization of string cavitation in large-scale Diesel nozzles with tapered holes," *Physics of Fluids,* vol. 21, no. 5, 2009.

[138] C. Soteriou, "Some flow effects of cavitation inside Diesel injectors," in *ILASS*, Chania, 2013.

[139] W. Rankine, "On the thermodynamic theory of waves of finite longitudinal disturbances," *Phil. Trans. Roy. Soc. London,* vol. 160, pp. 277-286, 1870.

[140] P. Hugoniot, "Mémoire sur la propagation du movement dans les corps et plus specialement dans les gaz parfaits, 1-2 Partie," *J. Ecole Polytech,* vol. 58, pp. 1-125, 1889.

[141] N. Mitroglou, M. Lorenzi, M. Santini and M. Gavaises, "Application of X-ray micro-computer tomography on high speed cavitating diesel fuel flows," *Exp. Fluids,* vol. 57, no. 11, 2016.

[142] D. Bauer, F. Barthel and U. Hampel, "High-speed X-ray CT imaging of a strongly cavitating nozzle flow," *J. Phys. Commun,* vol. 2, no. 7, 2018.

[143] M. Lyon, J. McHattie and C. Cardon, "Delphi new diesel common rail family: focus on high pressure pumps," in *Fuel Systems*, London, 2015.

[144] M. Winterbourn, M. Balin, R. Jorach, C. Soteriou, W. Tang and S. Zülch, "The Virtual Pump – Integrated Simulation of the High Pressure Diesel Common Rail Pump," in *Otto-von-Guericke-Universität*, Berlin, 2006.

[145] J. Lang, G. Knoll, I. Thornthwaite, C. Soteriou, C. Lensch-Franzen and M. Kronstedt, "Simulation methods for elastohydrodynamically coupled hydraulic components," in *9th International FLuid Power Conference*, Aachen, 2014.

[146] M. Brunhart, C. Soteriou, C. Daveau, M. Gavaises, P. Koukouvinis and M. Winterbourn, "Cavitaiton erosion risk indicators for a thin gap within a diesel fuel pump," *Wear,* vol. 442, no. DOI-10.1016/j.wear.2019.203024.IJER, 2019.

[147] A. Shima, K. Takayama, Y. Tomita and N. Ohsawa, "Mechanism of impact pressure generation from spark-generated bubble collapse near a wall," *AIAA J.,* vol. 21, pp. 55-59, 1983.